The effects of the ZnO nanoparticles buffer layer on organic solar cells

By

Pontsho Sylvia Mbule

(M.Sc)

A thesis submitted in fulfillment of the requirements for the degree

PHILOSOPHIAE DOCTOR

in the

Faculty of Natural and Agricultural Sciences

Department of Physics

at the

University of the Free State

Republic of South Africa

Promoter : Prof. O.M. Ntwaeaborwa

Co-Promoter : Prof. H.C. Swart

July 2013

“The road to success is not straight. There is a curve called Failure, a loop called Confusion; speed bumps called Friends; red lights called Enemies; caution lights called Family. You will have flats called jobs. But, if you have a spare called Determination; an engine called Perseverance; insurance called Faith, and a driver called Jesus, you will make it to a place called Success!! “

- Unknown

ACKNOWLEDGEMENTS

- First and foremost, I would like to thank the man upstairs, my Creator, for granting me this opportunity to pursue this research and conduct it to the best of my ability. I thank Him for answering my prayers and giving me strength to plod even in emotional times despite the edge of wanting to give up, thank you so much my Dear Lord.

- I express my sincere and heartfelt gratitude to my promoter *Prof. O.M. Ntwaeaborwa* for his excellent guidance on my research for the past several years and helping me develop my background in semiconductor physics and nanotechnology. This research wouldn't have been possible without his invaluable help. Most importantly, he played a great role in securing funds for this study so that it runs smoothly.

- I am immensely grateful to my co-promoter *Prof. H.C. Swart* for providing me with an excellent atmosphere for doing research. He let me experience research particularly his fruitful discussions and lessons on surface characterization. I express my sincere thanks and enormous gratitude to him for his technical advices of the organization of ideas towards this study, in the group meetings and paper write-ups.

- I thank *Dr. Zivayi Chiguvare* and his student *Mr. Lordwell Jhamba* at the school of Physics, University of Witwatersrand for welcoming me at his lab and introducing me to the fabrication of organic solar cells.

- I owe my deepest appreciation to *Dr. BongSoo Kim* and *Mr. Taehee Kim* at the Korea institute of Science and Technology (KIST) for permission, collaboration, introducing me to fabrication and testing of organic solar cells, helping with Photovoltaic extraction measurements, trusting me and allowing me to work and running equipments on my own. In addition, I thank the entire OPV group for their friendly spirit throughout my 3 months stay at KIST.

- I thank *MinWoo Jung, Boeun Kim, Sejong, Dr. Li Yuelong* and his wife for academic ideas and for showing me around at different locations in South Korea.

- I acknowledge *Dr. Liza Coetsee-Hugo* and *Mrs. Mart-Mari Duvenhage* for the surface characterization and measurements for my organic solar cells. And the entire staff and students in Physics department.

- In my daily work I have been blessed with a friendly and cheerful group of fellow post graduate students, I would like to thank *Mr. L.F. Koao, Ms P.P. Mokoena, Miss K.E. Foka, Miss M.A. Tshabalala, Mr. K.G Tshabalala, Mr. M.J. Madito, Ms M.A. Moleme and Mr. S.K.K Shaat* for promoting and stimulating a welcoming academic, social environment and fruitful academic discussions. A special thank you to *Dr. Gugu Mhlongo* for being such an inspiration.

- I'm greatly indebted to the University of the Free State (UFS) and National Research Foundation (NRF) for financial support throughout this research. I thank Photonic Initiative of South Africa (PISA) for financing my trip to South Korea and Korea Research Council of Fundamental Science and Technology (KRCF) and The KIST for NAP (National Agenda Project) program for financing me during my stay in South Korea.

- Last but not least, I owe my lovely thank you to my loving family. I thank my grandmother *Modiehi Mirriam Mbule* for being my rock, I'm where I am now because of the values and morals she instilled in me. Thank you for your prayers, patience and moral support. My entire family, *Meshack Lesoetsa, Alina Mbule, Lettie Mbule, Mamaphesa Esemang, Nobusi Mbule, Teboho Mbule, Luzzete Mbule and Tumelo Mbule.* You all have been there for me from the beginning of my journey and I thank you for your understanding, support and unconditional love.

Abstract

Organic photovoltaics devices have drawn a lot of attention as means for the renewable energy conversion due to the remarkable combination prospective low cost of manufacturing and rapid improvement of performance approaching the traditional silicon solar cells. By introducing metal oxides in organic photovoltaics, the organic solar cells show great potential in terms of device performance with high exciton dissociation, the favorable charge transport ability and the air stability. In this study, ZnO nanostructures are investigated as a buffer layer in organic solar cells (OSCs), focusing on their impact on the device performance.

ZnO nanoparticles, nanoflakes and nanoflowers were successfully synthesized using a wet chemistry route. Based on X-ray diffraction (XRD), the ZnO nanopaticles, nanoflakes and nanoflowers exhibited a hexagonal wurtzite structure matching the standard JCPDS data, card number 80-0075. The particle morphology of ZnO nanostructures was analyzed using field emission scanning electron microscopy (FE-SEM) and transmission electron microscopy (TEM). SEM revealed spherical nanoparticles, randomly oriented nanoflakes and nanoflowers clusters. TEM revealed nanorods clustered into nanoflowers. UV-visible absorption spectra of ZnO nanostructures exhibited peaks at ~251 nm and ~348 nm, attributed to structural defects and intrinsic excitons, respectively.

Conventional and inverted organic solar cells were successfully fabricated. The fabrication process of conventional solar cells was optimized by varying several important parameters in the photo-active blend (P3HT:PCBM). The performance of OSCs improved when the active layer was cast from the chlorobenzene solution rather than 1,2-dichlorobenzene solution. Varying the blend ratio also revealed improved device performance with the 1:0.6 weight ratio. All these parameter processes can significantly influence the device performance.

The effects of ZnO particle morphology on the performance of OSC devices were investigated. The best photovoltaic properties were obtained from devices with the ZnO nanoflakes and nanoparticles as electron extraction layers both spin coated from solutions of 0.5 mg/mL ZnO concentration. The ZnO nanoflakes morphology gave relatively higher power conversion efficiency (PCE) of 3.08 % versus 2.37 % from the ZnO nanoparticles.

The effects of thermal treatment before (pre annealing) and after (post-annealing) the deposition of Al electrode on the conventional devices were also investigated. Improved photovoltaic properties were observed from the post-fabrication annealed device. The inverted device with ZnO nanoparticles electron extraction layer revealed a relatively improved performance versus that with ZnO nanoflowers. Finally the compositional depth profiling and surface imaging were carried out for both conventional and inverted devices and the results indicated that the bulk heterojunction (BHJ) layer was P3HT enriched and there was diffusion of some other elements into the BHJ layer. The surface imaging showed homogeneous as well as inhomogeneous distribution of ions on the surface.

Keywords

Zinc Oxide, Organic solar cells, Photovoltaics, Morphology, Power conversion efficiency

List of Acronyms

XRD	X-ray diffraction
FE-SEM	Field-emission scanning electron microscopy
TEM	Transmission electron microscopy
AFM	Atomic force microscopy
TOF-SIMS	Time-of-flight Secondary ion mass spectrometry
PCE	Power conversion efficiency
EQE	External quantum efficiency
FF	Fill Factor
LUMO	Lowest unoccupied molecular orbital
HOMO	Highest occupied molecular orbital
P3HT	Poly (3-hexalthiophene)
PCBM	[6,6]-phenyl-C_{60} butyric acid methyl ester

PEDOT	Poly (3,4-ethylenedioxythiophene)
PSS	poly (styrenesulfonate)
ITO	Indium tin oxide
OSC	Organic solar cell
BHJ	Bulk-heterojunction

Table of Contents

Chapter 3: Research techniques and device fabrication

Chapter 4: ZnO nanostructures: background, preparation and characterization

Chapter 5: Optimizing the performance of organic solar cells by varying processing parameters in the photo-active layer

Chapter 6: Effects of particle morphology of ZnO buffer layer on the performance of organic solar cells

Chapter 7: Effects of thermal treatment and surface analysis of bulk heterojunction organic solar cells by TOF-SIMS technique

Chapter 8: Inverted organic solar cells with solution processed ZnO nanoparticles/nanoflowers

Chapter 9: Summary and conclusion

List of figures

1 Introduction

1.1 Overview

Energy and the environment have become two of the most critical subjects of wide concern and these two topics are also correlated to each other. An estimated 80% or more of today's world energy supplies are from the burning of fossil fuels such as coal, gas or oil. Carbon dioxide and toxic gases released from burning fossil fuels contribute significantly to environmental degradation, such as global warming, acid rain and smog [1,2,3]. Due to increased demand for energy supplies, alternative renewable and environmentally friendly as well as sustainable energy sources becomes desirable. There are different alternative energy sources that can be used to generate energy, such as solar power, wind power, nuclear power and biomass energy [3]. In addition, sunlight is an unlimited, renewable, clean (non-polluting) and readily available energy source, which can be exploited even at remote sites where the generation and distribution of electric power is a challenge.

Nowadays, any crude oil supply crisis or environmental degradation concern resulting from fossil fuel burning has prompted both researchers and the government to consider solar energy resources more seriously. The technique of converting sunlight directly into electrical power by means of photovoltaic (PV) materials has already been widely used in spacecraft power supply systems and is increasingly extended for terrestrial applications to supply autonomous customers with electric power. According to the U.S PV Industry Technology Roadmap 1999 Workshop and Strategies Unlimited [4], PV technology is becoming a billion dollar per annum industry and is expected to grow at a rate of 15% to 20% per year over the next few decades. PV devices were first demonstrated at the Bell Laboratories more than 50 years ago [5,6]. Silicon solar cells are "big business", their initial applications were in earth satellites and a wider range of applications quickly emerged. Because solar energy is perhaps the most obvious renewable energy source, large scale application of solar cell technology for the production of energy of our future civilization is, and must be a high priority. A priority that becomes even more important as oil

prices continue to increase and fossil fuel burning continues to degrade the global environment. However, silicon solar cell technology suffers from two serious disadvantages: production cost is relatively high and the rate at which new solar cell area can be produced is limited by the basic high temperature processing of silicon [7]. In contrast, recently developed organic and polymeric conjugated semiconducting materials appear very promising for PV applications due to the following reasons [7,8]:

- Their environmental stability and compatibility to mass production.
- Continuous tunability of optical energy band gaps of materials via molecular design, synthesis and ease of processing.
- Possibility of lightweight, flexible shape, versatile device fabrication schemes and low cost on large-scale industrial production.

However the overall power conversion efficiency of current organic solar cells is relatively low, and they have reached 7-8% power conversion efficiencies [9] compared to silicon technology, which can go to over 20% efficiencies according to the timeline for the solar cell energy conversion efficiencies from the National Renewable Energy Laboratory (U.S Department of Energy) [10]. The efficiency can be improved through systematic molecular engineering and the development of the device architecture that is optimally matched to the properties of these new PV materials. Again, it is also important to keep in mind that solar cells are made to generate electricity, so each solar power application results in its own unique set of challenges. These challenges can be addressed by a variety of technologies that overcome specific issues involving available area, efficiency, reliability and specific power at an optimal cost. Organic photovoltaics will most likely provide solutions in applications where price or large area is a challenge and much work remains to be done to further improve their performance.

1.2 Statement of the problem

In order to improve the performance, stability, and lifetime of bulk-heterojunction organic solar cells (BHJ-OSCs), researchers are faced with many challenges that need to be addressed. Appropriate design and fabrication of BHJ-OSCs are of great importance for their development. Therefore the major challenge lies in fabricating BHJ-OSCs in which free-charge-carrier generation is a critical step [11].

Despite high attainable external quantum efficiencies, overall power conversion efficiencies of BHJ-OSCs reported are still low due to inferior charge transport properties and the limited solar spectral absorption range of the polymer active layer. On the other hand, endeavors in synthesis and development of novel low band-gap polymers are being carried out to harvest the major part of the solar spectrum [11,12,13]. Fabrication parameters such as solvent selection and annealing treatment are also critical factors in film morphology of the active layer in BHJ-OSCs. The overall effects of morphology manipulation assist in forming an interpenetrating network of donor and acceptor molecules, facilitating both charge transfer and transport.

For efficient BHJ OSCs, transparent and conductive interfacial materials/buffer layers which are inserted between an active layer and top metal electrode are required. The role of this buffer layer is not only to form an electron selective layer but also to form an electrical contact to the metal electrode. Recently, a thin layer(10-20 nm) of solution processed titanium dioxide (TiO_2) or zinc oxide (ZnO) has been successfully applied as an interfacial layer in the normal and inverted geometry of BHJ-OSCs. Furthermore, BHJ-OSCs can suffer from degradation of the top electrode, which is normally a low work-function metal such as aluminium (Al) that is reactive and can easily be oxidized in air. Alternatively, inverted device geometry is an attractive concept to improve their longevity because a metal electrode such as silver (Ag) or gold (Au), with higher work-function is used. Moreover, this geometry brings the possibility of significantly improving the stability of the BHJ-OSCs in air [14,15,16].

1.3 Study Aim

- The aim of this study is to enhance the absorption efficiency of organic solar cell devices using ZnO nanostructures (nanoparticles, nanoflakes and nanoflowers) as a buffer layer between the photoactive layer and the top metal electrode.

1.4 Study Objectives

- The objectives are to synthesize ZnO nanostructures with different morphology (nanoparticles, nanoflakes and nanoflowers) using wet chemistry route and evaluate the effect of ZnO particle morphology when used as the buffer layer in organic solar cells (OSC).
- To compare the photovoltaic properties of OSC with ZnO buffer layer of different particle morphology.
- To compare the performance of the conventional and inverted OSC devices with ZnO nanostructures.
- To perform depth profiling analysis on conventional and inverted OSCs, to determine the variation of composition with depth below the initial surfaces of different layers of the OSC devices.

1.5 Thesis Layout

- ***Chapter 2:*** This chapter provides the literature review of Organic solar cells. Detailed information on the photovoltaic effect, the generation of solar cells, the origin of the electronic structures, the role of a buffer layer, device geometry, materials, device physics and efficiency characteristics are discussed.

- ***Chapter 3:*** In this chapter, a brief theory of characterization techniques and device fabrication are discussed.

- ***Chapter 4:*** In this chapter, fundamental optical properties of ZnO nanoparticles, nanoflakes and nanoflowers synthesized by a wet chemistry route for applications in organic solar cells are discussed.

- ***Chapter 5:*** This chapter presents optimization of power conversion efficiency of organic solar cells using two solvents for the photo-active materials.

- ***Chapter 6:*** This chapter presents the effects of the particle morphology of ZnO buffer layer on the performance of organic solar cells.

- ***Chapter 7:*** This chapter presents the pre and post annealing effects and TOF-SIMS depth profiling of organic solar cells.

- ***Chapter 8:*** In this chapter, comparison of the effects of ZnO nanoparticles and nanoflowers as electron extraction layers on the performance of inverted organic solar cells is presented.

- ***Chapter 9:*** Is about the summary of this study, conclusions and suggestions for possible future studies of organic solar cells, particularly using ZnO nanoparticles as a buffer layer.

References

[1] Sam-Shajing and Niyazi Serdar Saricifti, *Organic Photovoltaics, Mechanisms, Materials and devices*, (2005) Johannes Kepler University of Linz, Austria

[2] Eray S. Aydil, Nanomaterials for Solar Cells, *Nanotechnology Law and Business* **4**(2007) 275-291

[3] http://library.thinkquest.org/06aug/01335/welcome.htm [Accessed 11 Nov 2011]

[4] PV Technology Industry Roadmap Workshop Report, website: www.nrel.gov/ncpv [Accessed 11 Nov 2011]

[5] Gerhard P. Willek, *The Crystalline Silicon Solar Cell, History, Achievements and Perspectives*, 19th European PV Solar Energy Conference, June 2004, Paris, France

[6] Martin A. Green, Silicon Solar Cells, Evolution, High efficiency Design and Efficiency Enhancements, *Semiconductor Science and Technology*, **8**(1993) 1-12

[7] Ghidichimo G and Filippelli L, Organic Solar Cells: Problems and Perspectives, *International Journal of Photoenergy*, May 2010, doi:10.1155/2010/123534

[8] Serap Gunes and Niyazi Serdar Sariciftci, Review of Hybrid Solar Cells, *Inorganica Chimica Acta* **361**(2008) 581-588

[9] Ta-Ya Chu, Sai-Wing Tsang, jiayun Zhou, Pierre G. Verly, Jianping Lu, Serge Beaupre, Mario Leclerc and Ye Tao, *Solar Energy Materials and Solar Cells* (2011), doi:10.1016/j.solmat.2011.09.042

[10] http://www.nrel.gov/ncpv/images/efficiency_chart.jpg [Accessed 11 Nov 2011]

[11] L.-M. Chen, Z. Hong, G. Li and Y. Yang., *Advanced Materials* **21**(2009) 1434-1449

[12] J. Peet, C. Soci, R. C. Coffin, T. Q. Nguyen, A. Mikhailovsky, D. Moses, G.C. Bazan, *Applied Physics Letters* **89**(2006) 252105-1 - 252105-3

[13] C. Soci, I.-W. Hwang, D. Moses, Z. Zhu, D. Waller, R. Gaudiana, C. J, Brabec, A. J. Heeger, *Advanced Functional Materials* **17**(2007) 632-636

[14] H. Oh, J. Krantz, I. Litzov, T. Stubhan, L. Pinna and C.J. Brabec, *Solar Energy Materials and Solar Cells* **95**(2011) 2194-2199

[15] N. Sekine, C.-H. Chou, W.L Kwan and Y. Yang, *Organic Electronics* **10** (2009) 1473-1477

[16] S.H Eom, S. Senthilarasu, P. Uthirakumar, C.-H. Hong, Y.-S. Lee, J. Lim, S. C Yoon, C. Lee and S.-H. Lee, *Solar Energy Materials and Solar Cells* **92** (2008) 564-570

2 Literature Review

This chapter presents background information on organic solar cells. The photovoltaic effect, generation of solar cells, the device structure, characterization, physics of the devices, working principles, efficiency characteristics and applications are discussed extensively.

2.1 The Photovoltaic effect

Solar photovoltaic energy conversion is a one-step conversion process which generates electrical energy from sunlight energy. The explanation relies on ideas from quantum theory. Light is made up of packets of energy, called photons, whose energy depends only upon the frequency or colour of the light. The energy of visible photons is sufficient to excite electrons bound to solids, up to the higher energy levels where they are free to move [1]. An extreme example of this is the photoelectric effect, the celebrated experiment which was explained by Einstein in 1905, where blue or ultraviolet light provides enough energy for electrons to escape completely from the surface of a metal [2]. Normally, when light is absorbed by matter, photons are given up to excite electrons to higher energy states within the material, but the excited electrons quickly relax back to their ground state [1,2]. A photon of frequency υ carries energy $h\upsilon$, where h is plank's constant. If such a photon strikes an electron inside a metallic conductor, it can knock the electron out of the metal. Once liberated, the free electron has an energy $h\upsilon$-W, where W is the binding energy which formerly kept it inside, i.e. the work-function of the metal. This photoelectric effect is illustrated in Figure 2.1 (a).

However, in a photovoltaic device, there is some built-in electric field which pulls the excited electrons away before they can relax, and feeds them to an external circuit. The extra energy of the excited electrons generates a potential difference or an electromotive force (e.m.f), and this force drives the electrons through a load in the external circuit to do electrical work [3]. The effectiveness of a photovoltaic device depends upon the choice of light absorbing materials and the way in which they are connected to the external circuit. Figure 2.1 (b) shows the photovoltaic effect.

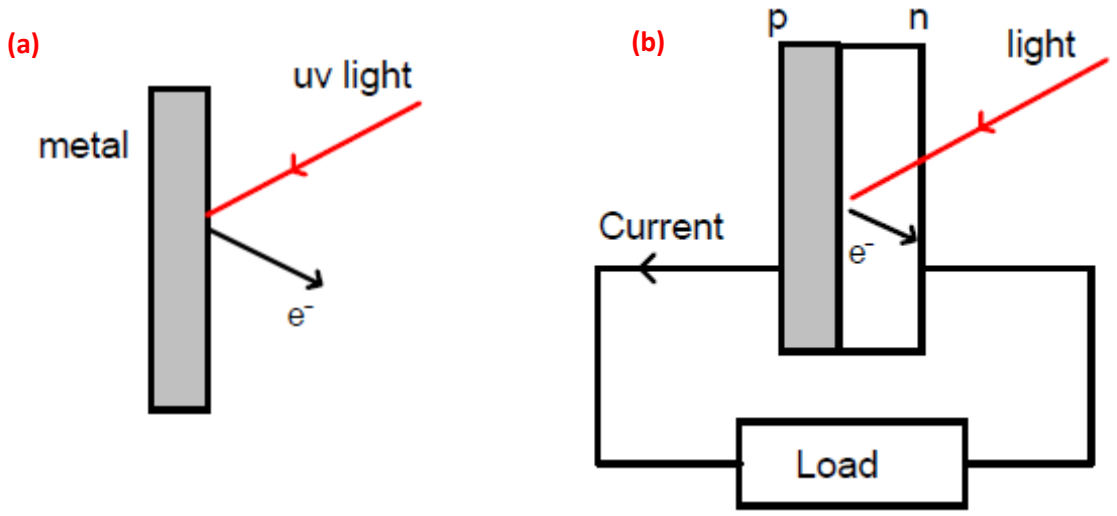

Figure 2.1: Comparison of the (a) photoelectric effect where UV light liberates electrons from the metal surface with (b) the photovoltaic effect in a solar cell [1].

2.2 Brief History of Solar Cells

A solar cell is a device that converts light into an electric current by means of the photovoltaic effect [4]. The photovoltaic effect was first reported by Edmund Becquerel in 1839 when he observed that the action of light on a silver coated platinum electrode immersed in electrolyte produced an electric current [5,6]. Forty years later the first solid state photovoltaic devices were constructed by researchers, investigating the recently discovered photoconductivity of selenium. In 1876, William Adams and Richard Day found that a photocurrent could be produced in a sample of selenium when contacted by two heated platinum contacts. The photovoltaic action of the selenium differed from its photoconductive action in that a current was produced spontaneously by the action of light and no external power supply was needed. In this early photovoltaic device, a rectifying junction had been formed between the semiconductor and the metal contacts. In 1894, Charles Fritts prepared what was probably the first large area solar cell by pressing a layer of selenium between gold and another metal [7]. In the following years, photovoltaic effects were observed in copper-copper oxide thin film structures, in lead sulphide and thallium sulphide. These cells were thin film Schottky barrier devices, where a semitransparent layer of metal deposited on top of the semiconductor provided both the asymmetric electronic junction, which is necessary for photovoltaic action and access to the

junction for the incident light [8]. The photovoltaic effect of structures like this was related to the existence of a barrier to current flow at one of the semiconductor-metal interfaces by Goldman and Brodsky in 1914. Later, during the 1930s, the theory of metal-semiconductor barrier layers was developed by Walter Schottky and Neville Mott [8]. However, it was not the photovoltaic properties of materials like selenium which excited researchers, but the photoconductivity. The fact that the current produced was proportional to the intensity of the incident light, and related to the wavelength in a definite way meant that photoconductive materials were ideal for photographic light meters. The photovoltaic effect in barrier structures was an added benefit, meaning that the light meter could operate without a power supply. In the 1950s, with the development of good quality silicon wafers for applications in the new solid state photovoltaic devices in crystalline silicon were developed.

The development of silicon electronics followed the discovery of a way to manufacture p-n junctions in silicon. Naturally n-type silicon wafers developed a p-type layer when exposed to the gas boron trichloride. Part of the layer could be etched away to give access to the n-type layer beneath. Therefore, these p-n junction structures produced much better rectifying action than Schottky barriers and better photovoltaic behavior. The first silicon solar cell was reported by Chapin, Fuller and Pearson in 1954 and converted sunlight with an efficiency of 6%, six times higher that the best previous attempts [9].

The early silicon solar cell did introduce the possibility of power generation in remote locations where fuel could not easily be delivered. The obvious applications was to satellites where the requirement of reliability and low weight made the cost of the cells unimportant and during the 1950s silicon solar cells were widely developed for applications in space. Also in 1954, a cadmium sulphide p-n junction was produced with an efficiency of 6% and in the following years studies of p-n junction photovoltaic devices in gallium arsenide, indium phosphide and cadmium telluride were stimulated by theoretical work indicating that these materials would offer a higher efficiency. However, silicon remained and still remains the foremost photovoltaic material, benefiting from the advances of silicon technology for the microelectronics industry. Short histories of the solar cells are given elsewhere [10, 11, 12] for further reading. In the 1970s, the crisis in energy supply experienced by the oil-dependent western world led to a sudden growth of interest in alternative sources of energy and funding for research and development in those areas. Photovoltaics were a subject of intense interest during this period

and a range of strategies for producing photovoltaic devices and materials more cheaply and for improving device efficiency were explored. Ways to lower cost included photo electrochemical junctions and alternative materials such as polycrystalline silicon, amorphous silicon, other thin film materials and organic conductors. Although none of these led to widespread commercial development, understanding of the science of photovoltaics was mainly rooted in this period. During the 1990s, interest in photovoltaics expanded along with growing awareness of the need to secure sources of electricity alternatives to fossil fuels. The trend coincides with the widespread deregulation of the electricity markets and growing recognition of the viability of decentralized power. During this period, the economics of photovoltaics improved primarily through economics of scale. In the late 1990s the photovoltaic production expanded at the rate of 15-25% per annum, driving a reduction in cost.

Recently, significant research interests from both academia and industry is growing with demands for energy and the focus is on seeking the most cost efficient renewable energy sources. Much of the research into solar power has been focused on organic solar cells and new ways of manufacturing organic solar cells that can scale up to large volumes and low cost are required. A broad range of solar cell technologies are currently being developed, including dye-sensitized nanocrystalline photo electrochemical solar cells, polymer/fullerene bulk heterojunctions, small molecule thin films and organic-inorganic hybrid devices.

2.3 Generations of Solar cells

Solar cells are classified into three generations, namely first, second and third. The generations indicate the order of which each type of a solar cell became important. There is concurrent research into all three generations but the first generation technologies are still the most highly represented in the commercial production [13].

2.3.1 First generation

The first generation represents the types of solar cells that are made from silicon and are currently the most efficient solar cells available for residential use and account for about 80% of all the solar panels sold around the world. Generally silicon based solar cells are more efficient and longer lasting than the non silicon based cells. However, they are more at risk to lose some of their efficiency at higher temperatures (hot sunny days). There are currently four types of silicon based cells used in the production of solar panels for residential use and they are based on the type of silicon used [14]. Examples of silicon based solar cells are monocrystalline, polycrystalline and amorphous silicon solar cells.

2.3.1.1 Monocrystalline Silicon Cells

The oldest solar cell technology and still the most popular and efficient are solar cells made from thin wafers of silicon. These are called monocrystalline solar cells because they are sliced from large single crystals that have been grown under carefully controlled conditions. Typically, the cells are a few inches across and a number of cells are laid out in a grid to create a panel. A monocrystalline silicon panel is shown in figure 2.2.

Figure 2.2: Monocrytalline silicon solar panel [15].

Relative to other types of cells they have a higher efficiency of about 24.2% and more electricity from a given area of panel can be obtained. However, growing large crystals of pure silicon is difficult and very energy-intensive process, so the production costs for this type of a panel historically are the highest of all the solar panel types. Again, panels made from monocrystalline silicon cells can lose their efficiency as the temperature increases, so they need to be installed in such a way as to permit the air to circulate over and under the panels [14].

2.3.1.2 Polycrystalline Silicon Cells

It is cheaper to produce silicon wafers in molds from multiple silicon crystals rather than from a single crystal as the conditions for growth do not need to be as tightly controlled. In this form, a number of interlocking silicon crystals grows together. Panels based on these cells are cheaper per unit area than monocrystalline panels but also slightly less efficient. Up to 13.3% can be obtained [14]. They are in a form of a square-block that can be cut into square wafers with less waste of space or material than round single-crystal wafers. Figure 2.3 shows an example of these panels.

Figure 2.3: A polycrystalline silicon solar panel [15].

2.3.1.3 Amorphous Silicon Cells

Most solar cells used in calculators and many small electronic devices are made from amorphous silicon. Instead of growing silicon crystals as is done in making the two previous types of cells, silicon is deposited as a very thin layer on to a substrate such as a metal, glass or even a plastic. The production methods are complex but less energy intensive than crystalline panels and prices have been coming down as panels are mass produced. The advantage of using very thin layers of amorphous silicon is that the panels can be made flexible. However disadvantage of amorphous panels is that they are much less efficient per unit area and are generally not suitable for roof installations. For a given power rating they do perform better at low light levels that crystalline panels and they are less likely to lose their efficiency as the temperature increases [14]. An amorphous silicon solar panel is shown in figure 2.4.

Figure 2.4: An amorphous silicon solar panel [15].

2.3.2 Second Generation

The second generation solar cells are usually called thin film solar cells because they are made from layers of semiconductor materials only few micrometers thick. The combination of using less material and lower cost manufacturing processes allow the manufacturers of solar panels made from this type of technology to produce and sell panels at much lower costs. There are three types of solar cells that are considered in this category- amorphous silicon, cadmium

telluride (CdTe) and copper indium gallium diselenide (CIGS). They have counted for about 16.8% of the panels sold in 2009 [14]. An example of a thin film solar cell is shown in Figure 2.5. About 99% of the light shining on a CIGS solar cell will be absorbed in the first micrometer of the material. Cells made from CIGS are usually heterojunction structures, structures in which the junction is formed between semiconductors having different band-gaps. The most common material for the top or window layer in CIGS devices is cadmium sulfide (CdS), although zinc is sometimes added to improve transparency. Adding small amounts of gallium to the lower absorbing CIS layer boosts its band-gap from its normal 1.0 electron-volt (eV), which improves the voltage and therefore the efficiency of the device. This particular variation is commonly called a copper indium gallium diselenide or "CIGS" solar cell.

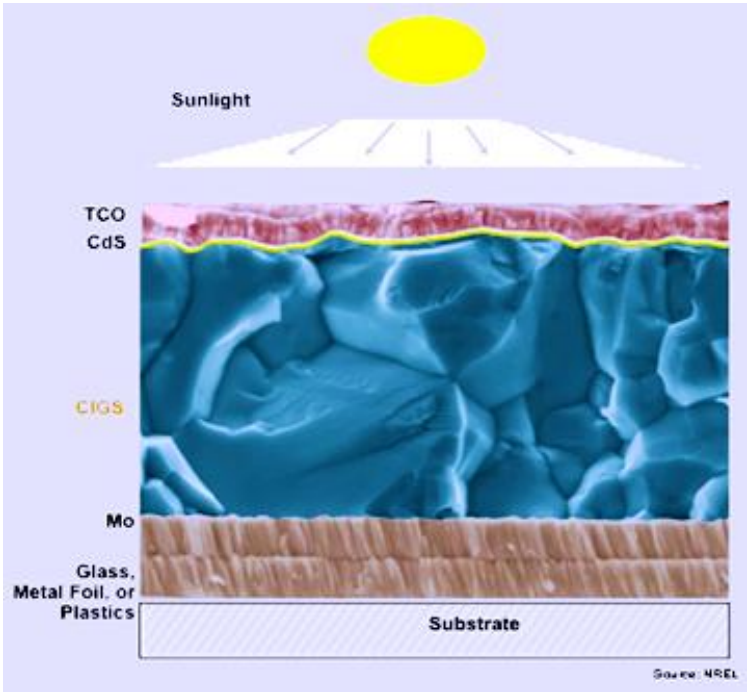

Figure 2.5: A CIGS solar cell [14].

2.3.3 Third generation

There has been an ongoing of solar research in what is being referred to in the industry a third – generation solar cells. In fact, according to the number of patents filed in the United States, solar research ranks second only to research in the area of fuel cells. This new generation of solar cells is being made from variety of new materials including nanotubes, organic dyes and conductive plastics. The goal is to improve the solar cells that are already commercially available. Currently,

most of the work on third generation solar cells is being done in the laboratory and being developed by new companies [14]. Third generation solar cells consists of a wide range of innovations including nano-crystalline solar cell, dye sensitized solar cells and polymer/organic solar cells. These solar cell technologies are being developed to enhance poor performance of the thin film solar cells with low production costs. Still in the research phase, these solar cells are the cutting edge in technology.

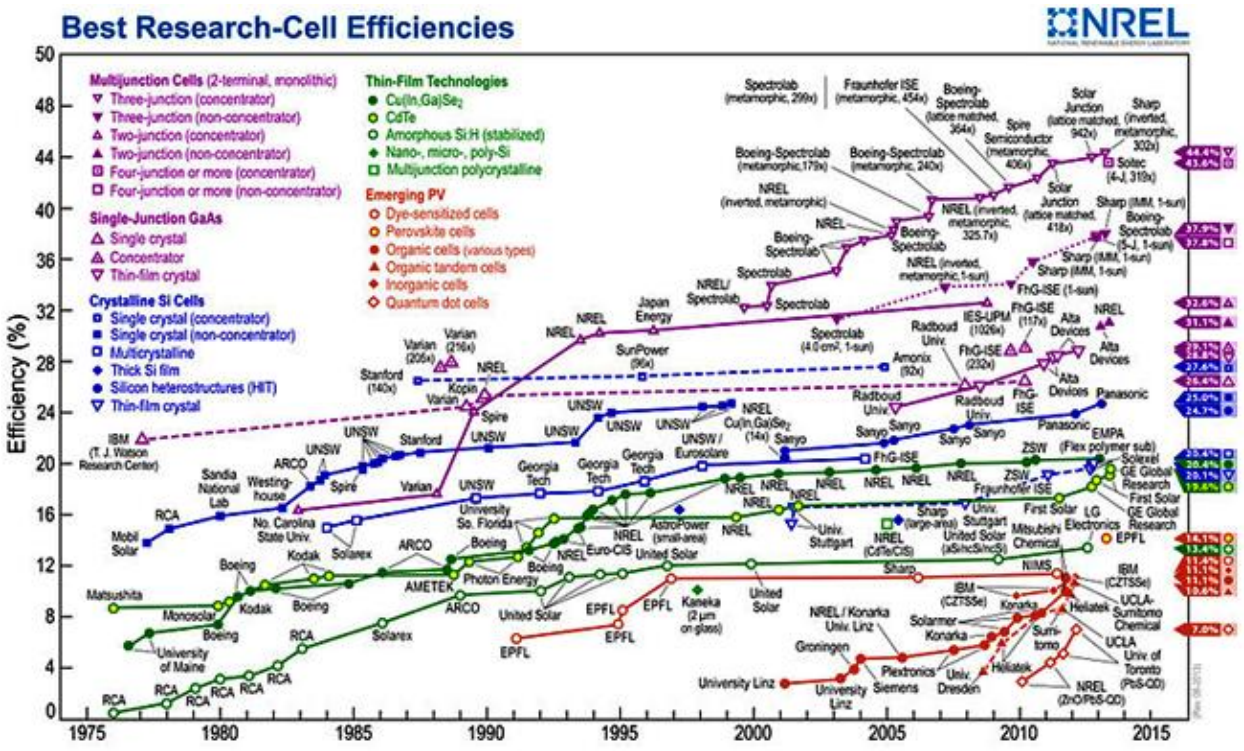

Figure 2.6: Reported timeline of solar cells energy conversion efficiencies [15].

Concurrent research is going on in all three generations and efficiencies of solar cells in different generations are shown in figure 2.6. The figure shows the comparison of the power conversion efficiencies of organic solar cells or third generation solar cells with the existing technologies based on inorganic materials. It shows the record of power conversion efficiencies from different research institutions, industries and universities with respect to the year in which the efficiencies were obtained. It is clear that the multi-junction concentration based solar cells are still on top, as their efficiencies have reached about 43.5 % as compared to 8.3 % of those emerging photovoltaic cells such as organic solar cells, which still needs to be improved.

2.4 Overview of organic solar cells

Organic solar cells research has developed during the past 30 years, especially in the last decade it has attracted scientific and economic interest triggered by a rapid increase in power conversion efficiencies [16]. Many organic solar cell devices use polymers as integral parts of their construction, for example, conjugated polymers often participate as electron donors and hole conductors in the active layer of an organic solar cell. However, basic organic solar cell research and device development still have a long way to go to be able to compete on an equal footing with conventional inorganic solar cells. The efficiency of inorganic solar cells can top 20% and the development of inorganic thin layer and multi-junction devices will likely lead to even better performance [17].

Further steps to improve the power conversion efficiencies of organic solar cells are made by solution-processed polythiophene:Fullerene and efficiencies between 6% and 8% by use of novel materials as well as additives optimizing the phase separation have been obtained [18, 19, 20]. The research and development of organic solar cells focuses mostly on two concepts, either soluble blends of conjugates polymers with fullerene derivatives or the combination of small molecular donor and acceptor materials, a material combination which can be thermally evaporated [21,22]. The first attempts to create organic solar cells were made by sandwiching a single layer of organic material between two dissimilar metal electrodes of different work function, see figure 2.7. In these cells the photovoltaic properties strongly depend on the nature of the electrodes [22, 23, 24]. These are called single layer organic photovoltaic cells and are the simplest form among various organic photovoltaic cells. By the absorption of light, strongly coulomb bound electron-hole pairs are created and their binding energy in organic semiconductors inhibiting much lower effective dielectric constants is usually between 0.5 and 1 eV. The excitons have to be separated to finally generate a photocurrent. In order to overcome the exciton binding energy, one either has to rely on thermal energy or dissociate the exciton at the contacts [25]. Unfortunately, both processes have a rather low efficiency under the operating conditions of solar cells and the temperature is not high enough so the sample thickness is much higher than the exciton diffusion length. Not all the excitons are dissociated and as a consequence, the single layer organic solar cells have power conversion efficiencies far below 1%.

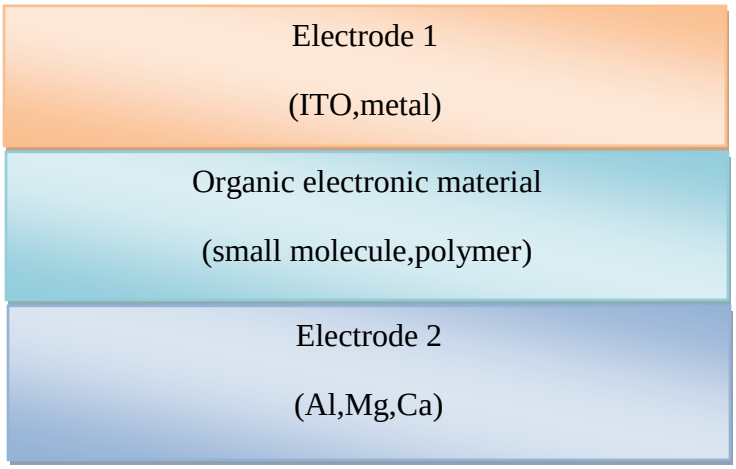

Figure 2.7: Single layer organic photovoltaic cell [24].

The second organic semiconductor layer was introduced and the first organic bilayer solar cell was presented by Tang in the mid-1980s [26]. The typical device configuration is shown in figure 2.8(a). In bilayer devices, the light is usually absorbed in the donor material and the photo generated excitons diffuse within the donor towards the planar interface to the second material, the acceptor, which is usually chosen to be strongly electronegative. The acceptor material provides the energy needed for the excitons to be separated, as the electrons can go to a state of much lower energy within the acceptor. In combining electron donating (p-type) and electron accepting (n-type) materials in the active layer of a solar cell, a bulk heterojunction (BHJ) was described by Yu et al in 1995 [27]. They reported that the bulk heterojunction significantly improved organic solar cells power conversion efficiencies by increasing the excitons access to the donor/acceptor interfaces. An example of BHJ is illustrated in figure 2.8(b). BHJ is presently the most widely studied photoactive layer and the name bulk-heterojunction solar cell has been chosen because the interface (heterojunction) between both components is all over the bulk (Figure 2.8b), in contrast to the classical (bilayer) heterojunction. Polymer-fullerene solar cells were among the first to utilize this bulk-heterojunction principle and have an advantage because of their much larger interface between the donor and acceptor [28].

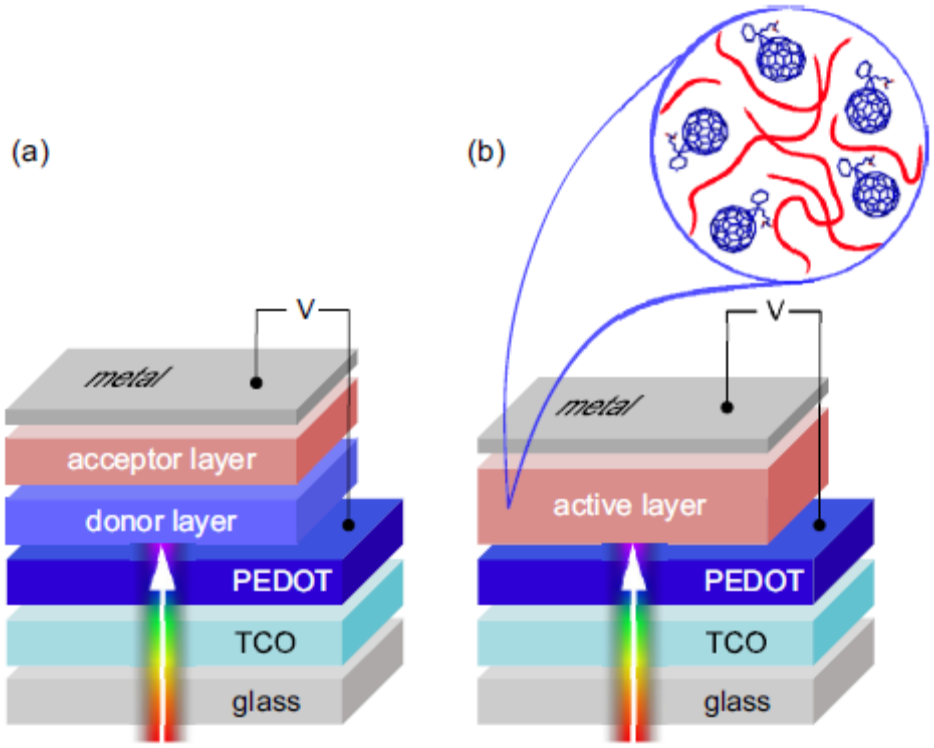

Figure 2.8: Typical device configurations of organic solar cells: (a) bilayer device with planar heterojunction, (b) bulk heterojunction device consisting of a blend of conjugated polymer with a fullerene derivative. On top of the glass substrate, a transparent conductive oxide (TCO) such as indium tin oxide acts as anode, a poly (3,4-ethylendioxythiophen) : polystyrolsulfonate (PEDOT) interlayer helps to avoid local shunts. The active layer consists of either the bilayer or the blend of organic semiconductors. On top, a metallic electrode acts as cathode [22].

2.5. Origin of the electronic structure in organic semiconductors

Organic semiconductors have different electrical properties when compared to traditional inorganic semiconductors. In this section, a brief overview of the electronic structure and charge carrier behavior of an organic semiconductor will be discussed. In addition, excitons or bound electron-hole pairs, which couple optical and electronic processes in organic materials, are introduced. Optoelectronic devices based on excitonic semiconductors have different operation principles and design requirements compared to those on traditional inorganic materials.

An understanding of charge transport and exciton formation is therefore crucial in effective device design and optimization [29]. All organic semiconducting materials, whether they are small molecules, polymers or more complex structures, rely on conjugated π-electron systems for conduction. Systems are considered π-conjugated when alternating carbon-containing single and double bonds are present in their molecular structure. A straight forward example of this system is an ethane molecule (C_2H_4), shown in figure 2.9. Each carbon atom in ethane is sp^2 hybridized, with three sp^2 orbitals created per atom and one leftover unhybridized p_z obital. The six sp^2 orbitals result in five strong σ-bonds within the system (four C-H bonds and one C-C), with the leftover dumbbell-shaped p_z orbitals around each carbon atom forming a C-C π-bond. Due to the shape of the p_z orbitals, the C-C π-bond has weak interaction due to small electron cloud overlap above and below the molecular plane [29].

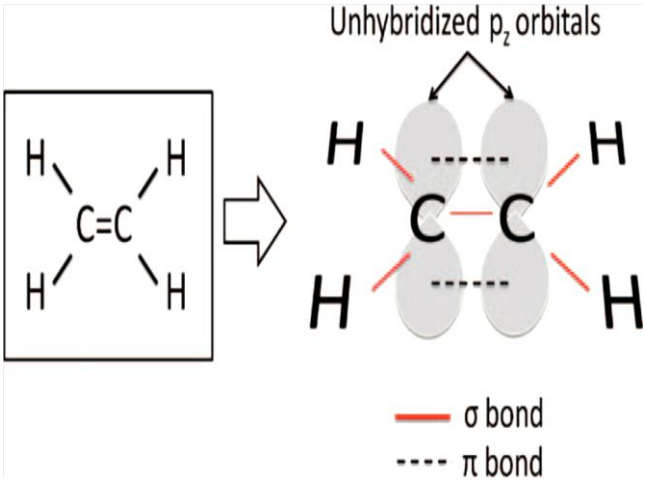

Figure 2.9: Diagram of σ- and π-bonding within an ethane molecule [29].

The strength of the overlapping σ-bonds leads to strong bonding (σ) and antibonding (σ*) molecular orbitals (MOs). The weaker interactions of the parallel p_z orbitals give correspondingly weaker bonding (π) and antibonding (π*) MO energy levels, making the π-π* transition as the smallest possible electronic excitation within the molecule. This is schematically represented in figure 2.10.

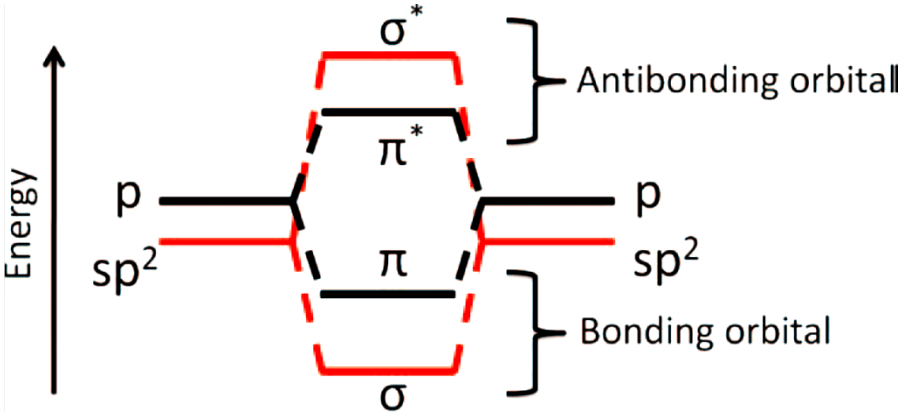

Figure 2.10: Schematic energy level diagram of a discrete organic molecule. The electronic band gap (HOMO-LUMO) is taken as the π-π* gap [29].

Because of the importance of the π-π*transition as the lowest-energy option in a π-conjugated system, the π-bonding MO is dubbed the highest occupied molecular orbital (HOMO) and the π*-antibonding MO is named the lowest unoccupied molecular orbital (LUMO). The HOMO and LUMO, respectively, are analogous to the valence and conduction bands in inorganic semiconducting materials. The degree of π-conjugation within an organic solid has a large impact on its electrical properties. Increased conjugation length causes a greater degree of electron delocalization, increasing the mobility of charges through the π-bonding system. Similarly, short conjugation length localizes electrons, reducing their ability to freely move about a system. This is reflected typically in the polyacenes, conjugated systems of conjoined benzene rings. Increased conjugation (more conjoined benzene rings) corresponds with the red-shifted absorption spectra caused by decreasing HOMO-LUMO separation. For example, the absorption maximum of benzene occurs at 225 nm, the increased conjugation in pentacene shifts its absorption maximum to 580 nm. This illustrates a prime strength of organic transport and optical properties [29,30].

2.6. Device geometry and materials

Since the introduction of the organic photovoltaics, several structures and materials have been used for design and fabrication of efficient and stable organic solar cells. In the construction of a working organic solar cell the organic layer is just one of the necessary components or layer. The device must also be designed to effectively get light in and charge out. The standard organic solar cell consists of glass substrate pre-coated with indium tin oxide (ITO), an organic layer

PEDOT:PSS, the active layer (a blend of P3HT:PCBM) and a top metal electrode, normally an aluminium metal. It is also notable that in this study ZnO is used as a buffer layer or electron selective layer in both geometries of organic solar cells. Figure 2.11 (a-b), shows the schematic diagram of the organic solar cell geometry. On the side where light will come in there is a transparent conducting electrode, ITO. There are two different organic solar cells geometries used in this study, i.e. normal/conventional and inverted. In normal cells, ITO is the anode or positive electrode and the cathode or negative electrode is the metal with a lower work function than ITO (usually aluminium). ITO is the cathode in inverted cells and a metal with a work function greater than ITO (usually silver or gold) is the anode. However, there are advantages and drawbacks for each geometry. Normal orientation results in relatively high efficiencies, while inverted cells are both more stable and more amenable to solution processing.

There is also often a glass substrate that provides mechanical support and anti-reflection coatings can also help to minimize losses due to non-absorption. On the other dark side the electrode usually consists of a thin film of metal such as Au or Al for a conventional device and Ag for inverted devices that have been evaporated onto the organic layer. Care must be taken with the attachment of the electrodes to the organic materials, lest an insulating layer forms. Strategies have been developed for certain materials, such as adding buffer layers to solve the problem of instability and degradation [31].

The energy level alignment in the organic solar cells is schematically shown in figure 2.10 (c-d) (Energies are referenced to the vacuum level). While P3HT and PCBM form a donor-acceptor heterojunction that facilitates the dissociation of photo-generated excitons (bound electron-hole pairs), the lower conduction band edge of ZnO as compared to the lowest unoccupied molecular orbital (LUMO) of P3HT may also lead to dissociation of excitons in P3HT via rapid electron transfer to ZnO. The similar electron affinities of ZnO and PCBM also suggest that there is a negligible barrier height for electron transport from PCBM towards the Al cathode. Furthermore, the very deep valence band of ZnO creates a large barrier height to block hole injection from the P3HT: PCBM active layer into ZnO [32].

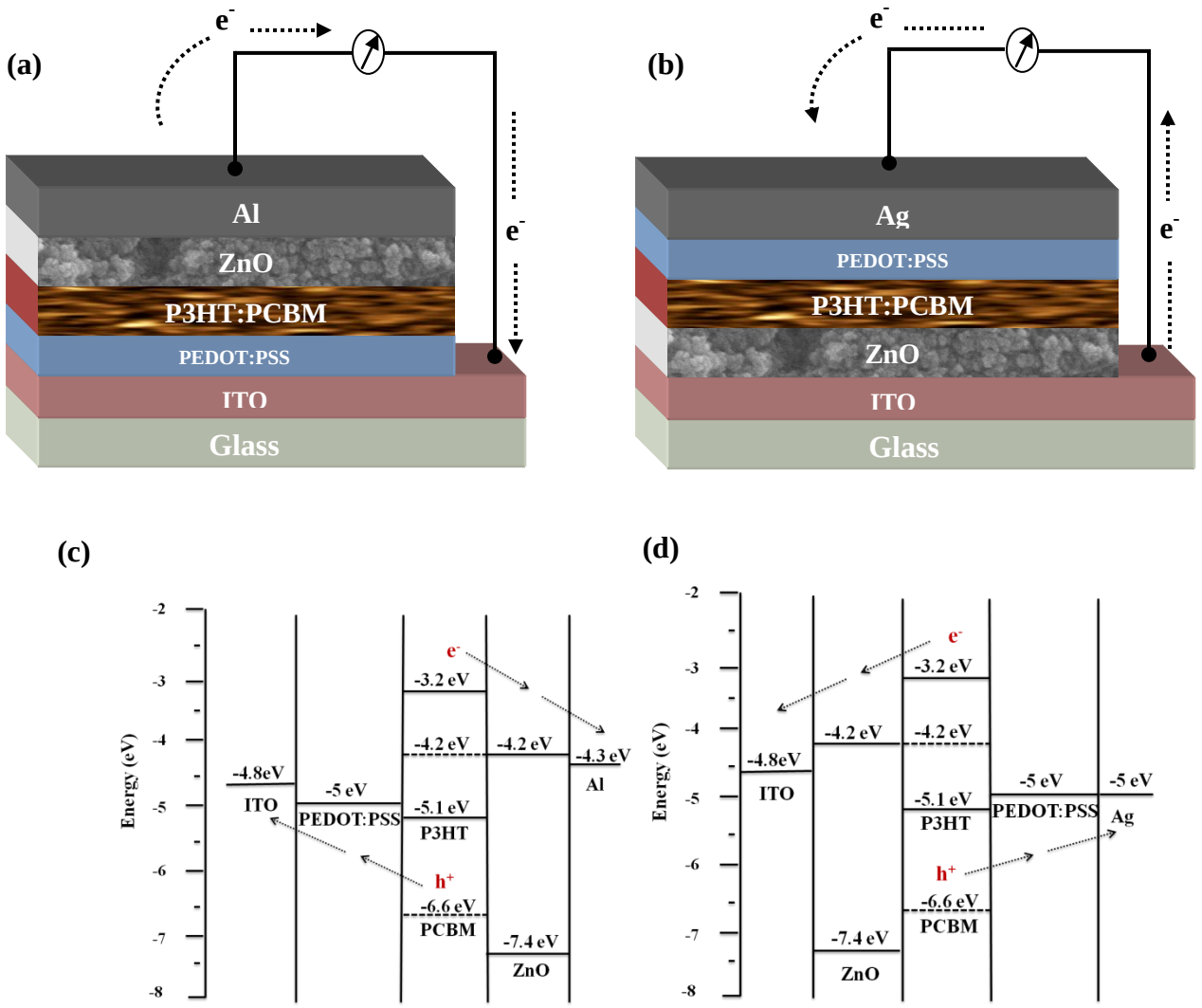

Figure 2.11: (a) Conventional Schematic Device structure, (b) Inverted structure and their Energy level diagrams (c and d). The energies are referenced to the vacuum level [32].

2.6.1 Indium tin oxide (ITO)

The interest in transparent conductors has tremendously increased since the first report of a transparent conducting cadmium oxide films by Bedeker (1907) [33]. For a solar cell or other opto-electronic applications, at least one transparent electrode is required. Typically, a transparent conductive oxide (TCO) is used and should have a high conductivity (or low sheet resistance), a high transparency, good substrate adherence and low surface roughness. The latter is necessary to prevent shunts in solar cells. The most widely used TCO in bulk heterojunction solar cells is Indium Tin Oxide (ITO). A composite oxide where indium oxide (Typically > 90%)

is doped with tin oxide (<10 %) and a glass substrate coated with a thin ITO layer can be obtained from commercial sources. ITO is unique in its combination of optical transparency, metallic conductivity and high work function making it an excellent contact to p-like organic molecules. It is a degenerately doped n-type semiconducting oxide with the bandgap of approximately 3.75 eV [34]. Figure 2.12 shows the band structure of ITO. The wide bandgap formed between the O 2p6 states and In 5s states permits high transparency while the degenerate doping of the In 5s band by Sn^{3+} donor states introduces a high density of free electrons.

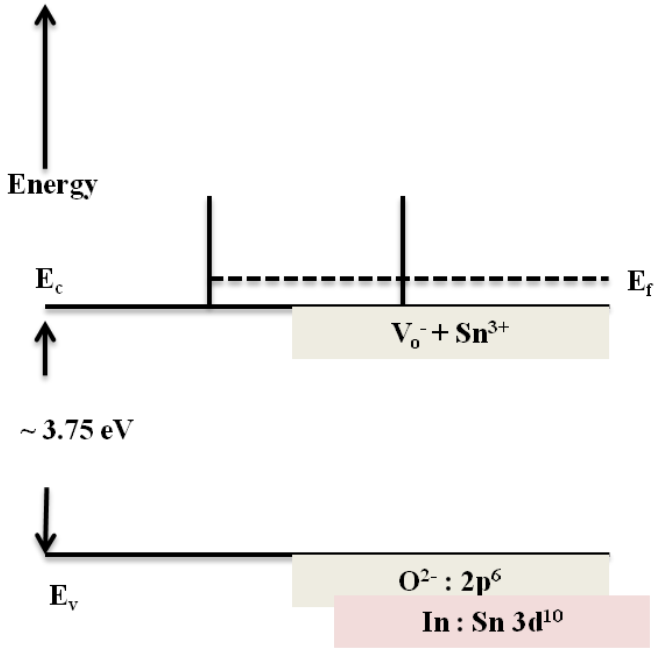

Figure 2.12: Band structure of tin doped indium oxide (ITO). Valence and conduction bands arise from O 2p and In 5s atomic orbitals [34].

2.6.2. Active Layer

In organic solar cells, the active layer material is responsible for light absorption; charge carrier production and carrier separation. Since exciton dissociation occurs at the interfaces, the active material is composed of the electron donor poly (3-hexalthiophene) (P3HT) and the fullerene [6,6]-phenyl-C_{60} butyric acid methyl ester (PCBM) as the electron acceptor [35]. In this work, P3HT and PCBM are used as the donor and acceptor. P3HT based organic solar cells are the most promising and efficient devices among other polymer based solar cells. This is despite higher band gap of P3HT polymer (1.9 eV) in comparison with the solar spectrum peak at 1.8

eV. One reason for outstanding performance of P3HT based devices is the efficient formation of the P3HT and PCBM mixture and the relatively uniform dispersion of PCBM in the polymer structure [36]. The chemical structures of both the polymer and fullerene are shown in figure 2.13.

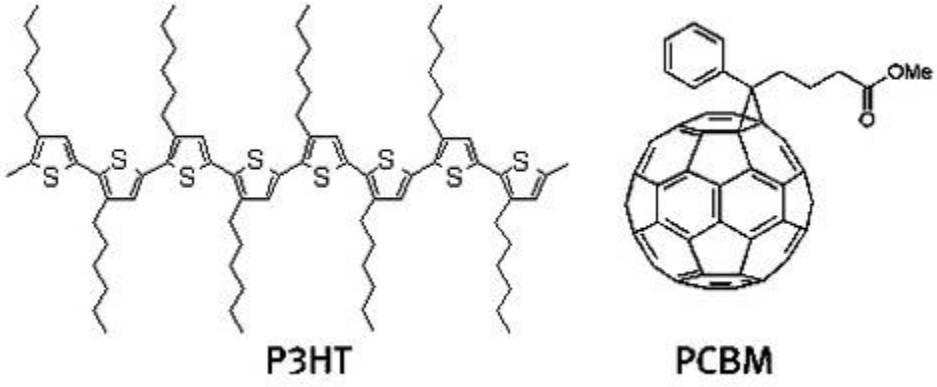

Figure 2.13: The chemical structure of the polymer poly(3-hexylthiophene) (P3HT) and the fullerene [6,6]-phenyl-C60 butyric acid methyl ester[37].

The significant improvement of power conversion efficiency (PCE) is mainly due to the crystallinity of P3HT. After casting P3HT and PCBM blend solution, the blend film morphology is controlled by varying the solvent evaporation rate. During the solvent evaporation, P3HT and PCBM forms a well-mixed interdigitated blend film, where P3HT forms a crystalline morphology and PCBM aggregates are embedded. This phase separated morphology of blend layers enhances the hole mobility and also improves the absorption efficiency from P3HT.

2.6.3. Intermediate layers

Intermediate layers placed between the active layer and electrodes are either hole-conducting or electron conducting materials. Poly (3,4-ethylenedioxythiophene) poly (styrenesulfonate) or PEDOT:PSS, a conjugated polymer, is the most commonly used hole conducting layer (see figure 2.14) [38]. Typical electron-conductors are zinc oxide (ZnO) and titanium oxide (TiO_2) nanoparticles. The geometry of the devices determines whether a hole or electron transporting layers follows ITO layer (see figure 2.11).

Intermediate layers have a variety of functions. By allowing a single type of charge carrier (positive or negative) to flow to the adjacent electrode, the intermediate layers can prevent charge recombination and may serve as steps for electrons or holes as they transition between active layer and electrodes with mismatched energy levels. In addition, intermediate layers deposited on top of a rough ITO may prevent shunt resistance or alternative paths through which current may flow [39].

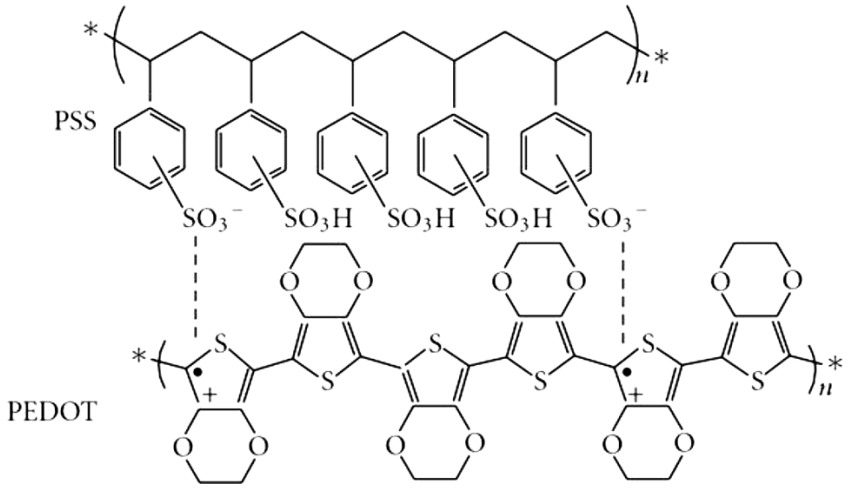

Figure 2.14: The chemical structure of poly 93,4-ethylenedioxythiophene) poly (styrenesulfonate)[40].

2.6.4. Top electrodes

The use of transparent conducting electrode, ITO, at the front of the cell is essential to allow light to travel to the active material. This was discussed in section 2.6.1. Silver (Ag, 5.0 eV) and Gold (Au, 5.1 eV) have high work functions and are exclusively used as anodes. They are usually used as electrodes in the inverted geometry of organic solar cells. Aluminum (Al, 4.1 eV) is a low work function electrode that is always a cathode in a cell. In other cases, a very thin (~ 1 nm) Ca or LiF film evaporated immediately before aluminum has been shown to improve the cell performance [41]. These metals have low work functions. In addition, they serve as protective layers between the Al electrode (which is prone to oxidation) and the organic layer [42].

2.7. The role of the buffer layer in thin film heterojunction solar cells

Inserting metal oxides (ZnO or TiO_2) nanostructures into the interface between the active layer and the cathode electrode in organic solar cells as a buffer layer is regarded as one of the most effective strategies in interface engineering to improve the device performance, in combination with some hole-transporting and electron blocking materials as an anode buffer layer [43]. The device structures of ZnO cathode buffer layer based conventional and inverted are shown in section 2.6, figure 2.11. The primary function of a buffer layer is to form a junction with the absorber layer while admitting a maximum amount of light to the junction region and absorber layer [44]. In addition, this layer should have minimal absorption losses and should be capable of driving out photo generated carriers with minimum recombination losses and electrical resistance. The band gap should be as high as possible and layer should be as thin as possible to maintain low series resistance.

The beneficial effects of the buffer layer ranges from modifying the absorber surface to protecting the sensitive interface during the subsequent deposition of cathode electrode and the favourable properties of the interface are suggested to be related to the match of lattice parameters [45]. The current understanding is that candidates for buffer layers should hold a wide band gap for limited light absorption and the process of deposition should be capable of passivating the surface states of the absorber layer and provide an alignment of the conduction band with the absorber to yield high efficiencies. Buffer layers also enhance the stability of the solar cells as the active layer is usually sensitive to air and this may lead to material degradation due to penetration of oxygen and water molecules through the top electrode.

2.8. Device physics of organic solar cells

2.8.1 General working principle

From the schematic point of view, organic solar cells operate the conversion of the incident solar irradiation to electrical current through essentially a four-step process. The first step is to absorb incident photons, which is affected by the microscopic surface property. Secondly, the electron-hole pair, the so-called excitons are produced. This is directly determined by the material's band structure. The third step is separation of the electron-hole pairs, determined by the charge

distribution inside the cell and then the final step is the generated charges to be collected at their respective electrodes. Figure 2.15 depicts this process. In this view, the donor is termed the holes transporting material and it makes contact with the anode, while the electrons transporting material is the acceptor, which is in contact with the cathode. When a photon incident on the absorber material, it would be either scattered or absorbed. For the latter case, upon absorption of photons, the created excitons will diffuse inside the material to reach the donor-acceptor interface where they will be separated. The donor-acceptor structure accelerates effective dissociation of generated excitons at the interface by internal field effect, which should be > 10^6 V/cm in order to separate electron and holes tightly bound (~ 1 nm distance) by coulomb energy equal to 0.25 eV [46]. This dissociation is limited to a thin interface between the donor and acceptor and is termed the exciton diffusion length. Excitons can be separated if they meet with electric field within their diffusion range (10- 20 nm). If excitons do not reach the interface, they recombine and the absorbed energy is dissipated without generating photocurrent. The internal field exist in the vicinity of junctions and it is due to the thermal equilibrium of the contacted materials. When two materials with different work functions are brought into contact electrons flows from one with lower work function to the other until a Fermi surface match. As a result the internal field is built up near the contact surface. Therefore, to efficiently generate power, the excitons have to be dissociated and charges be efficiently collected to their electrodes [47].

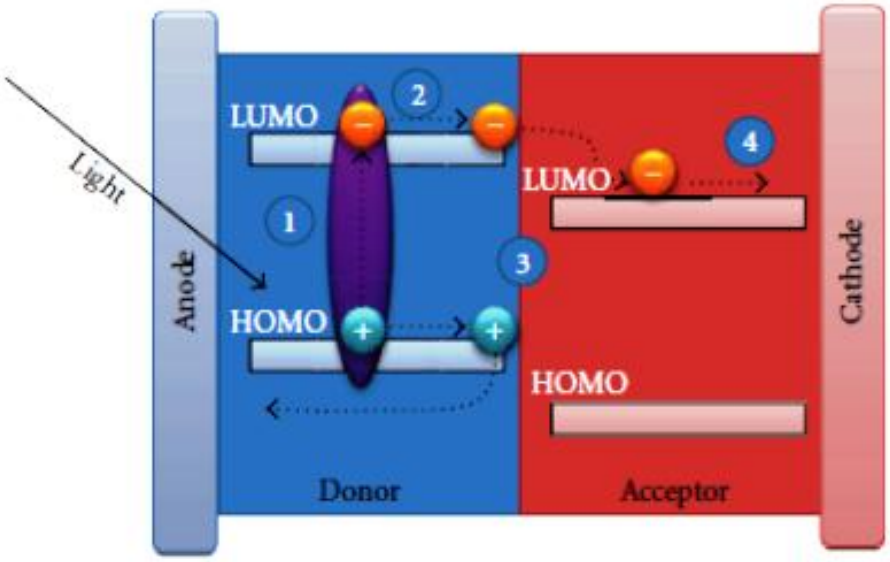

Figure 2.15: Device working principle from light absorption to charge collection [47].

2.8.2 Factors determining the performance of organic solar cells

Firstly, at least one, but preferably both components of the photoactive layer should have a large absorption coefficient and a broad absorption spectrum in order to create a good overlap with the solar emission spectrum. Most conjugated materials are strong absorbers in the visible region with exception of some, such as PCBM. However a considerable amount of solar energy is located at the near infrared region, which causes a non-negligible spectrum mismatch between the photo-response of active layer and solar emission spectrum [48]. In order to make a breakthrough in achieving highly efficient cells, it is important to find donor materials whose photo absorption range better overlaps solar emission.

The band gap of conjugated polymers is mainly determined by its effective conjugated length and functional groups on the main chains. For a given conjugated polymer, the most widely used and effective way to make the absorption spectrum red-shift is to resort to thermal annealing or choosing appropriate solvent to strengthen the inter-chain conjugation [49,50]. But the magnitude of red-shift is quite limited and still far away from our destination if merely these methods can be chosen. Therefore, it is required to develop lower band gap (<1.8 eV) conjugated polymers to completely solve this problem.

Secondly, the donor material should have a high hole mobility, whereas the acceptor should have high electron mobility. Most donor materials are reasonably good hole transporters with hole mobilities μ_h in the range of $10^{-6} – 10^{-3}$ cm^2/Vs [51, 52]. Recent insight suggests that the hole and electron mobility in the mixture does not necessarily reflect the mobility of the pure components, even for compositions where both mobilities should be rather similar to minimize space-charge built-up. Furthermore, the film should have a high dielectric constant, thereby facilitating a high charge density and more efficient exciton dissociation within the film. Typical values for the relative dielectric constant ε_r of conjugated organics are in the range of 3-4 [53].

Thirdly, one of both components should be easily oxidized (the donor), whereas the other one should be easily reduced (the acceptor) [54]. This means that for efficient photoinduced electron transfer from donor to acceptor, the lowest unoccupied molecular orbital (LUMO) of the donor should be located at higher potential energy than the LUMO of the acceptor. Likewise, for efficient photoinduced hole transfer from acceptor to donor, the highest occupied molecular orbital (HOMO) of the acceptor should be located below the HOMO of the donor. In this way,

photoinduced charge transfer can become the main decay mechanism of the excited state that was created by the absorption of light. This charge transfer, however, should not be so facile that it occurs in the ground state, resulting in a stable charge-transfer complex. Furthermore, other decay mechanism than charge transfer should be negligible, such that the excited state (exciton) can diffuse over a long distance to the interface between the donor and acceptor without decay [55].

Fourth, material design of both donor and acceptor should allow for a large open-circuit voltage (V_{oc}). The open circuit voltage is related to the distance between the HOMO level of the donor and LUMO level of the acceptor [56]. Additionally, the position of the LUMO level of the acceptor with respect to the work function or Fermi-level (E_F) of the electron collecting electrode should provide easy electron collection at the contact. The same holds for the HOMO of the donor with the hole collecting electrode. Proper choice of electrode materials should ensure efficient charge collection at the contacts. The importance of proper choice of electrode materials to improve performance has been extensively demonstrated in the field of organic solar cells [57]. The difference in effective work function between both electrodes should provide the built-in electric field necessary to extract the photo generated charges.

Apart from the opto-electronic properties, the materials should allow facile processing from solution. Additionally, they should allow easy purification after synthesis. Preferably, the glass transition temperature T_g should be far above room temperature to form a stable morphology and for conjugated polymers, the T_g typically lies above 65^{o}C. The materials should be chemically stable. Photo-oxidation is known to occur, but can be prevented to a large extent by proper device processing and encapsulation. Finally, the film morphology should ensure good percolation pathways for efficient charge collection and minimal charge recombination. The influence of morphology (particularly that of ZnO buffer layer) on the performance of organic solar cells is a subject of chapter 6.

2.9. Efficiency characteristics

2.9.1 Photovoltaic parameters

The performance of organic solar cells is characterized by measuring the current density to voltage (J-V) characteristics under illumination with the AM1.5G solar spectrum (100 mW/m^2). The term AM1.5G (air mass 1.5 global) refers to the mass of air that solar light has to travel through being 1.5 times larger than the light incident at zenith (i.e. on a surface facing the sun with a solar zenith angle of 48.2^o) at a cell temperature of 25^{o}C [58,59]. This is depicted in figures 2.16 (a) and (b). The directly measurable parameters of a solar cell are the short-circuit current density (J_{sc}), the open circuit voltage (V_{oc}), the fill factor (FF), the power conversion efficiency (η_p/ PCE) and the incident photon to current efficiency (IPCE) also known as the external quantum efficiency (EQE).

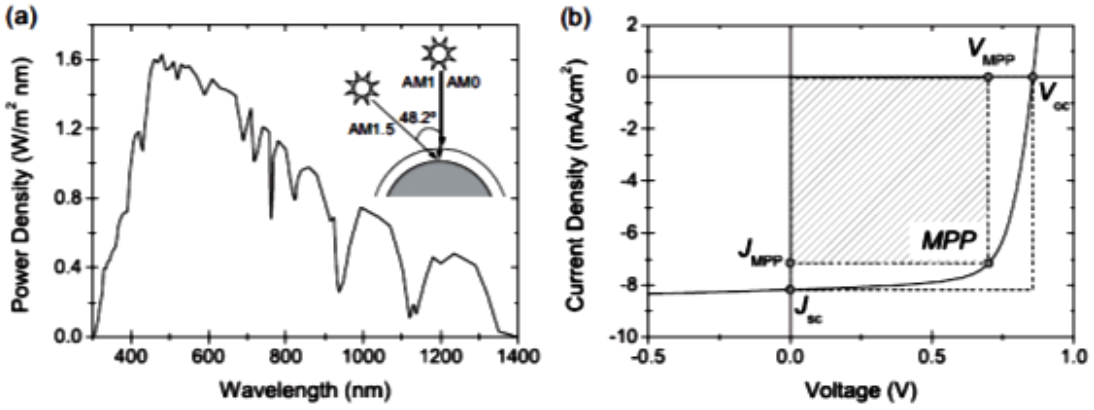

Figure 2.16: (a) AM1.5G solar spectrum, the insert shows the angle of incidence of the spectrum, (b) typical J-V characteristics of the solar cell with indication of the short-circuit current density (J_{sc}), the open-circuit voltage (V_{oc}) and the maximum power point (MPP) with the corresponding current density (J_{MPP}) and Voltage (V_{MPP}) [58].

- **Open-circuit voltage, V_{oc}**

  The voltage at which no current flows through a solar cell is called open circuit voltage. Several studies have demonstrated a strong dependence of V_{oc} on the energy difference between the HOMO-LUMO offset at the donor-acceptor interface of an organic solar cell [60,61]. However, the experimental values for V_{oc} can differ depending on the material system.

- **Short-circuit current density, J_{sc}**

  For V= 0 only the short-circuit current density J_{sc} flows through the solar cell which is purely based on photo generated charge carriers. Thus, for monochromatic exposure the spectral dependence of the charge carrier generation can be measured [62].

- **Maximum power point, P_{max}**

  The maximum power point is the point that maximize J_{max} x V_{max} product, hence maximizes the power. That is the load that can deliver maximum electrical power at the level of irradiation. In figure 2.16(b), V_{MPP} and J_{MPP} show the maximum power point. The power is zero at V_{oc} and J_{sc} [62].

- **Fill Factor, FF**

  Fill Factor of the device is the ratio of the maximum power generated in the device and $V_{oc} \times J_{sc}$ i.e. the ratio between the dark and bright shaded areas in figure 2.16(b). Therefore, it s given by [62]:

$$FF = \frac{P_{max}}{J_{sc}V_{oc}} \quad (1)$$

  Fill factor is an indicator of the quality of the solar cell and is significantly determined by the serial electrical resistance of the cell and therefore by mobilities of charge carriers in the organic layers of the cell. Typical values for the FF are found to be 0.75 to 0.85 in inorganic solar cells and 0.55 to 0.7 for organic solar cells.

- **Incindent photon-to-current efficiency (IPCE) or External quantum efficiency, (EQE)**

  The incident photon-to-current efficiency is defined as the ratio of the number of incident photons N_{photon} and the number of photo induced charge carriers N_{charge} which can be extracted out of the solar cell. It is smaller than the internal quantum efficiency which represents the conversion of absorbed photons into charge carriers within the cell. The reason for this is that IPCE takes into account the losses by reflection, scattering and recombination. In contrast to the internal quantum efficiency, which can achieve values

up to 100%, the IPCE yield can be directly determined from the J_{sc} and the Incident light power P_{in} [62].

$$IPCE = \frac{N_{charge}}{N_{photon}} = \frac{J_{sc}}{P_{in}} \times \frac{hc}{\lambda q}, \quad (2)$$

where q is the single electron charge, c is the speed of light, λ is the wavelength of the incident light and h is the planck constant.

- **Power conversion efficiency, η_p/ PCE**

  The power conversion efficiency is the maximum electrical power P_{max} per light input $P_{in.}$

$$\eta_p = \frac{P_{max}}{P_{in}} = \frac{J_{sc} V_{oc}}{P_{in}} FF \quad (3)$$

  For an efficient device a large fill factor, a large short-circuit current and a large open circuit voltage is needed. It is not sufficient to optimize only one of these parameters for efficient photovoltaics cells. Since the electrical response of the solar cell on the incident light is strongly dependent on its spectrum, standardized solar simulators which simulate an AM1.5G spectrum are used for device characterization [62].

2.9.2 Equivalent circuit, series and shunt resistances

In real cells power is dissipated through the resistance of the contacts and through leakage currents around the sides of the device. Figure 2.17 shows the equivalent circuit for a typical organic solar cell comprising of the following [63]:

- Current source that represents the photocurrent generated within the cell. This current flow in the opposite direction compared to the forward equivalent diode and depends on the voltage across the device.
- The dark current diode which is in the inverse direction with respect to the current source
- A series resistance (R_s) that gathers the ohmic contributions of the electrode and the contact between the organic semiconductor and the metal. The series resistance arises from the resistance of the cell material to the current flow, particularly through the front surface to the contacts and from sensitive contacts. It is a particular problem at high

current densities, for instance under concentrated light. R_s have to be lowered to ensure a maximum efficiency [63].

- The parallel or shunt resistance (R_{sh}) which arises from the leakage of current through the cell, around the edges of the device and between contacts of different polarity. Unlike R_s, R_{sh} has to be maximized to reach high efficiency cells. This resistance is typically due to manufacturing defects, rather than poor solar cell design. Low shunt resistance causes power losses in solar cells by providing an alternate current path for the light generated current. Such a diversion reduces the amount of current flowing through the solar cell junction and reduces the voltage from the solar cell. The equation for current density of this circuit is given by,

$$J = J_l - J_0\left(e^{\frac{q(V+JR_S)}{nkT}} - 1\right) - \frac{V+JR_S}{R_{sh}}, \qquad (4)$$

where J_l is the current density of the load, J_0 is the diode's saturation current density, q is the electron's charge, n is the diode's ideality factor, K is Boltzmann's constant, T is the temperature, R_s is the series resistance and R_{sh} is the shunt resistance [64].

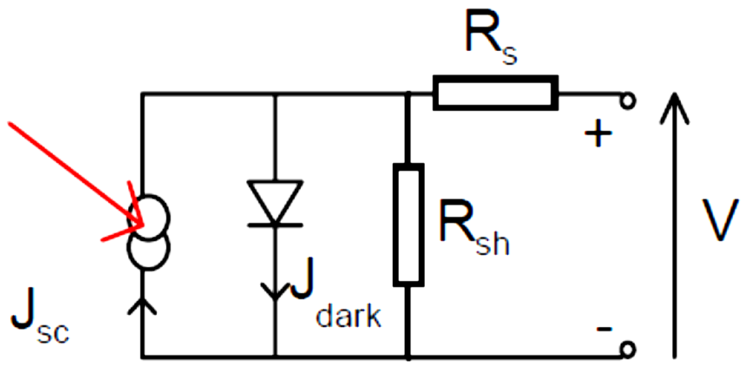

Figure 2.17: An equivalent circuit of a solar cell including series and shunt resistances [64].

As shown in figure 2.18, for efficient cell R_s has to be small and R_{sh} to be as large as possible. The values of R_s and R_{sh} can be determined independently from the inverse slope of the J-V curve of the device at $I=J_{sc}$ ($V=0$) and $V=V_{oc}$ ($I=0$), respectively. This is illustrated in figure 2.19

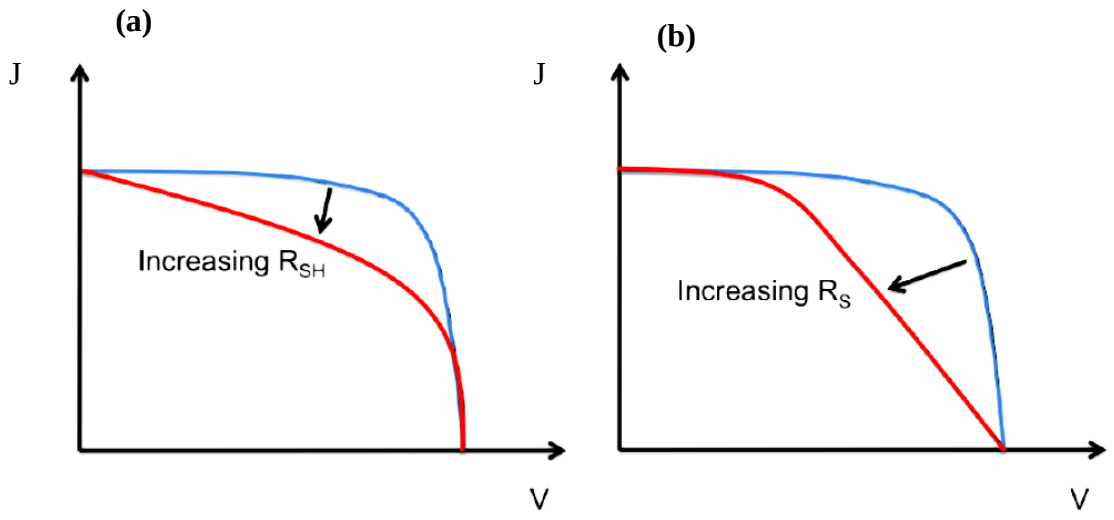

Figure 2.18: The effect of (a) increasing shunt resistance (R_{sh}) and (b) Increasing series resistance (R_s) on the solar cell's J-V curve [65].

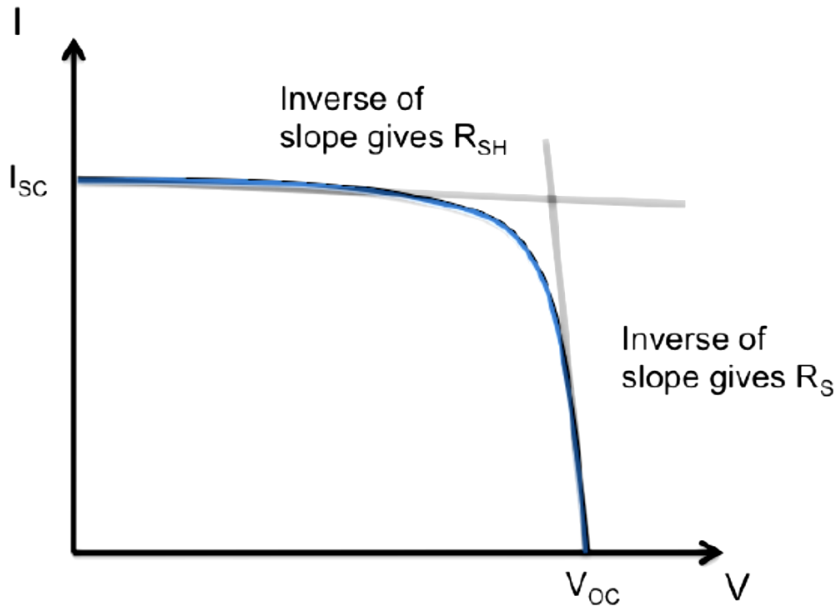

Figure 2.19: Determining R_s and R_{sh} using J-V curves [65].

2.10. Uses of solar cell technology

Solar technology is integrating its flexible thin-film photovoltaic devices in jackets. These jackets will allow consumers to carry, connect and charge their portable digital devices in one convenient and fully integrated package. Figure 2.20, shows the solar cell jacket whereby the solar panels are strategically mounted and wired providing solar power to individual's devices for power storage (charging) or immediate consumption [66].

The solar cell panel at the back of the jacket will convert the sun's photons into energy, which will feed the hidden battery pack charger about a size of a deck of cards in the lining of a jacket. The charge pack is also wired to all the pockets to power mobile devices such as cell phones and MP3 players. In addition, photovoltaic technology uses includes portable devices that needs power supply such as global positioning system (GPS) and smart fabrics such as camping gear. Other ideal solar cells applications include solar cell-covered sails for sailboats, rucksacks and tents. These are shown in figure 2.21.

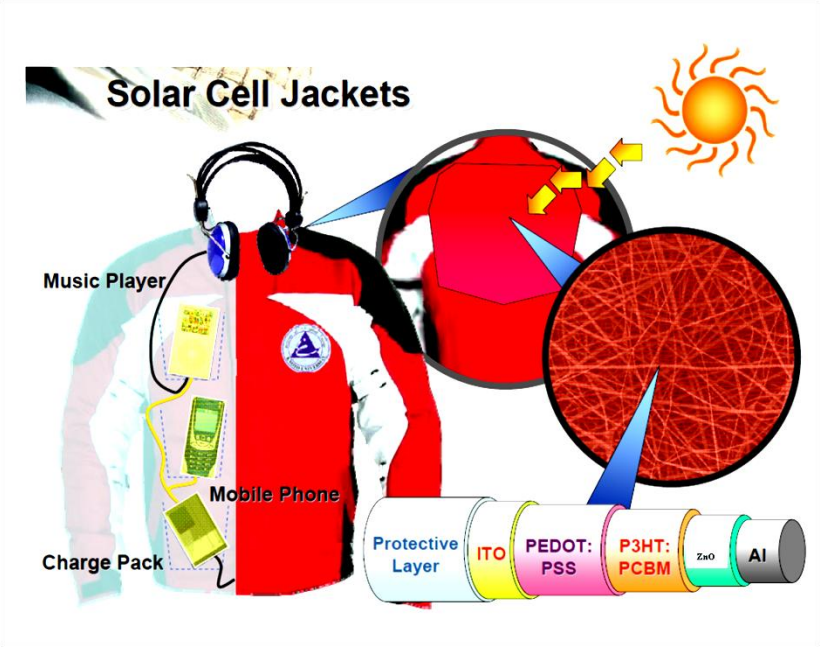

Figure 2.20: Solar cell powered jacket [66].

Figure 2.21: (a) Solar cell-covered sails of sailboats, (b) solar cells-covered Rucksacks and (c) solar cell-covered tents [66].

References

[1] Jenny Nelson, *Physics of Solar Cells*, website: http://www.worldscibooks.com/physics/p276.html [Accessed on November 2011]

[2] Deshmukh C. and Shyamala Venkataraman, *100 years of Einstein's Photoelectric Effects*, http://www.physics.iitm.ac.in/~labs/amp/EPEE_PCD_SV.pdf [Accessed on November 2011]

[3] http://photovoltaics.sandia.gov/docs/PVFEffIntroduction.htm [Accessed on November 2011]

[4] Inna Stukova and Nathan Harris, *Design of Organic Solar Cells*, Department of Electrical and Computer Engineering, Old Dominion University, Virginia.

[5] http://www.renewable-energy-concepts.com/solarenergy/solar-basics.html [Accessed on November 2011]

[6] http://www.facts-about-solar-energy.com/solar-energy-history.html [Accessed on November 2011]

[7] http://org.ntnu.no/solarcells/pages/history.php [Accessed on November 2011]

[8] Russel H. Varian, *Physical Review*, **46** (1934) 1051-1054

[9] John Perlin, The Silicon Solar Cell Turns 50. http://www.nrel.gov/docs/fy04osti/33947.pdf [Accessed November 2011]

[10] John N. Shive, a handbook, *Properties, Physics and Design of Semiconductor devices,*United States (2011)

[11] M. Wolf, *Historical Development of Solar Cells*, Proceedings of the 25th Power Sources Symposium.,23–25 May 1972, pp. 120–124.

[12] Martin A. Green, *The Path to 25% Silicon Solar Cell Efficiency: History of Silicon Cell Evolution, Progress in Photovoltaics,* **17**(2009) 183-189

[13] http://www.top-alternative-energy-sources.com/solar-cells.html [Accessed on November 2011]

[14] http://www.solar-facts-and-advice.com/solar-cells.html [Accessed on November 2011]

[15] http://en.wikipedia.org/wiki/Solar_cell [Accessed on November 2011]

[16] Harald Hoppe and Niyazi Serdar Sariciftci, *Journal of Materials Research*, **19** (2004) 1924-1945

[17] Travis L. Benanti and D. Venkataraman, *Photosynthesis Research*, **87** (2006) 73-81

[18] Peet J, Kim J Y, Coates N E, Ma W L, Moses D, Heeger A J and Bazan G C,*Nature Materials* **6** (2007) 497-500

[19] Park S H, Roy A, Beaupre S, Cho S, Coates N, Moon J S, Moses D, Leclerc M, Lee K and Heeger A J, *Nature Photon,* **3** (2009) 297-302

[20] Green M A, Emery K, Hishikawa Y and Warta W, *Progress in Photovoltaics,* **18** (2010) 144-150

[21] Vishal Shrotriya, Gang Li, Yan Yao, Tom Moriarty, Keith Emery and Yang Yang, *Advanced Materials,* **16** (2006) 2016-2023

[22] Carsten Diebel and Vladimir Dyakonov, *Report on Progress in Physics,* **73** (2010) 096401 doi: 10.1088/0034-4885/**73**/9/**096401**

[23] J.J Halls and R.H Friend, *Organic Photovoltaic Devices, in clean electricity from photovoltaics*, M.D. Archer and R.Hill, Editors. 2011. Imperial College Press, London

[24] http://en.wikipedia.org/wiki/Organic_solar_cell [Accessed on December 2011]

[25] Hertel D and Baessler H, *Journal of Chemical Physics and Physical Chemistry,* **9** (2008) 666-688

[26] Tang C.W, *Applied Physics Letters,* **48** (1986) 183-185

[27] Yu G, Gao J, Hummelen J.C, Wudl F and Heeger A. J, *Sciences* **270** (1995) 1789-1791

[28] R. Janssen, J.C Hummelen and N.Sariciftci, *MRS Bulletin* **30**(2005) 33-35

[29] J.D Myers and J. Xue, *Polymer Reviews* **52**(2012) 1-37

[30] W. Brutting (Chapter Edition), *The Physics of Organic semiconductors*, Wiley-VCH, Weinheim,(2005).

[31] H. Spanggaard and F.C Krebs, *Solar Energy Materials and Solar Cells* **83**(2004) 125-146

[32] L. Qian, J. Yang, R. Zhou, A. Tang, Y. Zheng, T.-K. Tseng, D. Bera, J. Xue and P. Holloway, *Journal of Materials Chemistry* **21** (2011) 3814-3817

[33] K. Bedeker, *Annals of Physics* **22** (1907) 749-766

[34] B.M. Graham, Dissertation, *Department of Material Science and Engineering, University of Toronto,* 2010.

[35] B. Zhang, D.-H. Lee, H. Chae, C. Park and S.M Cho, *Korean Journal of Chemical Engineering* **27**(2010) 999-1002

[36] C. Woo, B. Thompson, B. Kim, M. Toney and J. Frechet, *Journal of American Chemical Society* **130** (2008) 16324-16329

[37] L. Klimov, W. Li, X. Yang, G.G Hoffmann and J. Loos. *Macromolecules* **39** (2006) 4493-4496

[38] M. Girtan and M. Rusu, *Solar Energy Materials and Solar Cells*, **94** (2010) 446-450

[39] F.C. Krebs. *Polymeric Solar Cells: Materials, Design, Manufacture*. DEStech Publications, Inc., Lancaster, Pennsylvania, 2010.

[40] J. Li, J. Liu, C. Gao, J. Zhang, and H. Sun, *International Journal of Photoenergy*, Volume 2009, Article ID 650509, 5 pages.doi:10.1155/2009/650509

[41] V.Singh, A. K. Thakur, S. S. Pandey, W. Takashima, and K. Kaneto. *Organic Electronics*, **9** (2008) 790-796

[42] L. S. Hung, C. W. Tang, and M. G. Mason, *Applied Physics Letters*, **70**(1996) 152-154

[43] J. Huang, Z. Yin and Q.Zheng, *Energy and Environmental Science*, **4**(2011) 3861-3877

[44] B.E McCandless and S.S Hegedus, *Proceedings of the 22nd IEEE Photovoltaic Specialists Conference* (1991) 967-972

[45] J. Sterner, *Comprehensive Summaries of Uppsala Dissertations from the Faculty of Science and Technology*, 942 (2004) 14.

[46] B.A Gregg and M.C Hanna, *Journal of Applied Physics*, **93**(2003) 3605-3614

[47] G. Chidichimo and L. Filippelli, *International Journal of Photoenergy*, Doi:10.1155/2010/123534

[48] L. Ligui, L. Guanghao, Y. Xiaoniu and Z. Enle, *Chinese Science Bulletin* **52**(2007)145-158

[49] Y.N Yang, J. Loos and R.A. J Janssen, *Nano Letters* **5**(2005) 579-583

[50] S.E Shaheen, C.J Brabec and N.S Sariciftci, *Applied Physics Letters* **78** (2001) 841-843

[51] C.D Dimitrakopolous and P.R.L Malenfant, *Advanced Materials* **14**(2002) 99-117

[52] A.M Stonehan, M.M. B Ramos, A.M Almeida, H.M.G Correia, R.M Ribeiro, H. Ness and A.J. Fisher, *Journal of Physics:Condensed Matter* **14**(2002) 9877-9898

[53] P.W.M Blom and M.C.J.M Vissenberg, *Materials Science and engineering* **27**(2000) 53-94

[54] P. Peumans, A. Yakimov and S.R Forrest, *Journal of Applied Physics* **93**(2003) 3693-3723

[55] J.J.M Halls, K. Pilchler, R.H Friend, S.C Moratti and A.B Holmes, *Applied Physics Letters* **68**(1996) 3120-3122

[56] V.D Michailetchi, P.W.M Blom, J.C Hummelen and M.T Rispens, *Journal of Applied Physics* **94** (2003) 6849-6854

[57] T.M Brown, J.S Kim, R.H Friend, F. Cacialli, R. Daik and W.J Feast, *Applied Physics Letters* **75**(1999) 1679-1681

[58] American Society for Testing and Materials (ASTM) standard G173-03. Source: http://rredc.nrel.gov/solar/spaectra/aml.5/. [Accessed 1 December 2011]

[59] J.M Kroon, M.M Wienk, W.J.H Verhees and J.C Hummelen, *Thin Solid Films* **223**(2002) 403-404

[60] C. Brabec, A. Cravion, D. Meissner, N. Sariciftci, T. Frommherz, M.Rispens, L.Sanchez, and J. C. Hummelen. *Advanced Functional Materials,* **11** (2001) 374

[61] A. Gadisa, M. Svensson, M. Andersson, and O. Inganas, *Applied Physics Letters* **84** (2004) 1609-1611

[62] T.L Benanti and D. Venkataraman, *Photosynthesis Research* **87**(2006) 73-81

[63] S. Ebadian Thesis, *The University of British Columbia*, July 2009

[64] The physics of Solar Cells, http://www.worldscibooks.com/physics/p276.html [Accessed December 2011]

[65] National Instruments. Part ii –Photovoltaic cell I-V characterization theory and lab view analysis code. Development zone. URL: http://zone.ni.com/devzone/cda/tut/p/id/7230 [Accessed December 2011]

[66] http://www.gizmag.com/go/2522 [Accessed December 2011]

3 Research Techniques and device fabrication

3.1. Introduction

In this chapter the research techniques used in this study are discussed. Sample preparation and device (conventional and inverted) fabrication are also discussed in detail. The structure of nanoparticulate ZnO, particle morphology, surface topography and optical absorption were studied using X-ray diffraction (XRD, Bruker AXS D8 Advanced), field-emission scanning electron microscopy (FE-SEM, Nova-nano SEM^{200}, FEI), transmission electron microscopy (TEM, CM30, Philips), atomic force microscopy (AFM, Shimadzu SPM-9600) and UV-Vis spectrometer Perkin – Elmer Lambda 35 UV-Vis-NIR, respectively. The current density-voltage (J-V) curves were measured in air using a Keithley 2400 source meter and an Oriel xenon lamp (150 W) coupled with an AM1.5 filter to simulate sunlight. The light intensity was calibrated with a silicon reference cell with KG2 filter following the standard solar cell testing procedures. All J-V measurements were conducted at the light intensity of 100 mW/cm^2. The external quantum efficiencies (EQE) as a function of wavelength were measured using an incident photon-to-current efficiency (IPCE) measurement system (PV measurements, Inc). The wavelength of the bias light was controlled with optical filters (Andover Corporation). The surface imaging and depth profiling were performed by Time-of-flight Secondary Ion Mass Spectrometry (TOF-SIMS).

3.2. Characterization Techniques

3.2.1 X-ray Diffractometer

X-ray diffraction (XRD) is a popular and powerful technique used to determine crystal structure of materials. During XRD analysis, a collimated X-ray beam of a specific wavelength is directed to the sample and the angles at which the beam is diffracted are measured [1]. The crystalline phase of a material can also be identified by examining the diffraction patterns. The widths of the

diffraction lines are closely related to the size, size distribution, defects and strain in nanocrystals [2]. As the size of the nanocrystal decreases, the line width is broadened due to loss of long range order relative to the bulk. The average crystallite size, *D*, can be estimated from the broadened peaks by using the Debye-Scherrer equation given by [3]:

$$D = \frac{0.9\lambda}{\beta cos\theta}, \tag{3.1}$$

where β is the full width at half maximum of a diffraction line located at angle θ while λ is the X-ray diffraction wavelength (0.154 nm). The schematic diagram of the XRD system with an X-ray tube, the flat specimen holder and goniometer circle which remains constant throughout the analysis and is defined by the position of the target is shown in figure 3.1. The X-ray tube, specimen and receiving slit lie on the arc of the focusing lens. The incident angle, a filter which is used to remove all but the desired Kα radiation and a slit on the incident beam side which is used to narrow the beam so that it is confined to the area of the specimen are also shown on the figure.

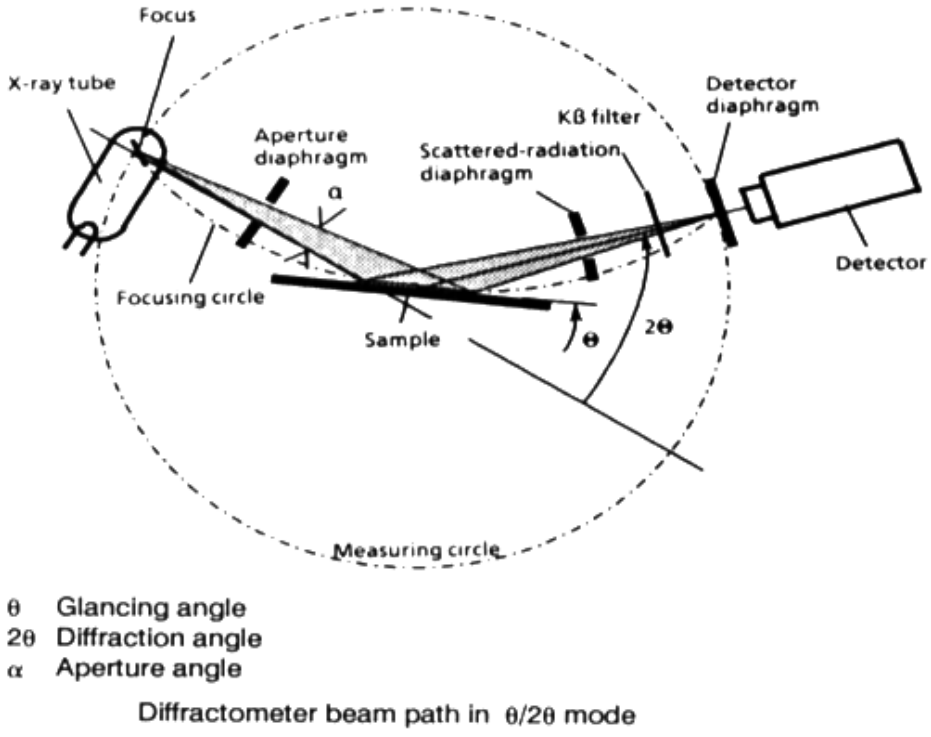

Figure 3.1: Schematic diagram of the X-ray diffractometer system [4].

3.2.2. Transmission electron microscopy

Transmission electron microscopy is an imaging technique in which a beam of electrons is transmitted through a specimen, and then an image is formed. The image is then magnified and directed to appear either on a fluorescent screen or layer of photographic film, or is detected by a sensor such as a CCD camera [5]. The system can study small details in different materials down to near atomic levels [6]. It can investigate the size, shape and arrangement of the particles which make up the sample as well as their relationship to each other on the scale of atomic diameters. Materials to be analyzed with this technique need to have dimensions small enough to be electron transparent and that can be produced by the deposition of a dilute suspension containing the sample onto support grids. The suspension is normally a volatile solvent such as ethanol that can evaporate to allow the sample to settle on the grids.

Figure 3.2 shows the schematic diagram of the transmission electron microscopy, with an electron gun which provides the source of illumination, electromagnetic lenses which focus the electron beam and then magnify the image. It also consists of apertures, which limit the angular spread of the beam and are crucial in controlling contact. An image is formed by accelerating a beam of electrons that pass through the specimen. These electrons are scattered at different angles depending on the density of the atom it encounters. An electron can either be (a) undeflected, (b) deflected but loses no energy (elastically deflected), or (c) loses a significant amount of energy and is probably deflected (inelastically). The different scattered angles produce a contrasting image because all angles scattered more than 0.5 degrees are stopped by an objective aperture situated below the specimen. The image is projected on a fluorescent screen where phases, fractures and other properties that are 2 to 3Å across can be seen [5]

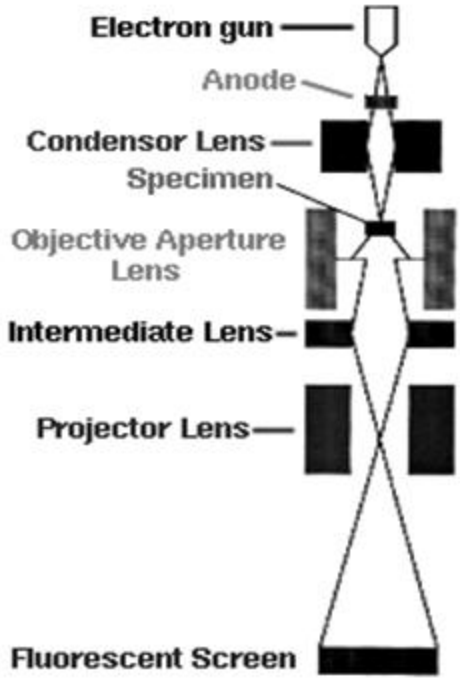

Figure 3.2: Schematic diagram of TEM [7].

3.2.3. Field-emission scanning electron microscopy

Field-emission scanning electron microscopy is a technique in which a beam of energetically well-defined and highly focused electrons is scanned across a material (sample). The technique can provide material's information about topography and morphology [8]. If the system is equipped with energy dispersive x-ray spectrometer (EDS), it can also provide information about chemical composition of the material [9]. FE-SEM uses the field emission source producing a clearer image, less electrostatic distortions and spatial resolution < 2 nm. The basic principle of the system is that, the electron beam impinges the surface and generates a splash of electrons with kinetic energies much lower than the primary incident electrons called secondary electrons.

An image of the sample surface is constructed by measuring secondary electron intensity as a function of the primary beam position. The FE-SEM has many advantages over traditional light microscopes. It has large depth of field, which allows more of a specimen to be in focus at one time. It also has much higher resolution, such that closely spaced specimens can be magnified at much higher levels. Because it uses electromagnets rather than lenses, the user has much more control in the degree of magnification. All of these advantages, as well as the actual strikingly clear images, make the scanning electron microscope one of the most useful instruments in

research today [10]. A simplified layout of a SEM is shown in Figure 3.3, consisting of an electron gun, magnetic lens used to form the beam and limit the amount of current in the beam and detectors. Electrons are produced via a thermionic emission from an electron gun and focused down to a spot on the specimen by a system of ion optics (i.e. electromagnetic coils). A set of scan coils are used to scan the spot over the surface of the sample and reflected electrons are collected, amplified and converted into a video signal. Thus, a micrograph of the specimen is obtained in the form of a 2D plot of the reflected spot.

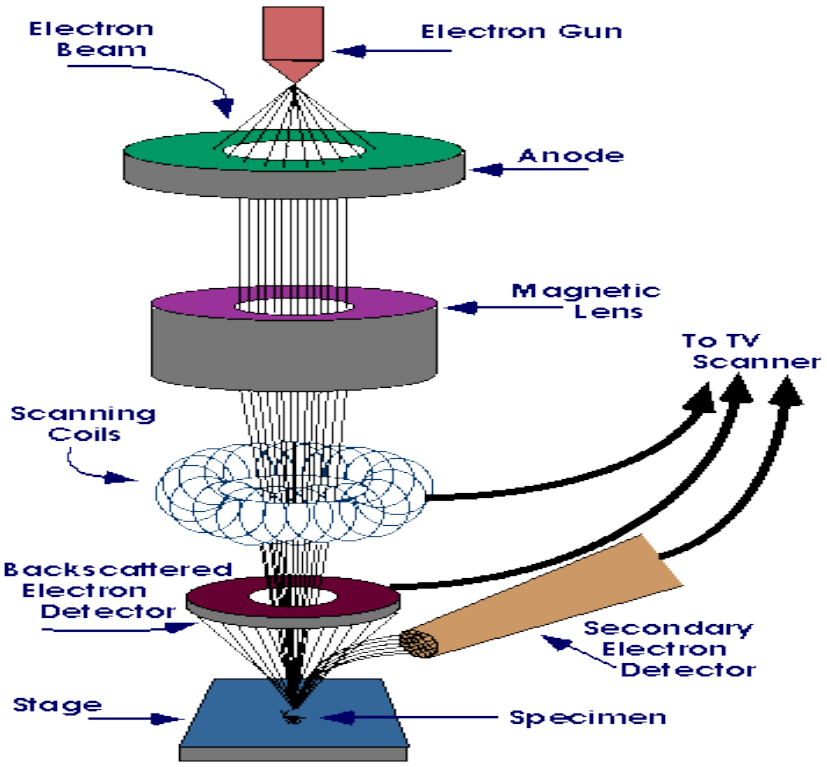

Figure 3.3: A simplified layout of a SEM [10].

3.2.4. Atomic force microscopy

The atomic force microscopy uses a probe, silicon tip and cantilever spring to record the surface topography of samples. While scanning, the force between the tip and the sample is measured by monitoring the deflection of the cantilever. The deflection is controlled by using the optical lever technique. A beam from a laser diode is focused onto the end of the cantilever and the position of the reflected beam is monitored by a position sensitive detector (PSD) [11]. A topographic image of the sample is obtained by plotting the deflection of the cantilever versus its position on the sample. Alternatively, it is possible to plot the height position of the translation stage. This height is controlled by a feedback loop, which maintains a constant force between the tip and the sample. Atomic force microscopes can be operated in air, different gases, vacuum or liquid. The AFM can also be operated in three modes, namely, the contact, non-contact and tapping mode [12]. Figure 3.4 shows the schematic diagram of AFM.

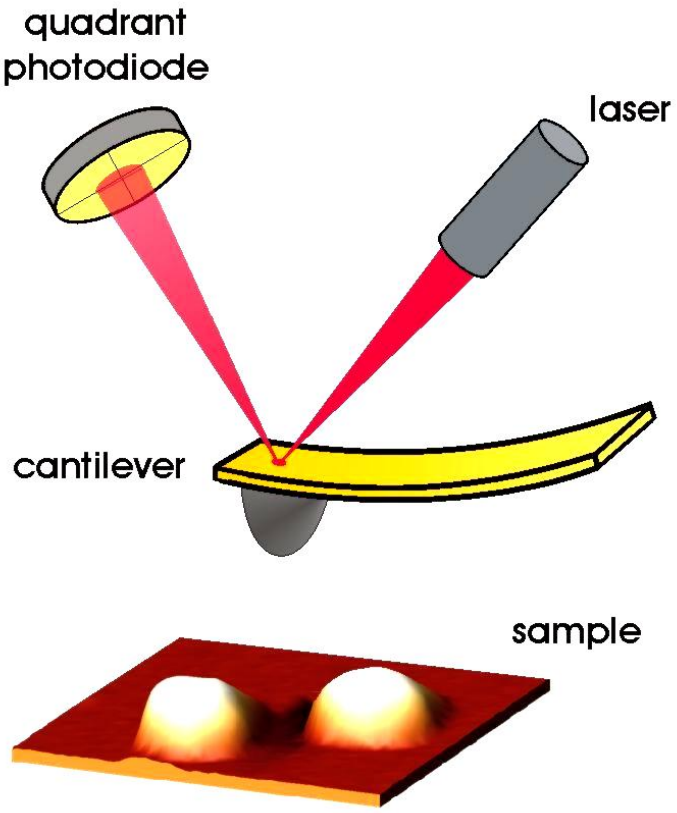

Figure 3.4: Schematic diagram of AFM [13].

3.2.5. UV-VIS Spectrometer

UV-Vis spectrophotometry is a technique which measures the intensity of light passing through a sample (I) and compares it to the intensity of the light before it passes through a sample (I_0). The ratio I/I_0 is called the transmittance, and is usually expressed as a percentage (%T). The absorbance, A, is based on the transmittance:

$$A = -\log(\frac{\%T}{100}) \quad (3.2)$$

The UV-Vis spectrometer can be configured to measure reflectance and can also be either single or double beam [14]. The basic parts of the spectrophotometer are a light source, a holder of a sample, a diffraction grating or monochromator to separate the different wavelengths of light, and a detector. The radiation source is often a Tungsten filament (300-2500 nm) and a deuterium arc lamp which is continuous over the ultraviolet region (190-400 nm). The detector is typically a photodiode or a charge coupled device (CCD). Photodiodes are used with monochromators, which filter the light so the only light of a single wavelength reaches the detector. Diffraction gratings are used with CCDs, which collects light from the different wavelengths on different pixels [15]. Figure 3.5 shows the simplified layout of a typical double beam UV-Vis Spectrophotometry.

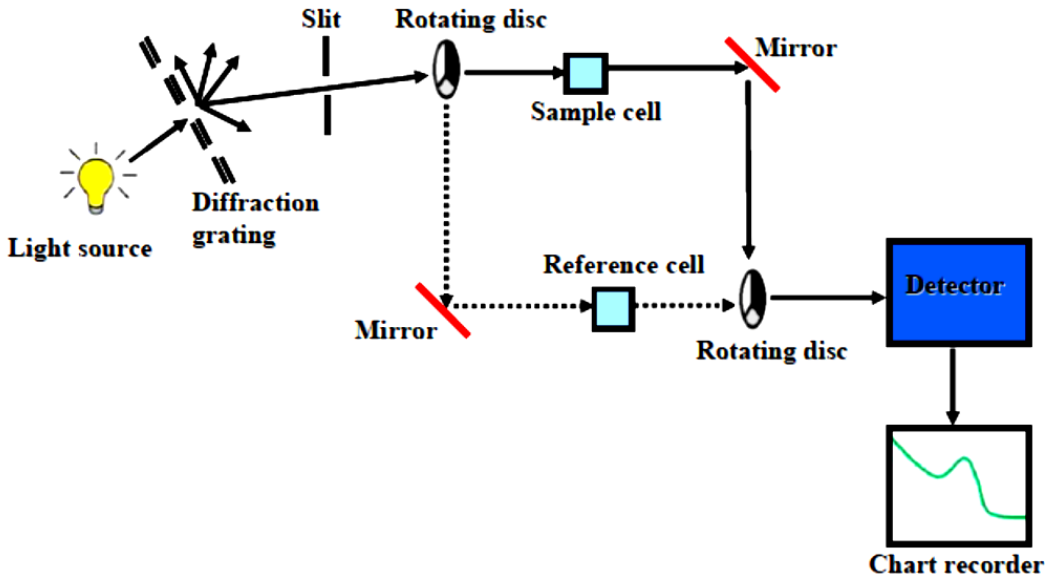

Figure 3.5: A simplified optical layout of a typical double-beam UV-Vis spectrophotometry [16].

3.2.6. Keithley 2400 source meter

The organic solar cells in this study were characterized by Keithley source meter. It is a source measurement unit (SMU) instrument designed specifically for test applications that demand tightly coupled sourcing and measurements. A LabView VI software is adjusted in order to output the open circuit voltage, short circuit current, maximum power, fill factor and efficiency of the cell [17]. The source meter is used with an Oriel Xenon lamp (150 W) coupled with an AM1.5 filter to simulate sunlight. The light intensity is calibrated with a silicon reference cell with KG2 filter following the standard solar cell testing procedures.

Proper integration between software, solar simulator and reference cell is necessary to achieve accurate repeatable data to calculate the PV-cell efficiency. Once the solar simulator and other instruments are turned on and the solar cell is placed beneath the simulator, the software will open the solar simulator shutter, sweep the voltage across the prescribed range, measure the current and display the J-V curve on the computer. Then the software calculates the PV parameters including the power conversion efficiency. Figure 3.6 shows the Keithley 2400 source meter.

Figure 3.6: A Keithley Source meter [18].

3.2.7. Incident photon-to-current efficiency (IPCE or EQE)

Measuring the photovoltaic response of a solar cell to monochromatic light provides information about how efficiently the cell converts photons of a given wavelength into electrons. An IPCE/EQE monochromator provides light of every narrow bandwidth (nearly monochromatic) and a measurement of the power at each wavelength can be used to calculate the number of photons that are generated. If this light is incident on a solar cell the output current generated by the solar cell (with zero bias voltage) can be used to calculate the number of electrons that are generated.

The monochromator's emission range is from 300 to 1000 nm. A 150 Watt Xe arc lamp is used to generate the light needed for the monochromator. In a Xe lamp the light is produced as high energy electrons pass through Xe gas forming a small cloud of plasma. The light emitted from this plasma has a very similar irradiance spectrum to sunlight, with the exception that there are spectral emission lines associated with the gas. These lines are significant, especially in the region from 850-900 nm. The IPCE monochromator uses a grating and slits to reduce the Xe lamp's spectral output to nearly monochromatic light (Figure 3.7). The output is therefore light of a given wavelength at a measurable intensity.

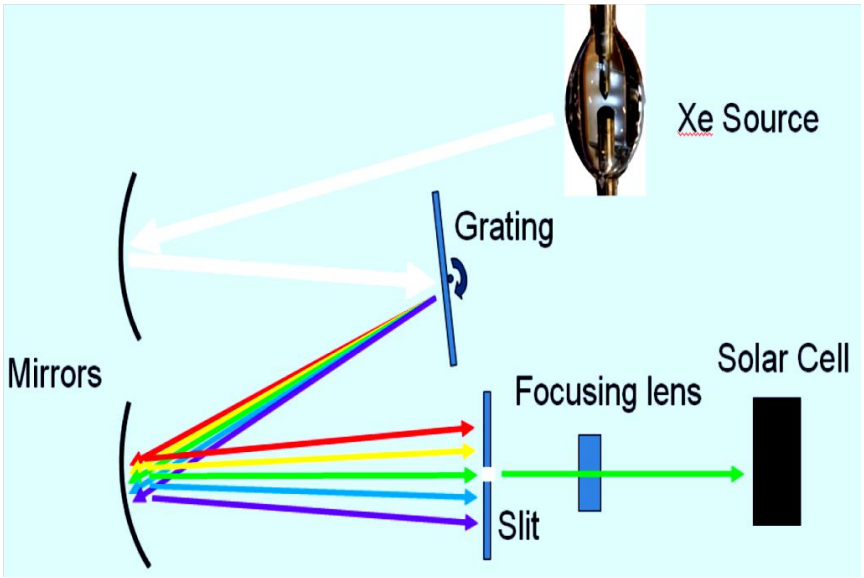

Figure 3.7: Simplified schematic diagram of the IPCE layout.

3.2.8. Time-of-flight Secondary Ion Mass Spectrometry

The technique TOF-SIMS is a surface sensitive characterization method that uses a pulsed ion beam (typically Cs, Ar or Ga) to remove molecules from the outermost surface of the sample. The particles are removed from atomic monolayers on the surface (secondary ions). These particles are then accelerated into a flight tube and their mass is determined by measuring the exact time at which they reach the detector on a scale of nano-seconds (i.e time of flight). It is possible to produce a mass resolution as fine as atomic mass units, i.e. one part in a thousand of the mass of a proton. Three operational modes are available using TOF-SIMS, namely, surface spectroscopy, surface imaging and depth profiling. TOF-SIMS instrument typically includes the following [19]:

- An ultrahigh vacuum system, which is needed to increase the mean free path of ions liberated in the flight path,
- A particle gun, that typically uses a Ga or Cs source,
- The flight path, which is either circular in design, using electrostatic analyzers to direct the particle beam or linear using a reflecting mirror and
- The mass detector system.

TOF-SIMS instruments are also equipped with a computer and software for system control and analysis. One of the key features of the TOF-SIMS software is the ability to perform retrospective analysis, that is, every molecule from the sample detected by the system can be stored by the computer as a function of the mass and its point of origin. This allows the user to obtain chemical maps or spectra of specific regions not previously defined after the original data have been cancelled [19]. The schematic diagram of TOF-SIMS is shown in Figure 3.8.

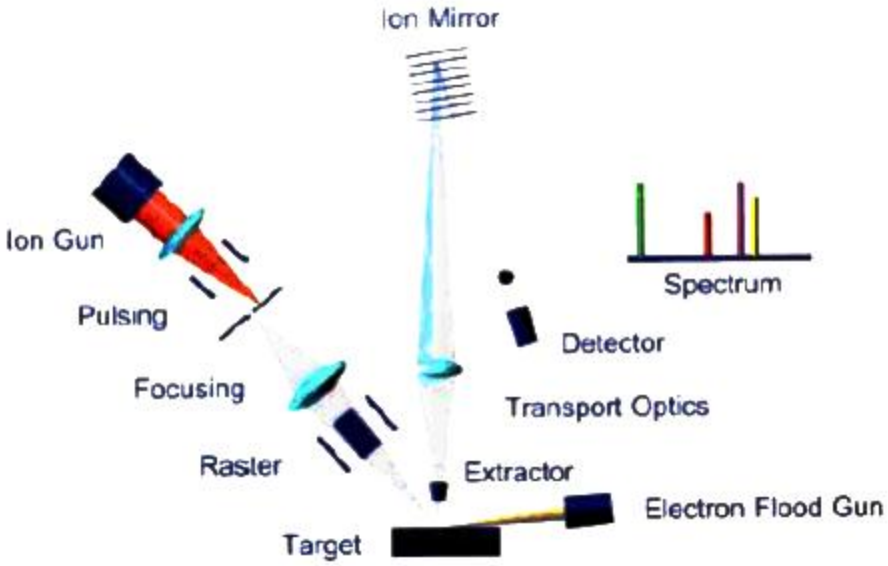

Figure 3.8: Schematic diagram of TOF-SIMS [19].

3.2.8.1 Surface imaging

If the aim of the measurements is to obtain compositional information of the surface formed from the secondary ion spectrum with minimum possible damage to the surface, then the main problem is to ensure that sufficient signal is obtained at the desired spatial resolution whilst minimizing the ion flux incident on any part of the surface. This is most easily achieved by switching from the traditional instrument approach of using continous-flux ion guns and quadrupole mass spectrometer detectors, to using pulsed ion sources and time-of-flight mass spectrometers. These spectrometers are a much more efficient way of acquiring spectral data and also provide good resolution and sensitivity up to the very high masses. Using such instruments, images with spartial resolution of better than 50 nm are obtainable [20].

3.2.8.2 Depth profiling

The aim of depth profiling is to obtain information on the variation of composition with depth below the initial surface. This information is particularly useful for the analysis of layered structures such as those produced in the semiconductor industry. The depth profile of a sample can be obtained by recording the sequential SIMS spectra as the surface is gradually eroded away by the incident ion beam probe. A plot of the intensity of a given mass signal as a function of time is a direct reflection of the variation of its abundance or concentration with depth below

the surface. One of the main advantages that TOF-SIMS offers over other depth profiling techniques (e.g auger depth profiling) are its sensitivity to very low concentrations of elements. Again this is particularly important in the semiconductor industry where dopants are often present at very low concentrations [19,20].

3.3. Organic solar cell device fabrication

3.3.1 General processing techniques

3.3.1.1 Cleaning the ITO glass substrate

Pre-patterned ITO glass substrates of 2.3 mm in thickness were sonicated for 10 min in isopropyl alcohol and acetone consecutively for 10 min each, followed by drying at ~ 80 ^{o}C in an oven for 20 min. The substrates were then put under a UV ozone generator for 20 min. The ITO glass substrates allow four cells to be synthesized at once with two cell areas of 0.12 cm^2 and 0.2 cm^2. The back electrode is evaporated on top of the ITO pattern and the overlap between evaporated metal and the active materials defines a single cell.

3.3.1.2 Spin coating

Spin coating is a simple and precise method that uses centrifugal force to produce a uniform thin film ranging from 20 to 300 nm in thickness. The variables in spin coating process are solvent concentration, spin speed and spin time and varying solution concentration and speed, the film thickness can be easily controlled. For organic solar cells fabrication, organic semiconductors require 100 to 200 nm film thickness. Spin time is determined by drying the wet film. During spin coating, the volatile solvent is evaporated and typical spin time is 30 seconds to 1 minute.

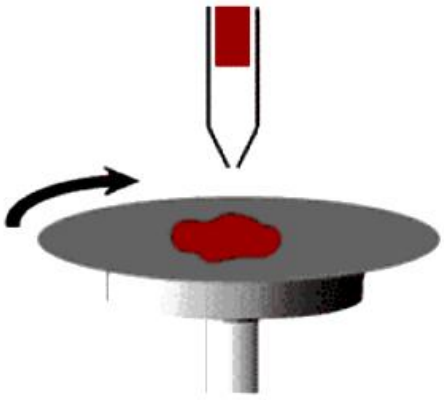

Figure 3.9: Scheme of spin coating process [21].

3.3.1.3 Thermal vacuum Evaporator

Thermal evaporation is a method to deposit thin films of metal or small molecule organic semiconductors. The variables to control the metal evaporation are vacuum chamber pressure, source material purity and evaporation power which is correlated with the evaporation rate. The pressure of the vacuum chamber should be maintained around 5 x 10^{-7} Torr to ensure good quality deposition. When the deposition is conducted at pressure higher than 1 x 10^{-6} Torr without reaching low enough pressure, hot evaporized metal particles reacts with remaining oxygen molecules and form metal oxides. Deposited layers with this condition lose metallic reflection and electrical properties. For high quality thin film, material purity over 99.99 % is essential. High purity sources material lowers the chance of side reactions or impurity formation during evaporation. The evaporation rate changes from 1Å/sec to 3Å/sec in most investigations and source materials should be evaporated slowly to protect the sub-layer which can be damaged by hot vapors. The schematic diagram of vacuum evaporator is shown in figure 3.10.

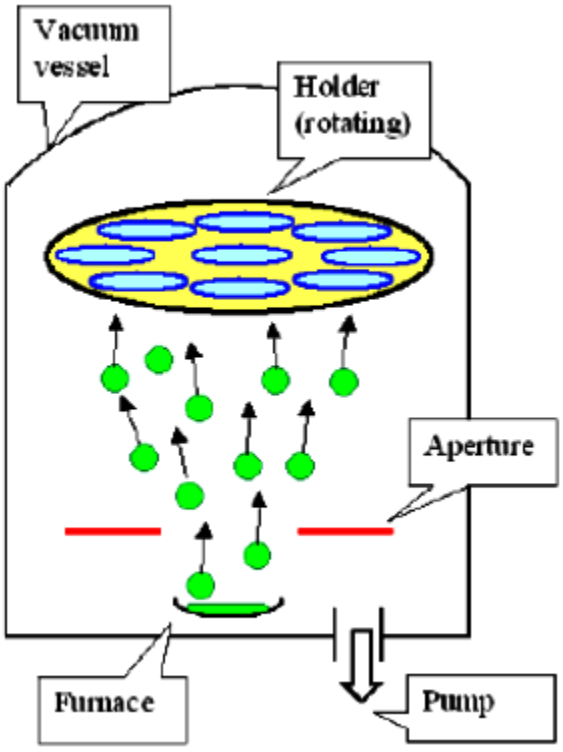

Figure 3.10: Diagram of vacuum evaporator [22].

For ***conventional device*** fabrication, roughly 1 mL of PEDOT:PSS is filtered through a 0.45 μm filter and the desired amount is spincoated on the ITO glass substrate using a micropipette. The PEDOT:PSS layer is dried in an oven at 110 ^{o}C for 10 min. After stirring for 3 hours, the P3HT:PCBM solution is filtered with a 0.45 μm filter. Using a micropipette, the desired amount of solution is spincoated on top of PEDOT:PSS layer. Then the ZnO buffer layer is also spincoated followed by thermal evaporation of ~ 100 nm Aluminum (Al) metal electrode. For ***inverted device***, the ZnO buffer layer is spin coated on top of ITO glass substrate and dried on hot plate at 60 ^{o}C for 1 hour. P3HT:PCBM solution is spincoated followed by PEDOT:PSS layer. The next step is to evaporate the ~ 100 nm silver (Ag) metal electrode. After cooling for ~ 30 min in the thermal evaporator the cells are annealed at 155 ^{o}C for 10min. An image of the complete conventional cell is shown in Figure 3.11.

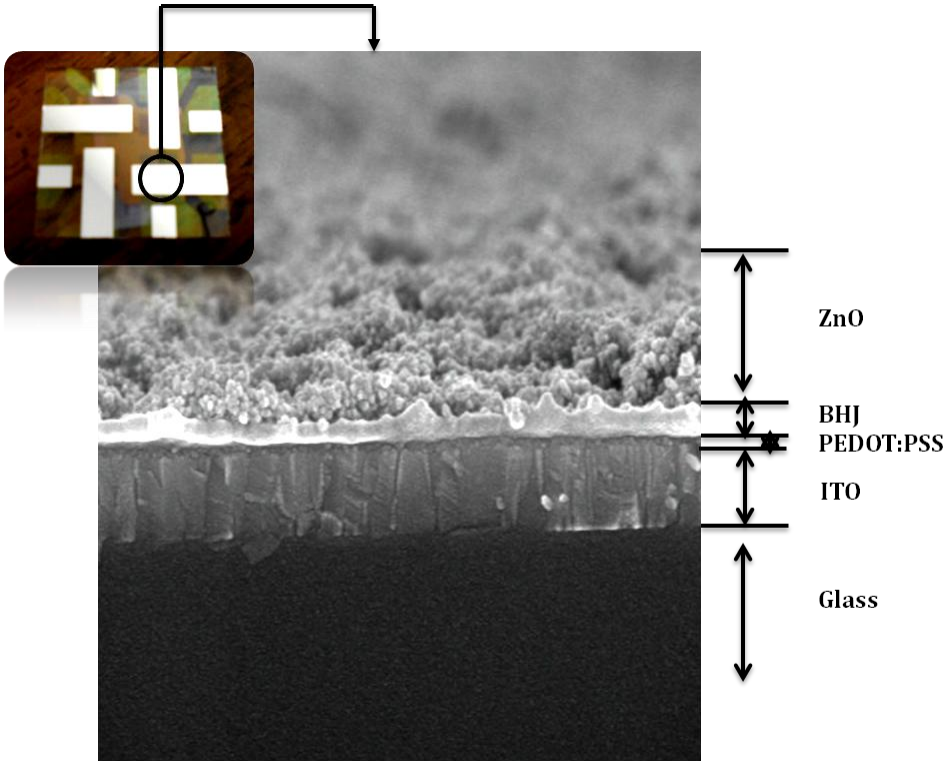

Figure 3.11: An image of a complete conventional organic solar cell and the FE-SEM cross-sectional view showing the device components layers.

References

[1] http://www.panalytical.com/index.cfm/pid=135 [Accessed June 2012]

[2] G.Gao, *Nanostructures and Nanomaterials: synthesis, properties and applications*. 6th edition, London, 2004

[3] K.S Rathore, D. Patidar, Y. Janu, N.S Saxena, K. Sharma and T.P Sharma, *Chalcogenide Letters* **5**(2008) 105-110

[4] J.R Connolly, for EPS400-002, *Introduction to X-ray Powder Diffraction*, Springer (2007)

[5] http://en.wikipedia.org/wiki/Transmission_electron_microscopy [Accessed June 2012]

[6] Z.L Wang, Y. Liu, Z.Zhang, *Handbook of nanophase and nanostructured materials*, 4th edition, New York, 2003

[7] http://www.gitam.edu/eresource/nano/NANOTECHNOLOGY/tem.htm [Accessed June 2012]

[8] University of Nebrasaka-Lncon:http//www.unl.edu/CMRAcfem/semoptic.htm. [Accessed June 2012]

[9]Binghamton University: Nanotechnology for undergraduate education: http//nue.clt.binghamton.edu/semtem.html [Accessed June 2012]

[10]J.Schweitzer, Radiological and Environmental Management (REM): http//www.purdue.edu/REM/rs/sem.htm 2008 [Accessed October 2009]

[11] N.Jalili and K. Laxminarayana, *Mechatronics* **14**(2004) 907-945

[12] R. Fung and S. Huang, *Journal of vibration and Acoustics* **123**(2001) 502-509

[13] A.V. Clemente and K. Gloystein, *Principles of Atomic Force Microscopy*, Physics of Advanced Materials winter school (2008) 1-10

[14]B.M Tissue, http://www.files.chem.vt.edu/chem-ed/spec/spectros.html (2000). [Accessed June 2012]

[15] http://en.wikipedia.org/wiki/Ultraviolet-visible_spectroscopy [Accessed June 2012]

[16] http://www.chemguide.co.uk/analysis/uvvisible/spectrometer.html [Accessed June 2012]

[17] http://www.keithley.com/products/dcac/voltagesource/broadpurpose/?mn=2400 [Accessed June 2012]

[18] Keithley model 2400 Series source meter, user's manual

[19]http://serc.carleton.edu/research_education/geochemsheets/techniques/ToFSIMS.html [Accessed Nov 2012]

[20] http://www.chem.qmul.ac.uk/surfaces/scc/scat7_4.htm [Accessed November 2012]

[21] http://www.clean.cise.columbia.edu/process/spintheory.pdf [Accessed November 2012]

[22] http://www.google.co.za/search?q=Diagram+of+vacuum+evaporator [Accessed November 2012]

4 ZnO Nanostructures: Background, Preparation and Characterization

In this chapter the properties and synthesis of nanosized zinc oxide (ZnO) particles are presented. Different nanostructures, such as spheres, flakes and flowers of ZnO were synthesized via a wet-chemistry route and were analyzed to be used as buffer layer/electron selective layer in organic solar cells (OSCs). The crystal structure, morphology and optical properties are also discussed.

4.1 Introduction

In recent years, there has been increasing interest in ZnO nanostructures due to their variety of morphologies and availability of simple and low cost processing [1]. In addition, nanostructured ZnO has distinguished performance in electronics, optics and photonics. Since the 1960s, synthesis of ZnO has been an active field and the study of low dimensional materials has become a leading edge in nanoscience and nanotechnology. With reduced particle size novel electrical, mechanical, chemical and optical properties have been observed which are the results of surface and quantum confinement effects [2].

While there are still unanswered questions concerning fundamental properties of ZnO, in particular those related to defects and visible luminescence lines, great progress has been made in synthesis methods and device applications of ZnO nanostructures. ZnO is a versatile functional material that has a diverse group of growth morphologies such as nanorods or nanowires for applications in transparent electrodes in solar cells, ultraviolet (UV) light emitters, diode lasers and spin-electronics [3,4]. Moreover, it has a direct wide bandgap (3.37 eV at room temperature) and high exciton binding energy (60 meV) making it the best candidate for applications particularly in solar cells [5]. ZnO nanostructures can be synthesized in a number of ways such as chemical bath deposition, laser ablation, hydrothermal process, co-precipitation and

sol-gel method [6-10]. However, most of these synthesis techniques involve processes of many complex steps requiring sophisticated equipments and extremely thorough experimental conditions. A wet-chemistry colloid preparation as opposed to other methods has its own attractiveness and ZnO nanostructures can be synthesized easily at low cost. A wet-chemistry route also allows the control of particle size, size distribution, shape and structures under different experimental conditions [11]. In this chapter the crystal and surface structure of ZnO, typical growth mechanisms and wet-chemistry synthesis methods of ZnO nanostructures for applications in organic solar cells are discussed. Furthermore, the kinetics in nanostructure formation such as change in morphology by monitoring the reaction time, temperature, pH and evaporation rate of ammonia in a solution are presented.

4.2. Crystal and surface structure of ZnO

ZnO crystallite is in a stable hexagonal wurtzite structure at room temperature and normal atmospheric pressure with lattice parameters a = 0.3296, c = 052065 nm and a density of 5.60 gcm^{-3}. The electronegativity values of O^{2-} and Zn^{2+} are 3.44 and 1.65, respectively, resulting in a very strong ionic bonding between Zn^{2+} and O^{2-}. The ZnO wurtzite structure is shown in Figure 4.1. Each zinc ion is surrounded tetrahedrally by oxygen ions, stacked alternatively along the c-axis. It is clear that this kind of tetrahedral arrangement of O^{2-} and Zn^{2+} in ZnO will form a non-central symmetric structure composed of two interpenetrating hexagonally closed packed sub-lattices of zinc and oxygen that are displaced with respect to each other along the hexagonal axis. This is responsible for the piezoelectricity observed in ZnO and it also plays an important role in crystal growth and defect generation [12].

Other basic characteristics of ZnO are the polar surfaces that are formed by oppositely charged ions, i.e. positively charged Zn^{+} and negatively charged O^{-} thus being responsible for the spontaneous polarization observed in ZnO. The polar surfaces of ZnO have non-transferable and non-flowable ionic charges. The interaction among the polar charges at the surface depends on their distribution; therefore the structure is arranged in such a way to minimize the electrostatic energy which is the main driving force for growing polar surfaces dominated nanostructures. This effect results in a growth of various ZnO nanostructures such as nanorods, nanowires, nanobelts and nanorings [13].

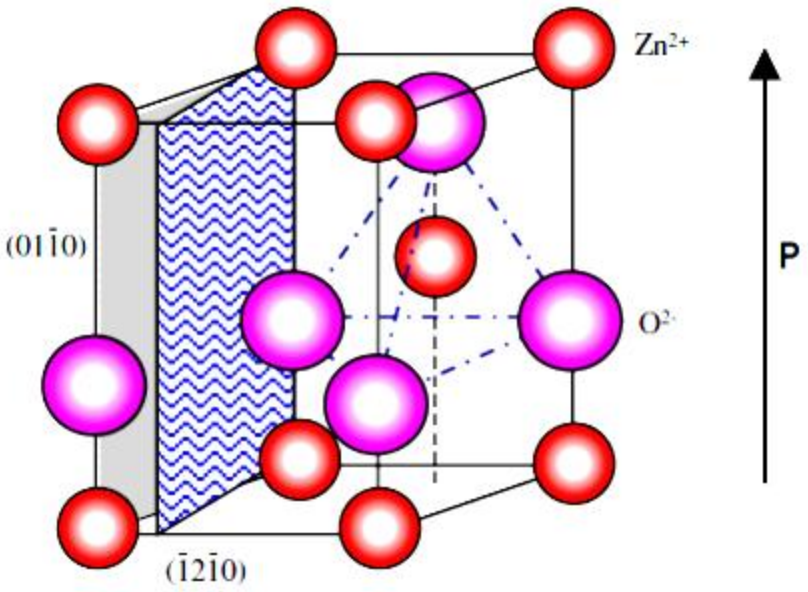

Figure 4.1: The wurtzite structure model of ZnO. The tetrahedral coordination of Zn-O is shown

4.3. Basic physical properties of ZnO

Understanding the fundamental physical properties of ZnO nanostructures is crucial to the rational design of functional devices and for developing their potential as the building blocks for future nanoscale devices [14]. The lattice parameters of wurtzite ZnO are shown in Table 4.1.

Table 4.1: Basic physical properties of wurtzite ZnO at room temperature [13,14]

Lattice parameters at 300 K	
a_0	0.32495 nm
c_0	0.52069 nm
a_0/c_0	1.6020(ideal hexagonal structure shows 1.633)
Density	6.505 g/cm^3
Stable phase at 300 K	Wurtzite
Melting point	1975 ^oC
Thermal conductivity	20.6, 0.13 1-1.2
Linear expansion coefficient (/^oC)	a_0: 6.5 x10^{-6}, c $_0$: 3.0 x10^{-6}

Static dielectric constant	8.656
Refractive index	2.008, 2.029
Energy gap	3.4 eV, direct
Intrinsic carrier concentration	$< 10^6$ cm^{-3} (max n-type doping $> 10^{20}$ cm^{-3} electrons, max p-type doping $< 10^{17}$ cm^{-3}
Exciton binding energy	60 meV
Electron effective mass	0.24
Electron Hall mobility at 300 K for low n-type conductivity	200 cm^2/Vs
Hole effective mass	0.59
Hole Hall mobility at 300 K for low p-type conductivity	5-50 cm^2/Vs
Bulk Young's modulus E (GPa)	111.2 ± 4.7
Bulk hardness, H (GPa)	5.0 ± 0.1

The lattice parameters of a semiconductor usually depend on the factors such as free electron concentration acting via deformation potential of a conduction band minimum occupied by these electrons, concentration of foreign atoms, defects and their difference of ionic radii [14]. The lattice parameters of any crystalline material are commonly and most accurately measured by X-ray diffraction.

4.4. Synthesis of ZnO Nanostructures

ZnO nanostructures can be synthesized by a variety of methods. Due to its rich defect chemistry, a large variety of electronic and optical properties can be obtained for different ZnO nanostructures [15]. While the relationship between the growth conditions, native defects concentrations and measured properties is not entirely clear, there are very few controversial topics when it comes to the growth of ZnO nanostructures. In this section ZnO nanostructures synthesized by precipitation and chemical bath method are discussed. Spherical nanoparticles,

nanoflakes and nanoflowers structures are also discussed for the applications in organic solar cells as electron selective layers.

4.4.1 ZnO nanoparticles synthesis

ZnO nanoparticles were synthesized by hydroxylation of zinc acetate dihydrate ($ZnAc.2H_2O$) by tetramethylammonium hydroxide (TMAH). In a typical preparation, TMAH dissolved in 30 ml of ethanol was added dropwise to 0.1M zinc acetate dihydrate dissolved in 30 ml of dimethylsulfoxide (DMSO) followed by vigorous stirring for 1hour at room temperature. Nanoparticles were precipitated by adding ethyl acetate. The precipitate was separated by centrifugation and was washed at least three times by a mixture of heptane and ethanol in the volume ratio of 2:1 and then in heptane only. The ZnO nanoparticles were either dispersed in ethanol/methanol or dried in an oven kept at 110^oC for 1hour. Figure 4.2 shows the schematic diagram of the synthesis.

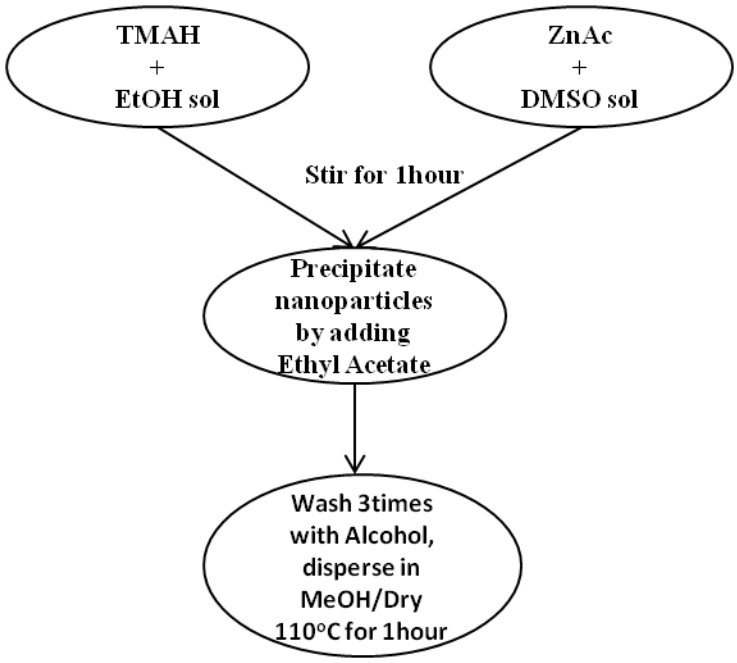

Figure 4.2: Schematic diagram of ZnO nanoparticles synthesis

4.4.2 ZnO nanoflake and nanoflower synthesis

ZnO nanoflakes were synthesized by adding a mixture of polyethyleneglycol (PEG) (M_w=1000) and ammonia water ($NH_3.H_2O$) dropwise to 0.2M solution of zinc nitrate hexahydrate ($Zn(NO_3)_2.6H_2O$) resulting in a white mixture with pH of 12. The mixture was rapidly stirred at

60^{o}C for 1 hour. The precipitate was centrifuged and washed at least three times with ethanol and distilled water and was then dried in an oven at 110^{o}C for 1hour. Similar experimental procedure was followed to prepare ZnO nanoflowers structures except that the mixture was vigorously stirred for 10 hours. Figure 4.3 shows the schematic diagram of the synthesis.

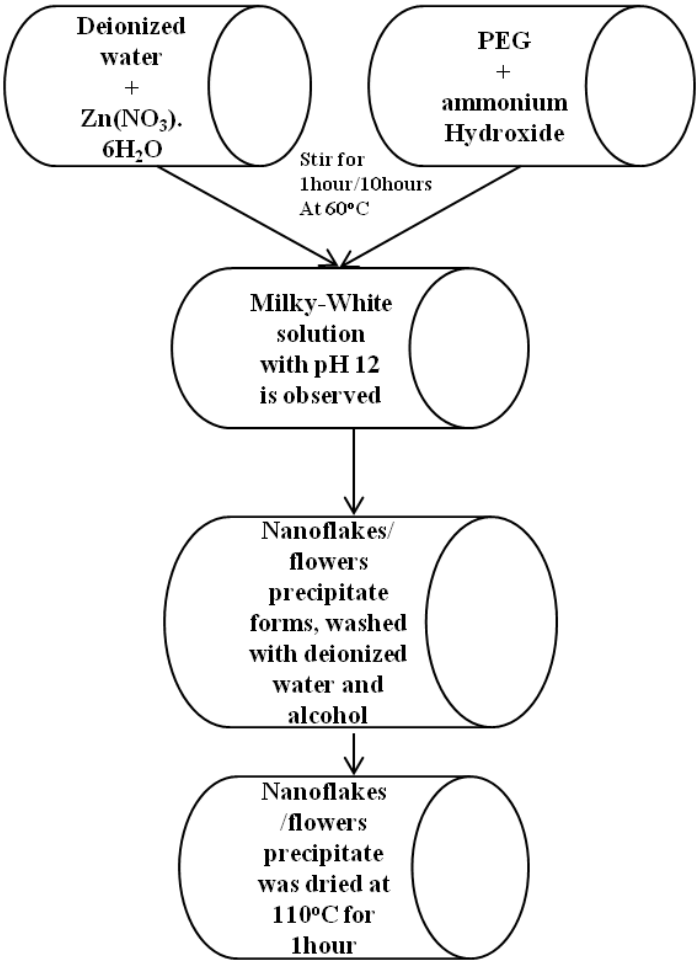

Figure 4.3: Schematic diagram of ZnO nanoflakes/nanoflowers synthesis.

4.4.3 Chemical bath method synthesis of ZnO

The solution of zinc acetate, ammonia and sodium hydroxide was used to synthesize ZnO nanoflower structures. 0.3 M of zinc acetate, 0.5 M ammonia and 0.1 M of sodium hydroxide solutions were mixed in a test tube with a continuous stirring. The volume ratios of the solutions were 50:50:50. The hot water bath was kept at temperature of 80 ^{o}C and the mixture was stirred for 10 minutes. The precipitate was centrifuged and washed several times with ethanol and heptane and was dried in an oven maintained at 110 ^{o}C for 1 hour. Figure 4.4 shows the schematic diagram.

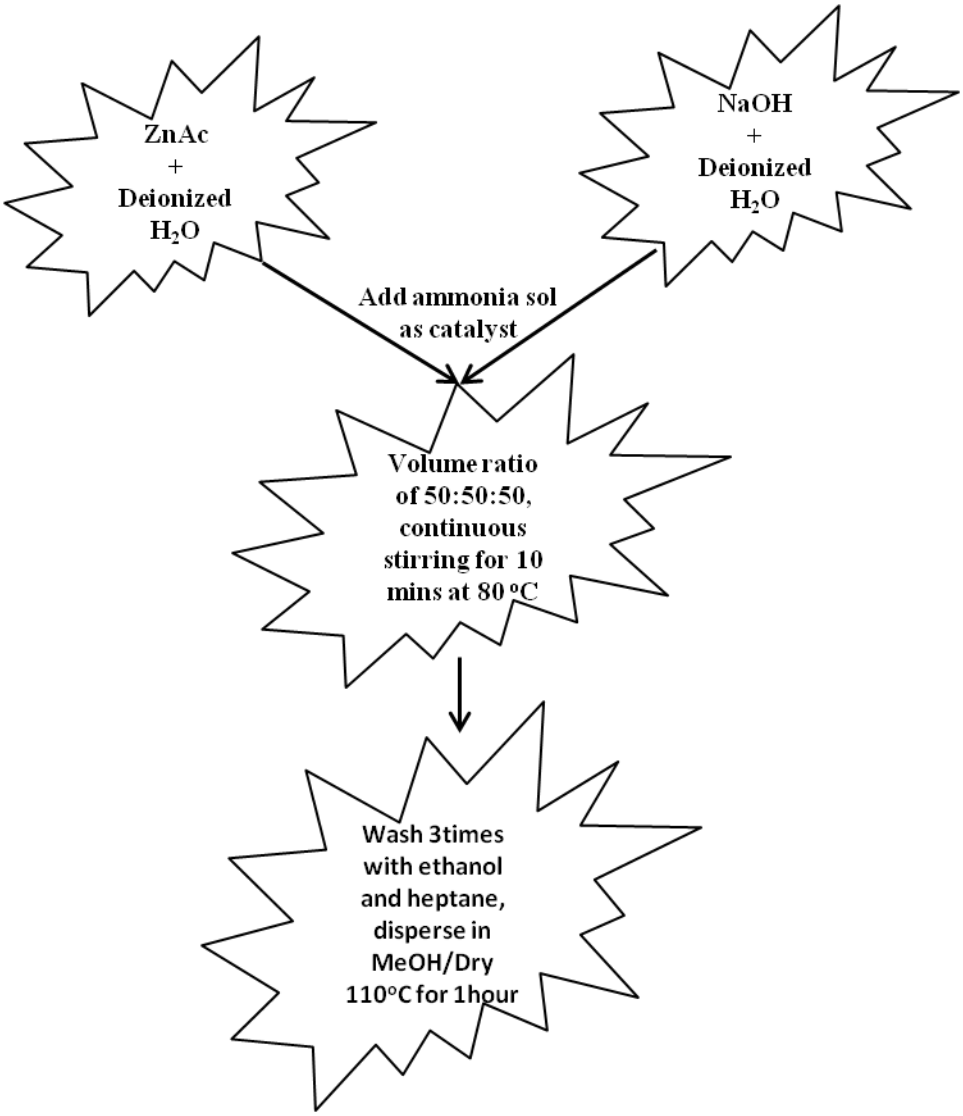

Figure 4.4: Schematic diagram of ZnO nanoflakes/flowers synthesis

4.4.4 Characterization of ZnO nanostructures

The structure of nanoparticulate ZnO, particle morphology, surface topography and optical absorption were studied using X-ray diffraction (XRD), field-emission scanning electron microscopy (FE-SEM), transmission electron microscopy (TEM) and UV-Vis spectrometry, respectively. These characterization techniques are discussed in details in Chapter 3, sections 3.2.1, 3.2.2, 3.2.3 and 3.2.5., respectively.

4.5. Crystal structure, morphology and kinetics in nanostructure formation

XRD patterns of ZnO nanostructures are shown in Figure 4.5. The diffraction peaks at scattering angles (2θ) of 31.8 ^{o}, 34.4 ^{o}, 36.3 ^{o}, 47.5 ^{o}, 56.5 ^{o}, 62.7 ^{o}, 66.3 ^{o}, 67.9 ^{o} and 69.0^{o} correspond to the reflection from (100), (002), (101), (102), (110), (103), (200), (112) and (210) crystal planes, respectively, matching well with the standard JCPDS data, card number 80-0075. Furthermore, XRD indicates that ZnO nanostructures exhibit the hexagonal wurtzite structure. Impurity peaks were observed from diffraction patterns of nanoflakes and this could be due to the precursor concentration super-saturation or short reaction times. The impurity peaks are due to the hydroxide chains which matched the standard JCPDS data, card number 76-1778 of $Zn(OH)_2$. The Debye-Scherrer equation [16,17] which uses the width of the peak at half of its maximum height (FWHM) of the wide angle x-ray scattering was used to estimate the crystallite size.

$$D = \frac{0.9\lambda}{\beta Cos\theta} \tag{4.1}$$

where λ is the wavelength of X-ray source, β is the full-width at half maximum in radians and θ is the Bragg's diffraction angle. The crystallite sizes of nanoparticles and nanoflakes were found to be ~ 5 ± 0.2 nm and ~20 ±0.2 nm, respectively and that of nanoflowers ~35 ± 0.2 nm. Figure 4.6(a-e) shows the FE-SEM images of ZnO nanoparticles, nanoflakes and nanoflowers. Spherical nanoparticles and randomly oriented nanoflakes were observed (Figure 4.6 (a-b)). Flower-like clusters were also observed (fig 4.6(c-e)), they have symmetric arms in level directions. Every arm consists of cluster of nanoparticles. TEM images in Figure 4.7(a-b), indicates agglomeration of nanoparticles with the diameter of about 5 nm in accordance with the XRD results and rods growing into flower-like structures (Figure 4.7(c-d)). The insert in Figure 4.7 (b) and (d) are the selected area electron diffraction patterns which consist of grainy rings due to the crystallinity of ZnO.

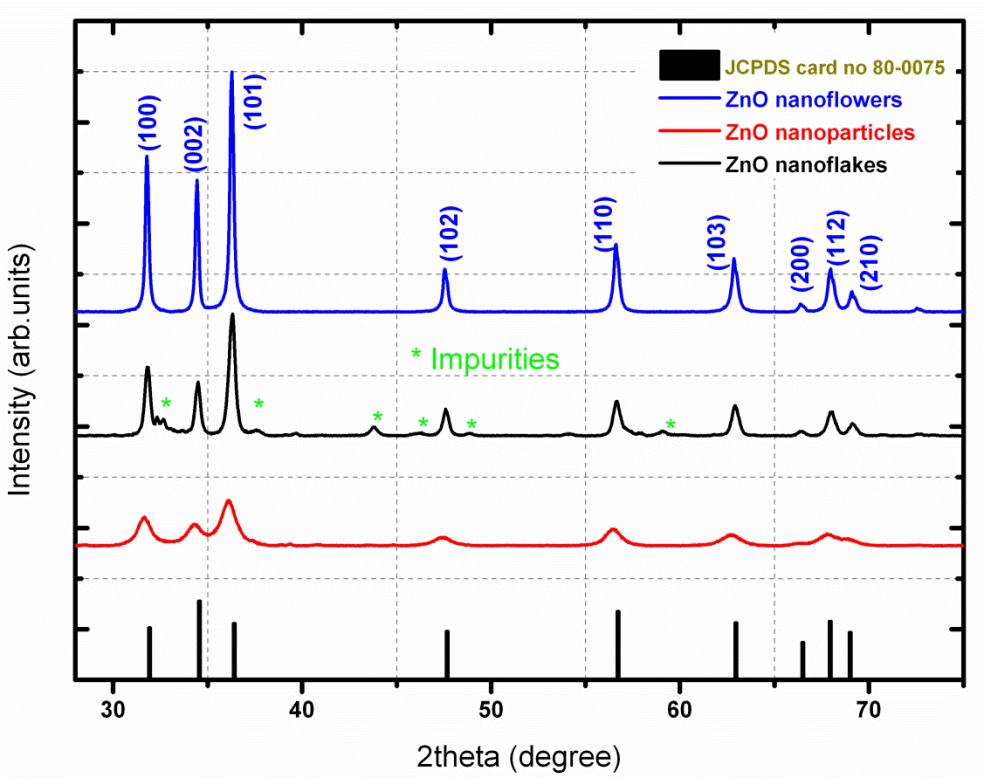

Figure 4.5: XRD spectra of ZnO nanostructures

ZnO nanostructures are expected to crystallize by the hydrolysis of Zn salts in basic solution that can be formed using strong or weak alkalis. Zn^{2+} is known to coordinate in tetrahedral complexes. Due to the $3d^{10}$ electron configuration, it is colorless and has zero crystal field stabilization energy. Zn^{2+} is able to exist in a series of intermediates and ZnO can be formed by the dehydration of these intermediates. Chemical reactions in aqueous systems are usually considered to be in a reversible equilibrium and driving force is the minimization of the free energy of the entire reaction system, which is the intrinsic nature of wet chemical methods [18]. The main reactions involved in the growth of ZnO nanostructures are illustrated in the following equations [19,20]:

$$Zn^{2+} + 2OH^- \leftrightarrow Zn(OH)_2 \quad (4.2)$$

$$Zn(OH)_2 + 2OH^- \leftrightarrow [Zn(OH)_4]^{2-} \quad (4.3)$$

$$[Zn(OH)_4]^{2-} \leftrightarrow ZnO_2^{2-} + 2H_2O \quad (4.4)$$

$$ZnO_2^{2-} + H_2O \leftrightarrow ZnO + 2OH^- \quad (4.5)$$

$$ZnO + OH^- \leftrightarrow ZnOOH^- \quad (4.6)$$

In the condition where ammonia is used, the mechanism of the formation of ZnO is usually accepted as follows:

$$NH_3 + H_2O \leftrightarrow NH_3.H_2O \leftrightarrow NH_4^+ + OH^- \quad (4.7)$$

$$Zn^{2+} + 4NH_3 \rightarrow Zn(NH_3)_4^{2+} \quad (4.8)$$

$$Zn(NH_3)_4^{2+} + 2OH^- \rightarrow ZnO + 4NH_3 + H_2O \quad (4.9)$$

$$Zn^{2+} + 4OH^- \rightarrow Zn(OH)_4^{2-} \quad (4.10)$$

$$Zn(OH)_4^{2-} \rightarrow ZnO + H_2O + 2OH^- \quad (4.11)$$

It can be seen that ZnO nuclei are obtained by the dehydration of $Zn(OH)_4^{2-}$ or $Zn(NH_3)_4^{2+}$. In the presence of PEG, growth units $Zn(NH_3)_4^{2+}$ or $Zn(OH)_4^{2-}$ are easily adsorbed by the atom O in the C-O-C chain. $Zn(OH)_4^{2-}$ or $Zn(NH_3)_4^{2+}$ can be carried and transformed into ZnO crystalline nanoparticles/nanoflakes and grow on active sites around the surface of ZnO nuclei. When the reaction temperature is low (60 ^oC), the rate of production of NH_3 is slow and more Zn^{2+} are transformed in to ZnO nuclei in the function of hydroxyl. Thus more ZnO nuclei with active sites aggregate spontaneously in hexagonal symmetry direction, which provides more chances for the formation of flower-like ZnO. When the synthesis temperature rises to 80 ^oC, more productions of NH_3 make $Zn(NH_3)_4^{2+}$ increase in the reaction system, which decreases the rate of formation of ZnO nuclei compared with that at 60 ^oC. When the rate of growth matches the rate of formation of nuclei, single/bundled nanorods structure is formed. In the case of 80 ^oC, the quantity of activity sites increases with the rise in temperature, which gives an advantage for more rods growing around ZnO nuclei [21,22].

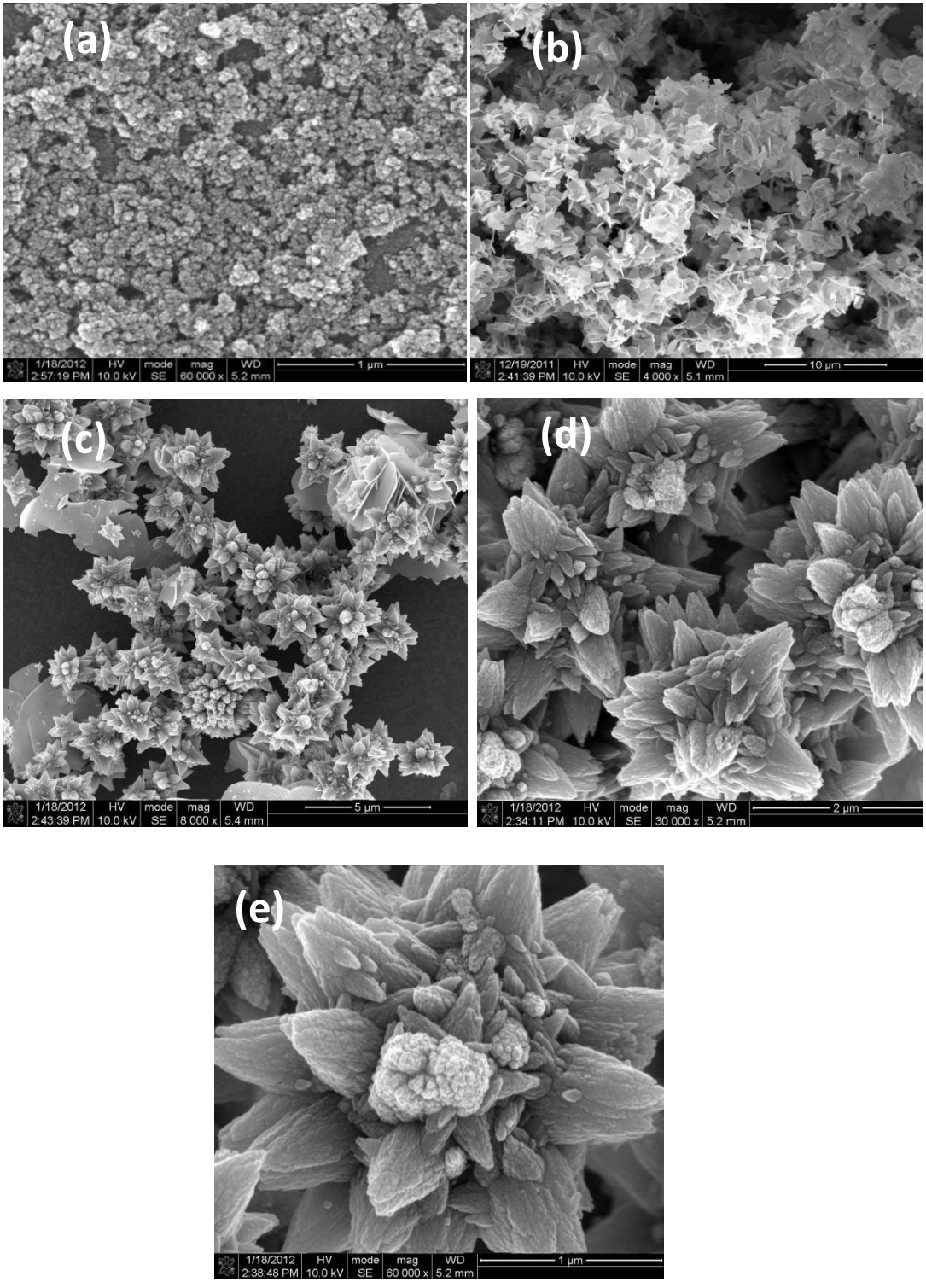

Figure 4.6: FE-SEM images of (a) ZnO nanoparticles, (b) Nanoflakes, (c-e) Flower-like clusters

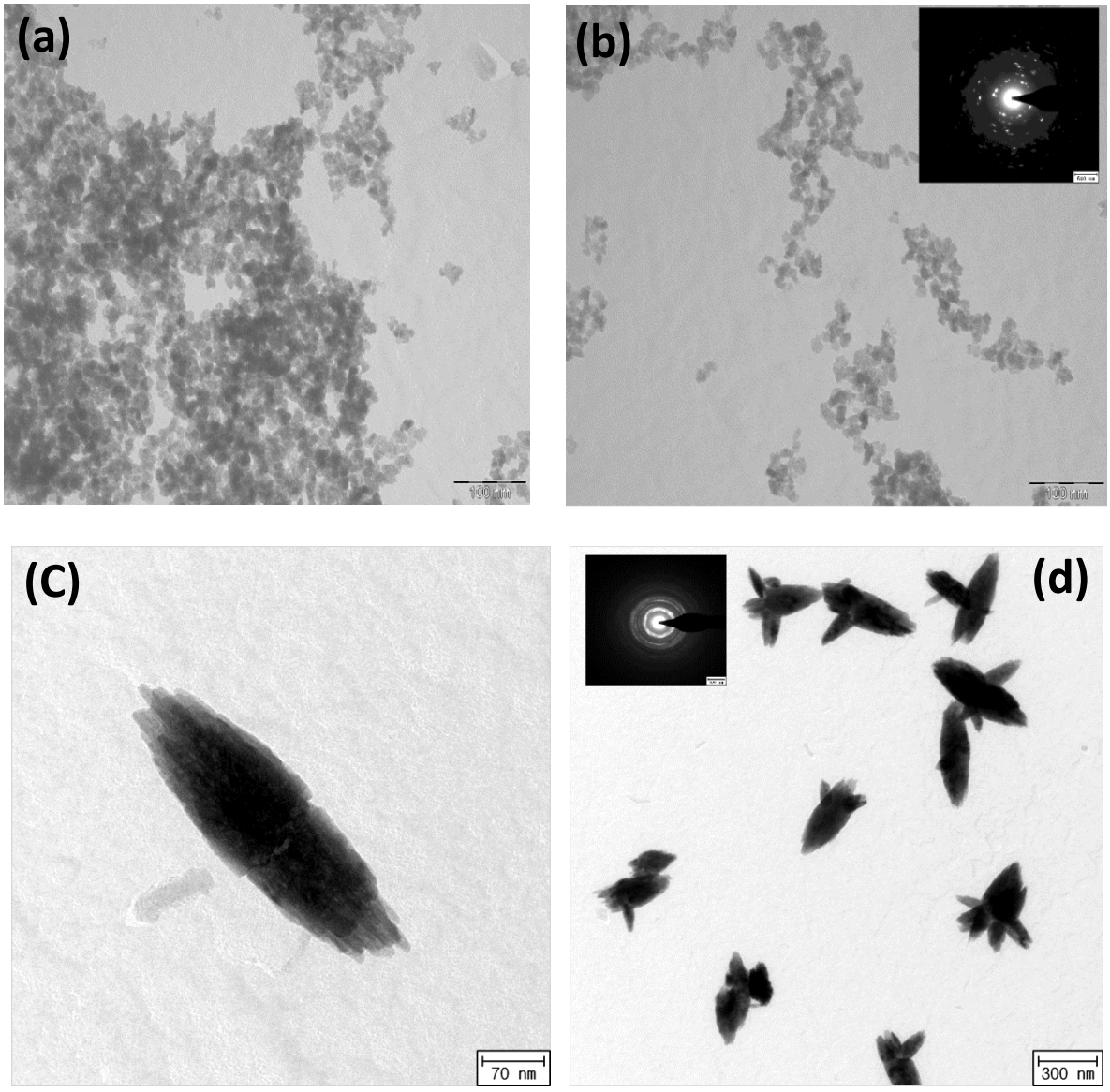

Figure 4.7: TEM images of (a-b) ZnO nanoparticles and (c-d) From nanorod to flower-like formation.

4.6. Optical absorption properties

UV-visible absorption spectra of ZnO nanostructures are shown in Figure 4.8. The ZnO nanoparticles exhibit two absorption peaks at ~251 and ~348 nm. The major absorption peak at 348 nm represents a well known intrinsic band gap absorption of ZnO, and it is attributed to electronic transitions from the valence band to the conduction band while the minor absorption peak at 251 nm is attributed to impurities or structural defects associated with either Zn or O vacancies [23,24]. In the case of the ZnO nanoflakes, intrinsic excitonic absorption peak at ~ 348 nm was not observed and only the ~251 nm was observed. The absence of absorption peak at 348 nm could be due to unbound electron and holes which show broad and flat optical absorption spectrum [25]. Kim et al [26] observed the broadening and flattening of excitonic absorption band from ZnO nanorods at ~ 375-400 nm and they attributed this to variation (heterogeneity) in particle sizes. Furthermore, Chandrappa et al. [27] attributed lack of excitonic absorption in ZnO nanoparticles to incomplete formation of ZnO (i.e. incomplete decomposition of precursors). The optical absorption of a direct band gap semiconductor can be calculated using Tauc's relation given by the equation 4.12 [28]:

$$\alpha h\upsilon = A(h\upsilon - E_g)^{1/2} \quad (4.12)$$

where A is the proportionality constant, α is the absorption coefficient and $h\upsilon$ is the photon energy (h = Planck's constant and υ = frequency of the photon). By plotting $\alpha h\upsilon^2$ against $h\upsilon$, $E_g$can be estimated by extrapolating the linear portion of the curve to zero absorption [28]. The estimated optical band gap was ~ 3.34 eV for ZnO nanoparticles as shown in Figure 4.9. The band gap of nanoflakes and nanoflowers using equation 4.12 could not be estimated because the excitonic absorption band was completely flattened.

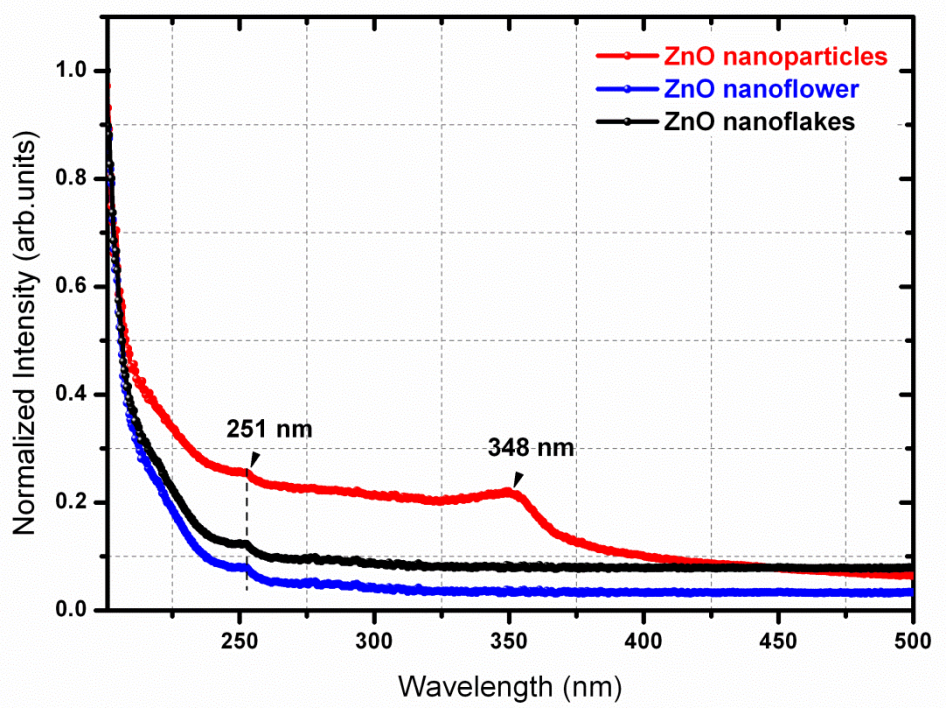

Figure 4.8: UV-Vis absorption spectra of ZnO nanostructures.

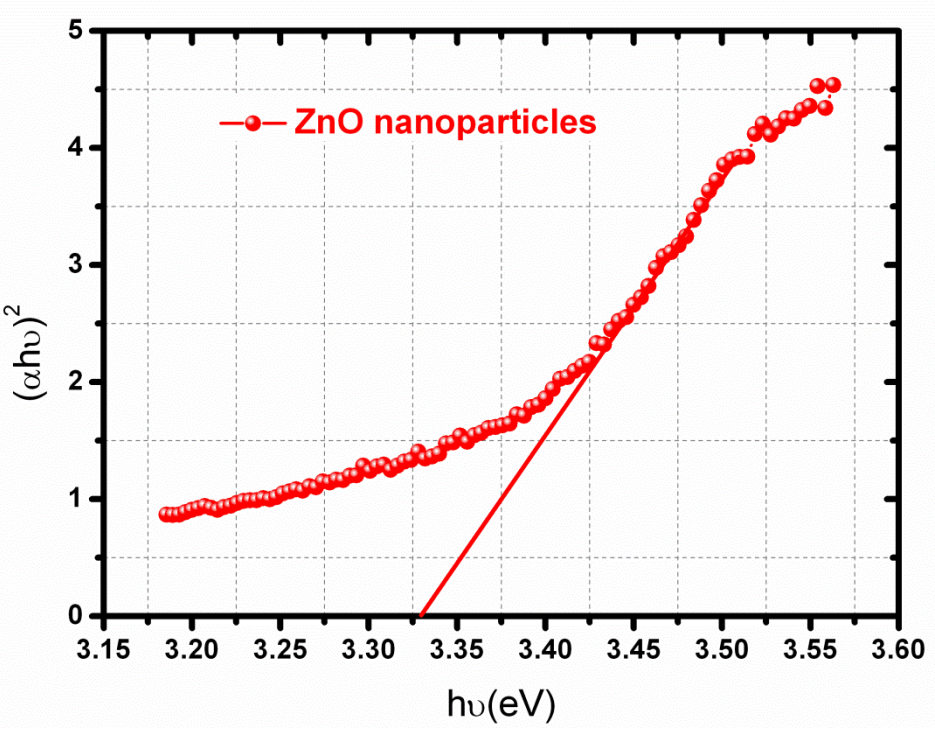

Figure 4.9: Plot of $(\alpha h\upsilon)^2$ vs photon energy ($h\upsilon$) of ZnO nanoparticles

The particle sizes of the ZnO nanoparticles were estimated using the following relationship between the band gap and particle radius, *r* [29]:

$$E = E_g + \frac{\pi^2 \hbar}{2m_0 r^2}\left(\frac{1}{m_e^*} + \frac{1}{m_h^*}\right) - \frac{1.8e^2}{4\pi\varepsilon_0\varepsilon_r r} - 0.25\frac{e^4}{8\pi^2\varepsilon_0^2\varepsilon_r^2 \hbar}\left(\frac{1}{m_e^*} + \frac{1}{m_h^*}\right)^{-1} \quad (4.13)$$

where *E* is the band gap of ZnO nanostructures, E_g is the band gap of the bulk ZnO (3.20 eV at room temperature) [24], m_e^* and m_h^* are the effective masses of the electron and holes, *r* is the radius of the particle, ε_0 is the permittivity of the vacuum, ε_r is the relative permittivity of the particle, *e* is the elementary charge and $\hbar$ is Planck's constant. Using $m_e^* = 0.26m_e$ and $m_h^* = 0.59m_h$ for ZnO [24] the particle radius was found to be ~ 2.21 nm with the average particle size estimated to be 4.42 ± 0.5 nm in diameter. This is in agreement with the crystallite size of ZnO nanoparticles estimated from the X-ray diffraction data.

4.7. Conclusion

ZnO nanostructures for applications in organic solar cells were successfully synthesized via a wet-chemistry route. XRD analysis revealed the impurities/secondary phases of the synthesized ZnO nanoflakes due to the incomplete reaction of precursors; however prolonging the reaction time no impurities/secondary phases were observed for ZnO nanoflowers. Reaction mechanisms involved in the growth of ZnO nanostructures were discussed and by manipulation of parameters such as pH, reaction time, temperature and precursor concentration, growth and nucleation process can be controlled and particle morphology can be tailored. Optical absorption showed both excitonic band gap absorption (~ 348 nm) and defects related absorption (~ 251 nm) for nanoparticles. Large band gap of ZnO nanoparticle was obtained by using Tauc's relation and the relationship between band gap and particle radius was used to estimate the particles size of ZnO nanoparticles.

References

[1] A.B Djurisic, A.M.C Ng and X.Y Chen, *Progress in Quantum Electronics* **34**(2010) 191-259

[2] A.B.Djurisic, X. Chen, Y.H Leung and A.M.C Ng, *Journal of Materials Chemistry* **22**(2012) 6526-6535

[3] U. Ozgur, Y. I. Alivov, C. Liv, A. Teke, M.A Reshchikov, S.Dogan, V. Avrutin, S.-J. Cho and H. Morkocd, *Journal of Applied Physics* **98** (2005) 041301-1-041301-103

[4] A.K Singh, V. Viswanath and V.C Janu, *Journal of Luminescence* **129** (2009) 874-878

[5] Kuo-Feng Lin, Hsin-Ming Cheng, Hsu-Cheng Hsu, Li-Jiaun Lin and Wen-Feng Hsieh, *Chemical Physics Letters* **409**(2005) 208-211

[6] H, Zhang, J. Feng, J. Wang and M. Zhang, *Material Letters* **61** (2007) 5202-5205

[7] X. Hou, L. Wang, B. Yu, F.Zhoo and W. Liu, *Particuology* **8** (2010) 458-462

[8] Y.W Chen, Q. Qias, Y.C Liu, and G.L Yang, *Journal of Physical Chemistry* **113** (2009) 7494-7502

[9] Y.J Kwon, K.H Kim, C.S Lim and K.B Shim, *Journal of Ceramic Processing Research* **3** (2002) 146-149

[10] Y. Lare, A.Codoy, L. Cattin, K. Jondo, T. Abachi, F.R. Diaz, M. Morsli, K. Napo, M.A. del Valle and J.C Bernede, *Applied Surface Science* **255**(2009) 6615-6619

[11] C. Wu, X. Qiao, J. Chen, H. Wang, F.Tan and S.Li, *Materials Letters* **60**(2006) 1828-1832

[12] Zhang Lin Wang, *Journal of Physics: Condensed Matter* **16**(2004) 829-858

[13] C. Jagadish and S.J Pearton, *Zinc Oxide Bulk, Thin Films and Nanostructures 1st edition*,(2006), Elseviser Ltd. Oxford, UK

[14] H.Morkoc and U. Ozgur, *Zinc Oxide: Fundamentals, Materials and Device Technology*,(2009) Wiley-VCH Verlag GmbH & Co. KGaA, Weinheim, Germany

[15] A.B. Djurisic, X. Chen, Y.H Leung and A.M. C Ng, *Journal of Materials Chemistry* **22** (2012) 6526-6535

[16] H. Oh, J. Krantz, I. Litzov, T. Stubhan, L. Pinna and C.J Brabec, *Solar Energy Materials and Solar Cells* **95**(2011) 2194-2199

[17] S.Tachikawa, A. Noguchi, T. Tsuge, M. Hara, O. Odawara and H. Wada, *Materials* **4**(2011) 1132-1143

[18] S. Xu, Y. Shen, Y. Ding and Z.L Wang, *Advanced Functional Materials* **20**(2010) 1493-1495

[19] L.N Demianets and D.V Kostomarov, *Annales de Chimie Sciences* **26**(2001) 193-198

[20] L.N Dem'yanets, D.V Kostomarow and I.P Kuz-mina, *Journal of Inorganic Materials* **38**(2002) 124-131

[21] S.Xu and Z.L Wang, *Nano Research* (2011) DOI 10.1007/s12274-011-0160-7

[22] Y.Zeng, T. Zhang, L. Wang, R. Wang, W. Fu and H. Yang, *Journal of Physical Chemistry* **113**(2009) 3442-3448

[23] D. Bera, L. Qian, S. Sabui, S. Santra and P.H Holloway, *Optical Materials* **30** (2008) 1233-1239

[24] P. Kumbhakar, D. Singh, C.S Tiwary and A.K Mitra, *Chalcogenide Letters* **5**(2008) 387-394

[25] K.Ogawa, proceedings of the XXVIIth General Assembly of the International Union of Radio Science, Maastricht The Netherlands, 17-24 August 2002 pp. 1495-1498

[26] S.Y Kim, I.S Lee, Y.S Yeon, S.M Park and J.K Song, *Bulletin of the Korean Chemical Society* **29**(2008) 1960-1964

[27] K.G. Chandrappa, T.V. Venkatesha, K. Vathsala and C. Shivakumara, *Journal of Nanoparticle Research* **12**(2010) 2667-2678

[28] H.Oh, J. Krantz, I. Litzov, T. Stubhan, L. Pinna and C.J. Brabec, *Solar Energy Materials and Solar Cells* **95**(2011) 2194-2199

[29] Y. Diecmann, H. Colfen, H. Hofmann and A. Petri-Fink, *Analytical Chemistry* **81**(2009)3889-3895

5 Optimizing the performance of organic solar cells by varying processing parameters in the photo-active layer

In this chapter the effect of solvent and weight ratio on the photo-active (P3HT:PCBM) blend of organic solar cell (OSC) devices are investigated. Dissolving the photo-active materials in 1,2-dichlorobenzene (DCB) and chlorobenzene (CB) solvents, optical absorption of the blended films, external quantum efficiencies (EQE) and photovoltaic properties of devices were evaluated. The films prepared by using CB showed intense absorption compared to those prepared from DCB solvent. The current-density (J-V) characteristics showed a maximum power conversion efficiency of ~2.94 % from CB solution while the power conversion efficiency of ~2.86 % was obtained when DCB was used as solvent. In addition, different weight ratios of the photo-active materials (P3HT:PCBM) spin-coated from CB were varied (i.e. 1:0.6, 1:0.8, 1:1 and 1:1.2) and the results are discussed.

5.1. Introduction

Conventional bulk heterojunction (BHJ) organic solar cells (OSCs) are of great interest nowadays due to their potential applications as sources of renewable energy and for being able to reach power conversion efficiencies of 3-9 % [1,2]. Among all possible materials that have been used as photo-active layers, the most widely used material system in BHJ-OSCs is the blend of poly(3-hexylthiophene-2,5-diyl) polymer or P3HT and [6,6] phenyl butyric acid methyl ester fullerene or PCBM, and the layer is commonly referred to as P3HT:PCBM. Investigations show that OSCs made from this blend have power conversion efficiencies that can go up to 3-5% and this indicate the reasonable capability of the P3HT:PCBM blend to attain high efficiencies in future [3,4]. High performance can be achieved by the optimization of phase segregation in the polymer-fullerene blend and the development of new materials allowing better p-n interfaces and balanced charge transport [3]. In OSCs the efficient photo-induced charge separation strongly depends on the processing conditions used in depositing the photo active layer, morphology of the photo active layer, drying time, nature of solvent and thermal annealing [5]. Moreover,

maximum photovoltaic response is obtained by optimizing processing parameters in the P3HT:PCBM blend system and the thickness of the active layer is important in this regard [6]. Solvents such as cholorobenzene and 1,2-dichlorobenzene have been explored by many researchers as feasible to improve the film morphology thereby enhancing the conversion efficiencies in OSCs. Kim *et al* [7] found that active layers cast from chlorobenzene demonstrated more ordered mesophase morphology and ultimately performed more efficiently than those cast from dichlorobenzene.

5.2. Experimental

Device Fabrication: A glass substrate pre-coated with ITO was cleaned ultrasonically using isopropanol and acetone consecutively for 10 minutes. The substrates were dried at ~ 80^{o}C in an oven for 20 minutes and were then treated in an ultraviolet ozone generator for 20 minutes. A thin layer of poly(3,4-ethylenedioxythiophene):polystyrenesulfonic acid (PEDOT:PSS) (CLEVIOS™ AI 4083) was spin coated on a substrate at the speed of 4000 rpm for 35 seconds then followed by drying at 110^{o}C for 10 minutes. The photo active P3HT:PCBM blend layer (P3HT, Aldrich/ PCBM, Nano-C), with weight ratio of 1:0.6, dissolved from a blend solution of chlorobenzene and 1,2 dichlorobenzene was spin coated on the substrate at the speed of 1000 rpm for 15 seconds. This was followed by the deposition of the Al layer (~ 100 nm) thermally evaporated at ~ 1x10^{-6} Torr pressure through a shadow mask defining the device area of 0.12 cm^{2}. The devices were then heat treated at 155^{o}C for 10 minutes. The same device fabrication procedure was followed for different weight ratios of 1:0.6, 1:0.8, 1:1 and 1:1.2 using chlorobenzene solvent.

Films and Device Characterization: The UV-Vis absorption spectrum of the P3HT:PCBM blend films were recorded using Perkin – Elmer Lambda 35 UV-Vis spectrophotometer. The current density-voltage (J-V) curves were measured in air by a Keithley 2400 source meter and an Oriel Xenon lamp (150 W, Newport) coupled with an AM1.5 filter to simulate sunlight. The light intensity was calibrated using a silicon reference cell with a KG2 filter following standard solar cell testing procedures. The light intensity used in this study was 100mW/cm^{2}. The external quantum efficiencies (EQE) as a function of wavelength were measured using incident photo-to-current efficiency (IPCE) measurement system (PV measurement, Inc).

5.3. Results and discussion

Figure 5.1 shows the UV-Vis absorption spectrum of P3HT:PCBM films prepared from CB and DCB solvents. The absorption band at ~ 510 nm is attributed to the π-π* transition of P3HT while the shoulders at ~557 nm and ~609 nm are due to the inter-chain interactions. The two shoulders at ~557 nm and ~609 nm become prominent in the device made from the blend of CB solution as compared to that of DCB, indicating the highly crystalline nature of the P3HT in the blend [8,9]. Absorption due to P3HT at ~ 508 nm is also observed in figure 5.2. The absorption of the films in the visible region, specifically between 400-650 nm, significantly decreases with an increase of PCBM content in the blend. This can be attributed to the interactions between polymer chains and PCBM molecules where the presence of PCBM lowers the interaction among the P3HT chains upon increased disordering in the blend film. Moreover, the peak intensity at ~ 338 nm, which is due to PCBM [10], increases slightly with an increase of PCBM weight.

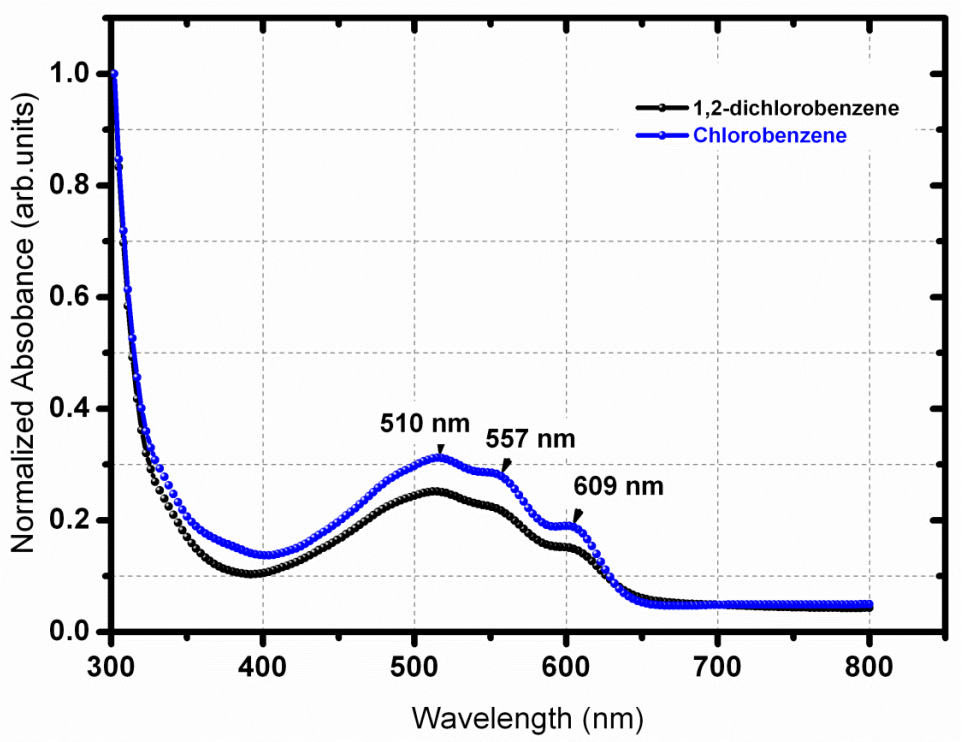

Figure 5.1: UV-visible spectra of P3HT:PCBM blend processed from chlorobenzene and 1,2-dichlorobenzene solutions

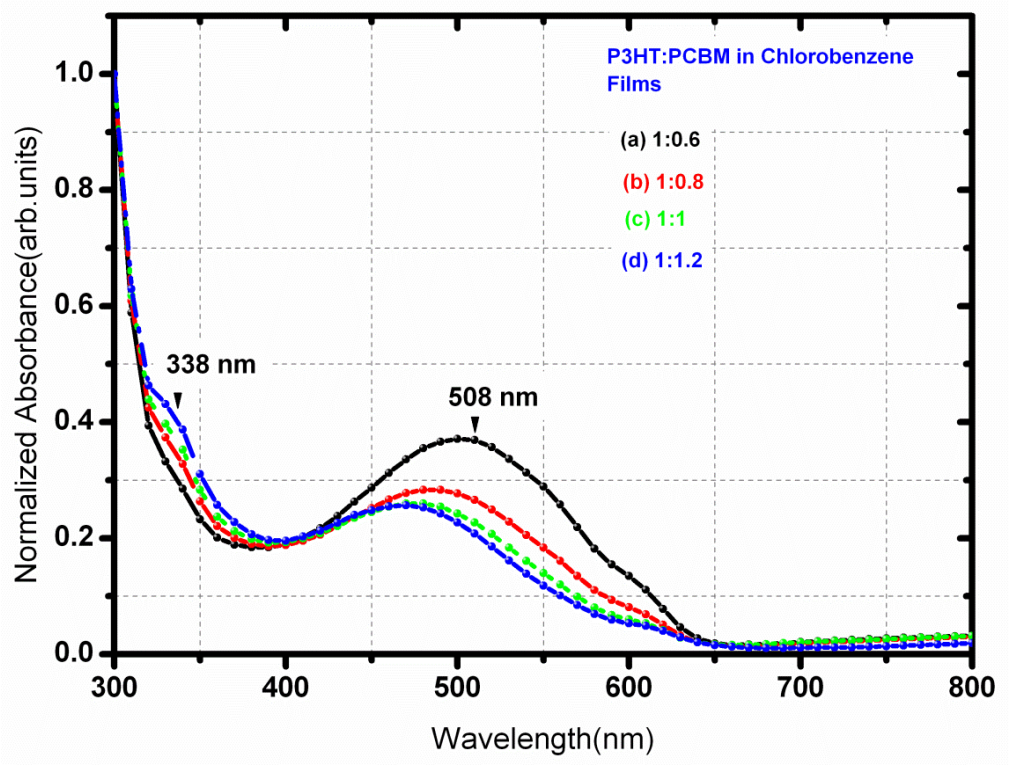

Figure 5.2: UV-visible spectra of P3HT:PCBM blend from chlorobenzene solution varying ratios of P3HT/PCBM

The measured current density-voltage (J-V) and external quantum efficiency (EQE) curves of P3HT:PCBM solar cells in dark and under illumination are shown in figure 5.3 (a) and (b). The corresponding photovoltaic characteristics are summarized in Table 5.1. The dark J-V curve indicates a diode behavior which shows that the devices have little or no shunts. The power conversion efficiency (PCE), short-circuit current (J_{sc}) and fill factor (FF) of OSCs processed from CB slightly increases compared to the DCB solvent and short circuit voltage (V_{oc}) of devices remain constant. This is attributed to higher carrier mobility, better conductivity of active layer film and charge collection to the respective electrodes in devices processed from CB [10]. Furthermore, the increase of J_{sc} is also attributed to a better packing of P3HT chains as well as structural re-organization of the blend film. Factors like solution viscosity, balancing of solvent evaporation rate and solubility of materials in these solvents also influence the general performance of OSCs [11]. As mentioned, the significant improvement in photocurrent was observed when the CB solvent was used. This could also be due to the different degree of material mixing which provides better P3HT/PCBM interface [12]. It is also possible that the

PCBM nanocrystals in CB processed film constitutes appropriate pathways for enhanced electron transport to the respective electrode compared to the DCB processed films. The EQE curves confirm better device performance from the CB solution with FF of 50.42 % and photons absorbed at ~383 nm, ~599 nm and maximum photons are absorbed at ~505 nm.

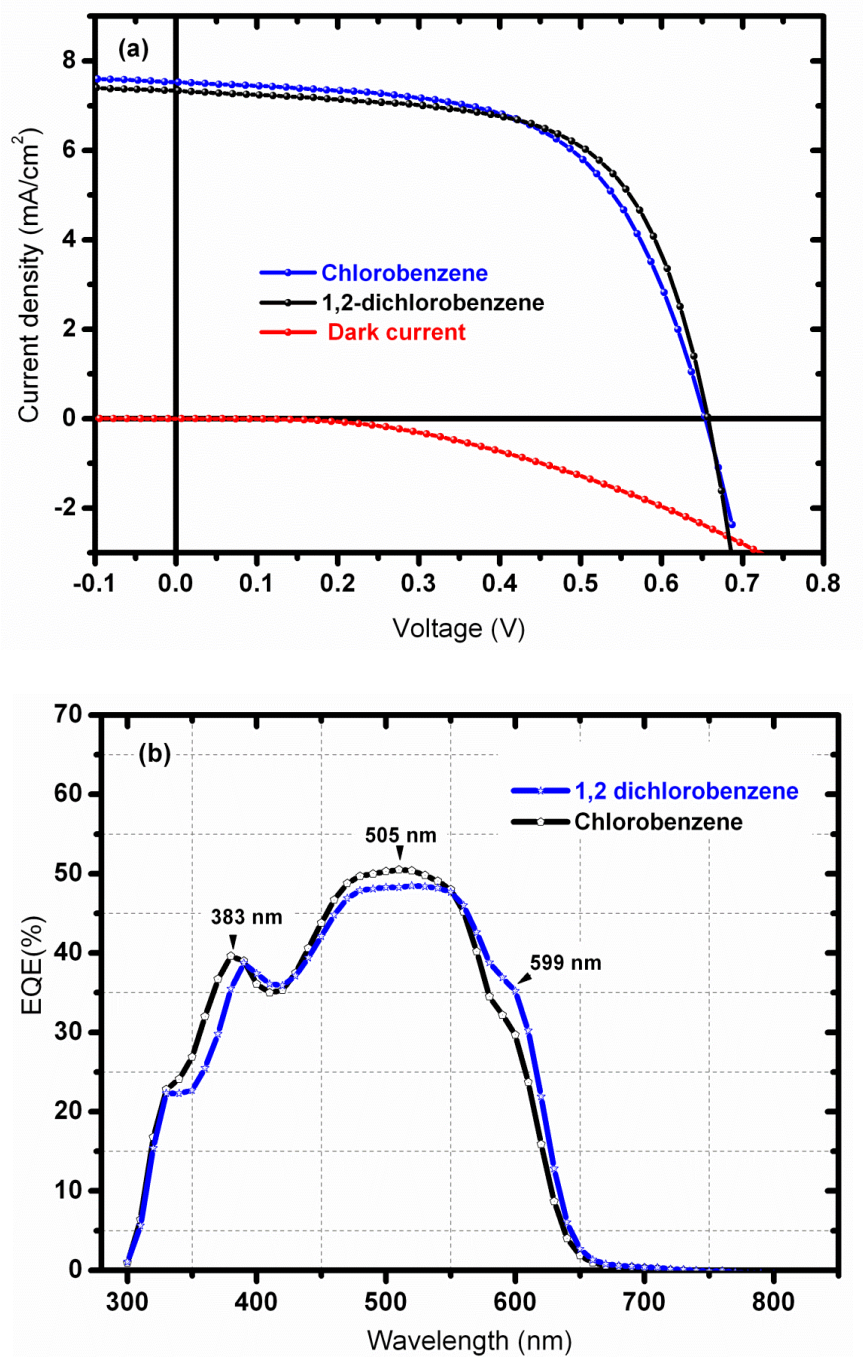

Figure 5.3: (a) Current-density curves (dark and under illumination) (b) external quantum efficiencies of P3HT:PCBM blends OSCs.

Table 5.1: Photovoltaic characteristics of organic solar cells, two solvents

P3HT:PCBM Ratio	P3HT:PCBM Solvent	$J_{sc}(mA/cm^2)$	$V_{oc}(V)$	FF(%)	PCE(%)
1:0.6	Chlorobenzene	7.524	0.653	50.42	2.94
1:0.6	1,2-diChlorobenzene	7.333	0.657	48.25	2.86

It is evident that CB is a better solvent for better performance of OSCs and the weight ratio of P3HT:PCBM blend significantly affects the efficiency. We investigated at which weight ratio using CB as a solvent in P3HT:PCBM blend can a maximum PCE of OSCs be obtained. The J-V and EQE curves of the photovoltaic devices having P3HT:PCBM weight ratios are shown in figure 5.4 (a) and (b). The PCE are 2.45 %, 1.97 %, 1.77 % and 1.91 % for devices with the weight ratios 1:0.6, 1:0.8, 1:1 and 1:1.2, respectively. The PCE and FF decrease with an increase of PCBM weight and then increases. This is demonstrated in figure 5.5 (a). The device with the ratio 1:0.6 demonstrates the maximum performance with PCE of 2.45 %, FF of 54.95 %, J_{sc} of 7.14 mA/cm2 and V_{oc} of 0.62 V. The behavior of V_{oc} and J_{sc} are shown in figure 5.5(b). At lower ratio of 1:0.6 the PCBM content makes it possible to form effective interpenetrating network morphology for exciton diffusion and dissociation at the interface between two components. In addition, even when the PCBM content increases, it is still enough to produce an effective donor/acceptor interface for exciton dissociation and to form percolation pathways for charge transport to the electrodes. However, at high concentrations of PCBM, aggregation may occur which may deter exciton generation, separation and transport in the active layer [13]. This is in agreement with the absorption measured in figure 5.2, were absorption became weaker as the weight of PCBM was increased in the blend. The dependence of the photovoltaic performance on PCBM content was further confirmed by EQE curves shown in figure 5.4(b). Shoulders at ~348 nm and ~600 nm are observed with the maximum photons absorbed at ~490 nm. Even though the maximum conversion efficiencies are observed in the device with 1:0.6 ratio, EQE reveals that the device with ratio 1:1.2 have better overall performance. The slight shift of peak at ~362 nm in the 1:1 ratio device may be due to the degree of solubility of PCBM in the P3HT:PCBM blend.

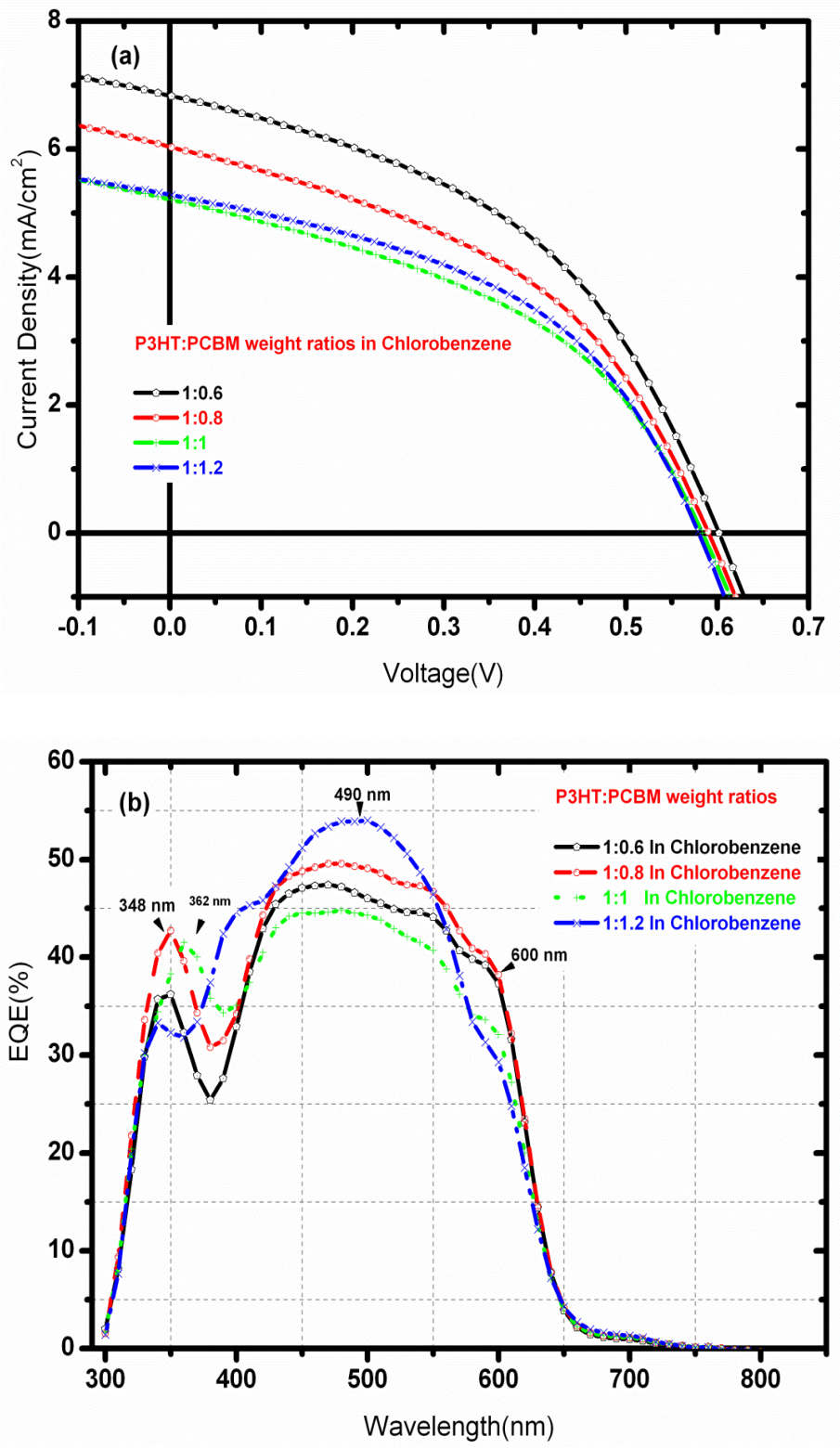

Figure 5.4: (a) Current-density curves (b) external quantum efficiencies of P3HT:PCBM blends OSCs.

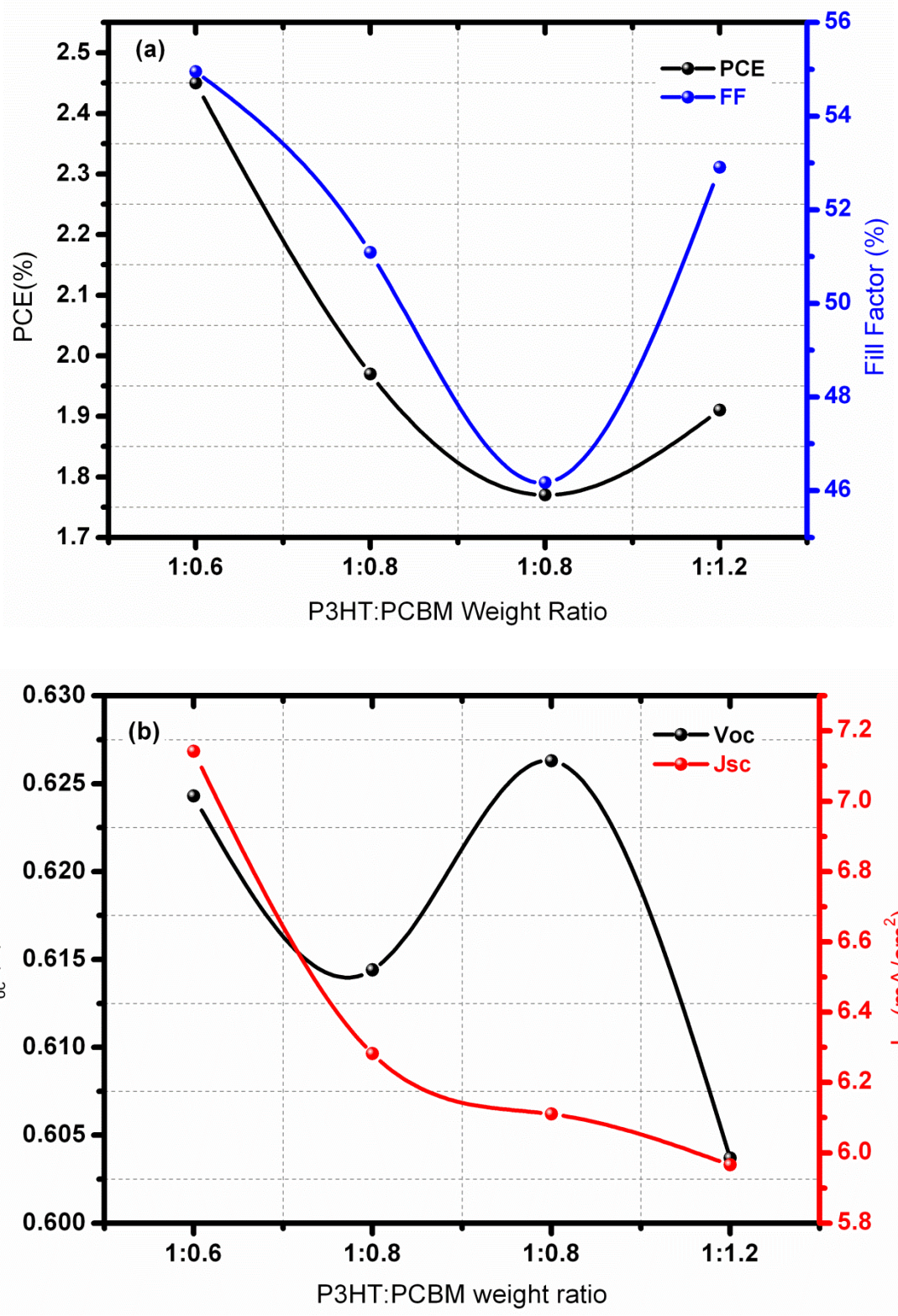

Figure 5.5: Efficiency parameters of OSCs with respect to the P3HT:PCBM weight ratios.

5.4. Conclusion

In conclusion, photovoltaic properties of solution processed OSCs based on P3HT:PCBM blend system from chlorobenzene and 1,2-dichlorobenzene solvents were investigated. J_{sc}, FF and PCE of the OSCs were shown to significantly depend on the solvent in which the photoactive layer material is dissolved and also on the weight ratio of P3HT:PCBM. Maximum PCE was observed when using chlorobenzene as a solvent and at the P3HT:PCBM ratio of 1:0.6. Chlorobenzene is generally used as a solvent because both PCBM and P3HT are soluble in it, although 1,2-dichlorobenzene has also shown comparable device performance. In addition the vastly improved performance of the device cast from chlorobenzene can be attributed to factors like the length scale of phase segregation is the same order of magnitude as the exciton diffusion length or the more bicontinous nature of the films facilitates charge transport.

References

[1] W. Ma, C. Yang, X. Gong, K. Lee and A.J Heeger, *Advanced Functional Materials* **15**(2005)1617-1622

[2] S.R Cowan, N. Banerji, W-L Leong and A.J Heeger, *Advanced Functional Materials* **22**(2012) 1116-1128

[3] B. Zhang, D-H Lee, H. Chae, C. Park and H-M Cho, *Korean Journal of Chemical Engineering* **27**(2010) 999-1002

[4] K. Kawano, J. Sakai, M. Yahiro and C. Adachi, *Solar Energy Materials and Solar Cells* **93**(2009) 514-518

[5] A. Bagui and S.Iyer, *IEEE Transactions on Electron Devices* **58**(2011) 4061-4066

[6] M.T Dang, L Hirsch and G. Wantz, *Advanced Materials* **23** (2011) 3597-3602

[7] Y. Kim, S.A Choulis, J. Nelson and D.D.C Bradley, *Journal of Materials Science* **40**(2005) 1371-1376

[8] L. Ligui, L. GuangHao, Y XiaoNiu and Z. Enle, *Chinese Science Bulletin* **52**(2007) 145-158

[9] T. Hori, V. Kittichungchit, H. Moritou, H. Kubo, A. Fujii and M. Ozaki, *Materials* **3**(2010) 4939-4949

[10] G. Li, V. Shrotriya, Y. Yao, J. Huang and Y. Yang, *Journal of Materials Chemistry* **17**(2007) 3126-3140

[11] J. Lee. A. Kim, S. MinCho and H. Chae, *Korean Journal of Chemical Engineering* **29**(2012) 337-340

[12] J.G Van Dijken, M.D Fleischauer and M.J Brett, *Organic electronics* **12**(2011) 2111-2119

[13] B. Yin, L. Yang, Y. Liu, Y. Chen, Q. Qi, F. Zhang and S. Yin, *Applied Physics Letters* **97**(2010) 023303-1 – 023303-3

6 Effects of particle morphology of ZnO buffer layer on the performance of organic solar cell

In this chapter the effects of concentration and particle morphology (nanoparticle versus nanoflake) of ZnO electron extraction layer on the performance of the based organic solar cell OSC devices are presented. The devices were fabricated by spin-coating poly(3,4-ethylenedioxythiophene) poly(styrenesulfonate) (PEDOT:PSS) polymer on a glass substrates pre-coated with a layer of transparent indium-tin-oxide (ITO) followed consecutively by layers of blends of poly(3-hexylthiopene) (P3HT) and [6,6] –phenyl C_{61}-butyric acid methyl ester (PCBM), ZnO nanoparticles/nanoflakes and aluminium metal. The configuration of the device was ITO/PEDOT:PSS/P3HT:PCBM/ZnO/Al. The concentration of ZnO nanoparticle or nanoflake solutions was varied from 0.5 to 20 mg/ml. The power conversion efficiency (PCE) of 3.08 % was recorded from devices incorporating ZnO nanoflake electron extraction layer, whereas the PCE of 2.37% was recorded from devices incorporating ZnO nanoparticles as the electron extraction layer. The maximum PCE was obtained from a concentration of 0.5 mg/ml ZnO for both devices. The influence of the particle morphology and the concentration of the ZnO electron extraction layer on the general performance of the OSC devices are discussed in detail.

6.1. Introduction

Organic solar cell devices often show poor device stability especially because of (i) the use of air-sensitive low work function metals such as Ca or Al, and (ii) metal atom diffusion [1]. In this regard, metal oxide nanoparticles have emerged as an important class of materials to act as an electron extraction layer, when they are inserted between the photoactive layer and the top electrode. An electron extraction layer of a wide band gap semiconducting material such as ZnO or TiO_2, that facilitates the electron transport from the photo-active layer (P3HT:PCBM blend) to the top metal electrode (e.g. Al) and, at the same time, blocks holes from reaching the top electrode is often used. For instance, Qian et al [2] reported that the ZnO nanoparticle electron extraction layer prevents diffusion of Al atoms into the photo-active layer and that it also has the potential to improve the environmental stability of the OSC devices by absorbing UV photons

that could lead to bond breaking or photo-oxidation in the presence of water and/or oxygen molecules. They demonstrated an improved stability and a 30–80% improvement in PCE of PH3T-CdSe OPV devices using ZnO nanoparticles as an electron extraction layer. It therefore showed that device performance can be improved by incorporating metal oxide (e.g. TiO_2 or ZnO) nanoparticle electron extraction layers. With their relatively high electron mobility and hole blocking capability, ZnO nanoparticles can improve charge collection and prevents carrier recombination at the interface of the photoactive layer [3,4]. For further PCE improvement, intensive studies on the formation and properties of the thin metal oxide electron extraction layer are highly needed. Here, the influence of concentration and particle morphology of ZnO thin film on the performance of the OSC devices are reported. The ZnO thin films were spin-coated from ZnO nanoparticle or ZnO nanoflake solutions. Note that in the best of the author's knowledge, this is the first report that utilizes ZnO nanoflakes in OSC devices. The ZnO nanostructures were characterized using X-ray diffraction (XRD), Field-emission scanning electron microscopy (FE-SEM), Atomic force microscopy (AFM), and UV-visible spectrometer. The performance of the OSCs incorporating a ZnO nanoflake electron extraction layer was shown to be superior to that using a ZnO nanoparticle electron extraction layer. Furthermore, the ZnO solution concentration was found to be critical to optimizing the photovoltaic performance of the devices.

6.2. Experimental

A wet chemistry route was used to synthesize ZnO nanoparticles and nanoflakes and the synthesis is discussed in details in chapter 4, section 4.4. The organic solar cell devices consisting of successive layers of poly(3,4-ethylenedioxythiophene) poly(styrenesulfonate) or PEDOT:PSS (hole extraction layer), a blend of poly(3-hexyltheopene):[6,6]-phenyl C61-butyric acid methyl ester or P3HT:PCBM (photo-active layer) , ZnO nanoparticles/nanoflakes (electron extraction layer) and aluminum (Al) top electrode (cathode) spin-coated on a glass substrate pre-coated with a layer of transparent indium-tin-oxide or ITO (anode) were fabricated. The glass substrate was cleaned ultrasonically in isopropyl alcohol and acetone, consecutively for each 10 min, then followed by drying at ~80 ^{o}C for 20 min and was lastly treated in an ultraviolet ozone generator for 20 min. A thin layer of poly(3,4-PEDOT:PSS (CLEVIOS™ AI 4083) was spin-coated on the cleaned ITO pre-coated glass substrate at the speed of 4000 rpm for 35 s followed by drying in an oven/hot plate at 110 ^{o}C for 10 min. The active layer of P3HT:PCBM blend with a weight ratio of 1:0.6, dissolved in chlorobenzene, was spin-coated at the speed of 1000 rpm for

15 s. This was followed by the deposition of the layer of methanol solution of ZnO nanoparticles/nanoflakes at 4000 rpm for 35 s. Electron extraction layers of ZnO nanoparticles/nanoflakes were spin-coated with four different concentrations of 0.5, 1, 2 and 20 mg/mL. The top Al metal electrode (100 nm) was thermally evaporated at ~ 1 x 10^{-6} Torr pressure through a shadow mask and the device area was 0.12 cm^2. All the devices were then thermally treated at 155 ^oC for 10 min. The device structure was ITO/PEDOT:PSS/P3HT:PCBM/ZnO (nanoparticles or nanoflakes)/Al. The schematic diagram of the device structure and the simplified energy level diagram for different layers of the device are shown in Figure 6.1(a) and (b). The lower conduction band edge of ZnO as compared to the lowest unoccupied molecular orbital (LUMO) of P3HT should allow dissociation of excitons formed in P3HT via rapid electron transfer to ZnO [2]. It is expected that there is nearly an Ohmic contact between PCBM to ZnO for electron transport.

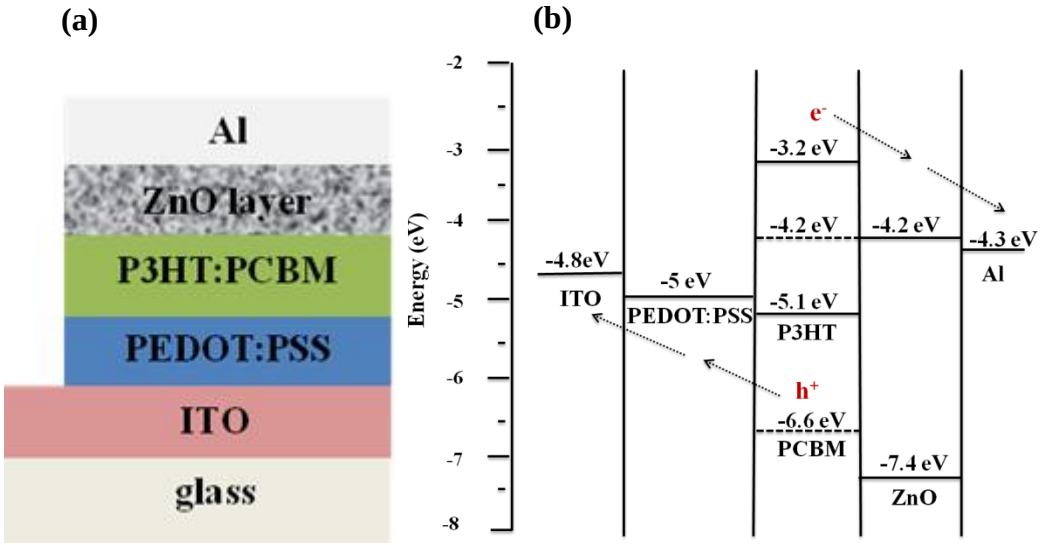

Figure 6.1: (a) Device structure of the organic solar cell with the electron extraction layer of ZnO nanostructures and (b) the energy level diagram of each component of the device (the energies are referenced to the vacuum level).

Film and Device Characterization: The UV-Vis absorption of ZnO nanostructures and P3HT:PCBM blend films were evaluated using a Perkin – Elmer Lambda 35 UV-Vis-NIR spectrophotometer. The morphology of the films was analyzed using a field-emission scanning electron microscope (FE-SEM, Nova-nano SEM^{200}, FEI) and the surface topography was analyzed by atomic force microscopy (AFM, Shimadzu SPM-9600). The current density-voltage

(J-V) curves were measured in air using a Keithley 2400 source meter and an Oriel xenon lamp (150 W) coupled with an AM1.5 filter to simulate sunlight. The light intensity was calibrated with a silicon reference cell with a KG2 filter following standard solar cell testing procedures. All J-V measurements were conducted at the light intensity of 100 mW/cm^2. The external quantum efficiencies (EQE) as a function of wavelength were measured using an incident photon-to-current efficiency (IPCE) measurement system (PV measurement, Inc). The wavelength of the bias light was controlled with optical filters (Andover Corporation).

6.3. Results and discussion

XRD patterns of ZnO nanoparticles/nanoflakes are shown in Figure 6.2 and they both are consistent with the hexagonal wurtzite structure of ZnO. Notice that the diffraction peaks of the nanoparticles were broad while those of the nanoflakes were narrow and sharp. Broad diffraction peaks are indicative of smaller particle sizes while sharp narrow peaks point to relatively bigger particle sizes and higher crystallinity. The average crystallite sizes of the nanoparticles and nanoflakes were estimated from the XRD data using the Scherrer equation (see chapter 4, equation 4.1) and were found to be ~5 ± 0.2 nm and ~20 ±0.2 nm, respectively. Secondary phases were observed from the XRD patterns of the nanoflakes and these could be due to the concentration super-saturation of the reactants or short reaction times. It has been reported that an increase in the super-saturation can decrease the solubility of the reactants [5] thereby leading to incomplete reaction of the precursors. Figure 6.3(a-d) shows the FE-SEM images of ZnO nanoparticles or nanoflakes spin-coated from a solution concentration of 2 mg/mL and their respective device cross-sectional view. Figure 6.3(a) shows an agglomeration of spherical ZnO nanoparticles distributed throughout the substrate area and the high density nanoflakes in Figure 6.3(c) are randomly oriented. Figures 6.3(b) and (d) show the cross-sectional images that reveal the components layers of the devices, i.e. ZnO nanoparticles or nanoflakes film, P3HT:PCBM film, PEDOT:PSS, ITO and glass substrate.

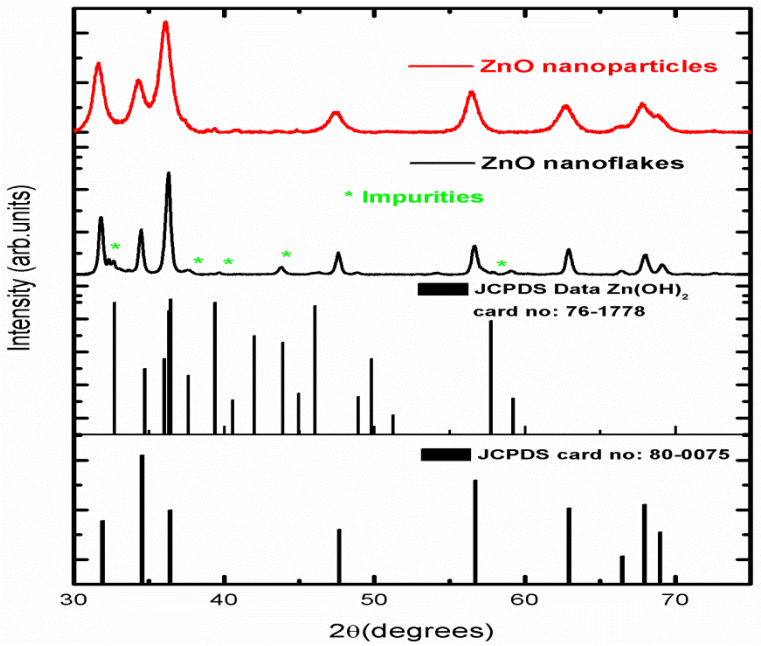

Figure 6.2: XRD patterns of ZnO nanoparticles (red) and nanoflakes (black)

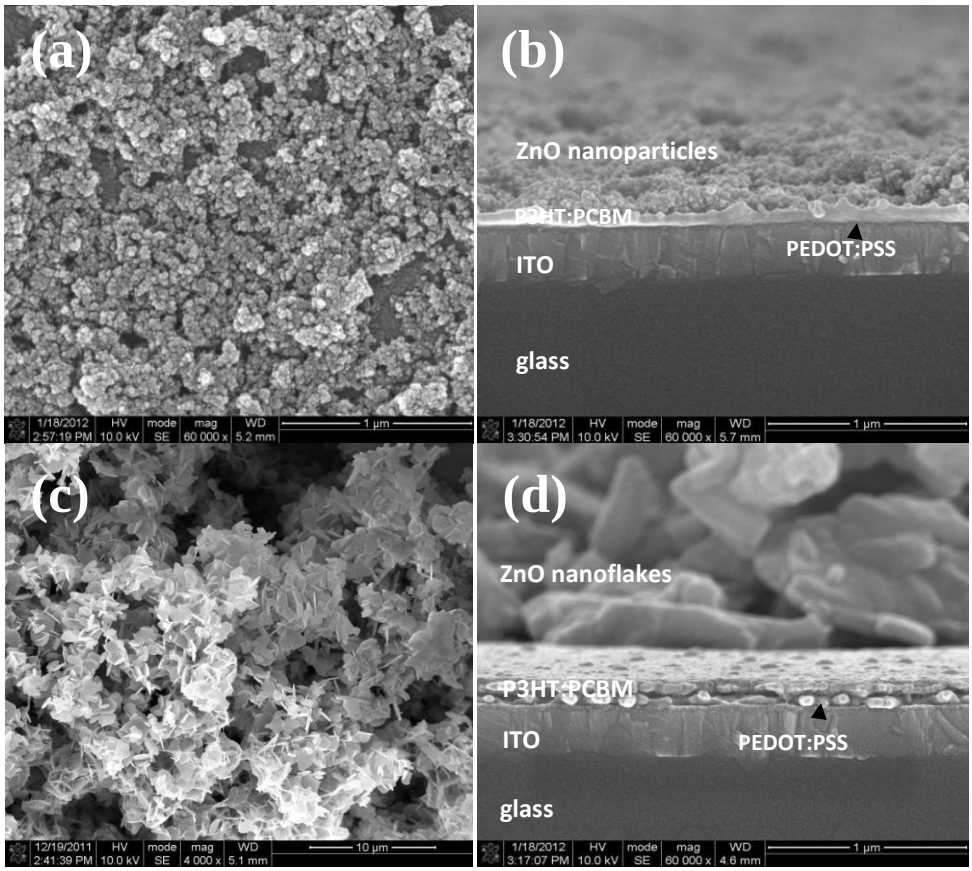

Figure 6.3: FE-SEM images of ZnO nanopaticles and nanoflakes (a-c) from 2mg/ml concentration and cross-sectional images showing components layers of the devices (b-d).

The UV-visible absorption spectra of ZnO nanoparticles/nanoflakes and P3HT:PCBM (inset) blend films spin-coated from methanol and chlorobenzene solutions, respectively, are shown in Figure 6.4(a). P3HT:PCBM blend film show broad absorption of P3HT polymer in the visible range of the spectrum with maximum at 510 nm. The shoulder around 557 nm and 609 nm are attributed to the P3HT vibronic transitions and indicates the high ordering of P3HT [6]. ZnO nanoparticles exhibit two absorption peaks at 251 and 348 nm. The major absorption peak at 348 nm is a well known intrinsic band gap absorption of ZnO, and it is attributed to electronic transitions from the valence band to the conduction band while the minor absorption peak at 251 nm is attributed to impurities or structural defects associated with either Zn or O vacancies [7,8]. In the case of the ZnO nanoflakes, the intrinsic band gap absorption is suppressed and only the 251 nm peak associated with the structural defects was observed. The suppression of the intrinsic band gap absorption in the ZnO nanoflakes could be due to restricted carrier mobility from the top of the valence band to the conduction band due to high density of secondary phases (confirmed by the XRD data) or high density of vacancies. The optical absorption of a direct band gap semiconductor can be calculated using equation 6.1 [9]:

$$\alpha h\upsilon = A(h\upsilon - E_g)^{1/2} \qquad (6.1)$$

where A is the proportionality constant, α is the absorption coefficient and $h\upsilon$ is the photon energy (h = Planck's constant and υ = frequency of the photon). By plotting $(\alpha h\upsilon)^2$ against $h\upsilon$, E_g can be estimated by extrapolating the linear portion of the curve to zero absorption [9]. The estimated optical band gap was ~3.34 eV for ZnO nanoparticles as shown in Figure 6.5. Although the band gap of the ZnO nanoflakes could not be estimated using equation (6.1) due to lack of band to band absorption, we expect it to be smaller than that of the nanoparticles because of their bigger particle sizes with higher crystallinity than the nanoparticles as shown in the XRD data in figure 6.2.

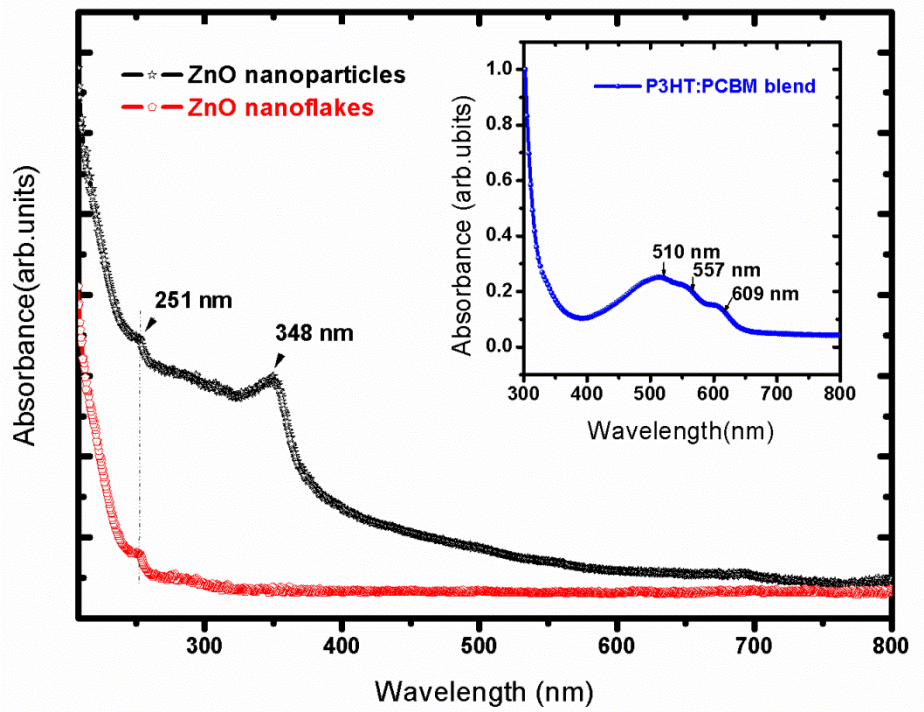

Figure 6.4: UV-vis absorption spectra of ZnO nanoparticles/nanoflakes films. The inset shows P3HT:PCBM blend

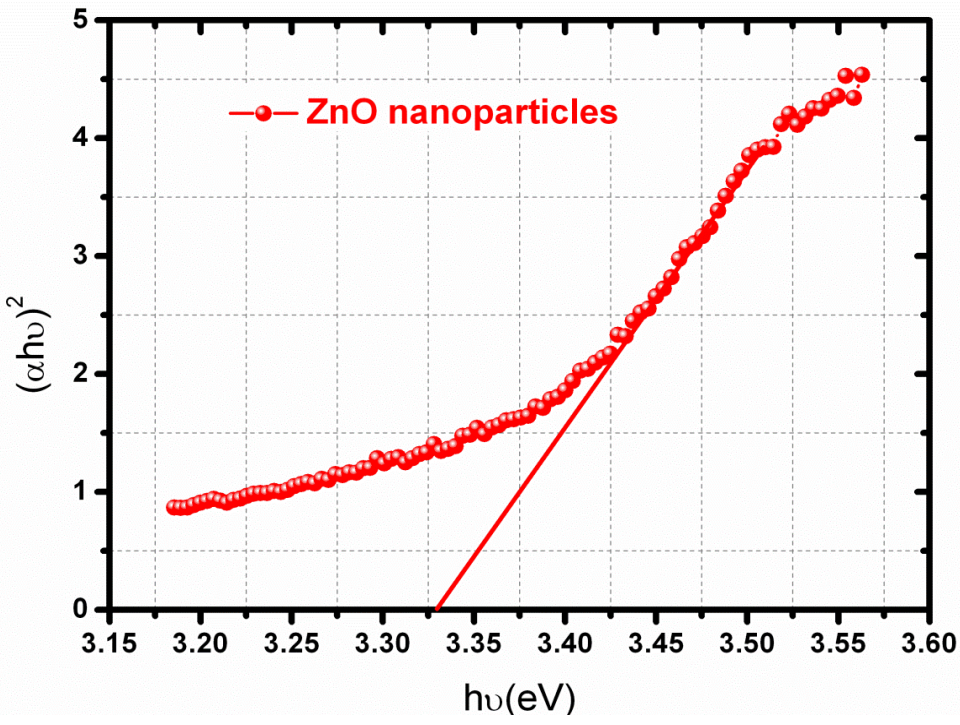

Figure 6.5: Plots of $(\alpha h\upsilon)^2$ vs photon energy ($h\upsilon$) of ZnO nanoparticles

The surface topography of the device layers was examined using contact-mode AFM. Figures 6.6(a-f) show topographic images of PEDOT:PSS, P3HT:PCBM, ZnO nanoflakes electron extraction layer, ZnO nanoparticles electron extraction layer, and Al layer scanned from P3HT:PCBM/ZnO/Al and Al layer scanned from P3HT:PCBM/Al device geometries, respectively. The lowest rms value of 1.02 (± 0.01) nm demonstrates surface smoothening effect of PEDOT:PSS. The other layers (P3HT:PCBM and Al, figure 6.6(b) and (f)) show a distribution of particles and their rms roughnesses were 5.2 (± 0.2) nm and 5.4 (± 0.4) nm, respectively. The ZnO nanoparticles and nanoflakes (2mg/ml concentration) rms roughnesses were 52 (± 3.6) nm and 3.5 ± 0.5 nm, respectively, and the Al layer (figure 6.6e), shows the roughness of 58 (± 3.2) nm.

The layers in figure (b),(d) and (e) show much coarser texture with broad hill-like features and an increased surface roughness compared to the other films. This is most likely due to annealing and ordered structure formation in the film [10]. It has been reported that rougher interface between the photo-active layer and the top electron can improve efficiency of organic solar cell devices by increasing light harvest in the photo-active layer and by subsequently preventing the formation of shunt paths [11,12]. As discussed, it is reasonable to attribute high PCE value of 3.08% from the OSC device with ZnO nanoflakes to increased light harvest by rougher interfacial morphology. However, Qian et al [2] reported improved efficiency from OSC devices with relatively smooth interface morphology. They reported that the improved electrical contact between the cathode and the photoactive layer enabled the efficient collection of photo-generated electrons.

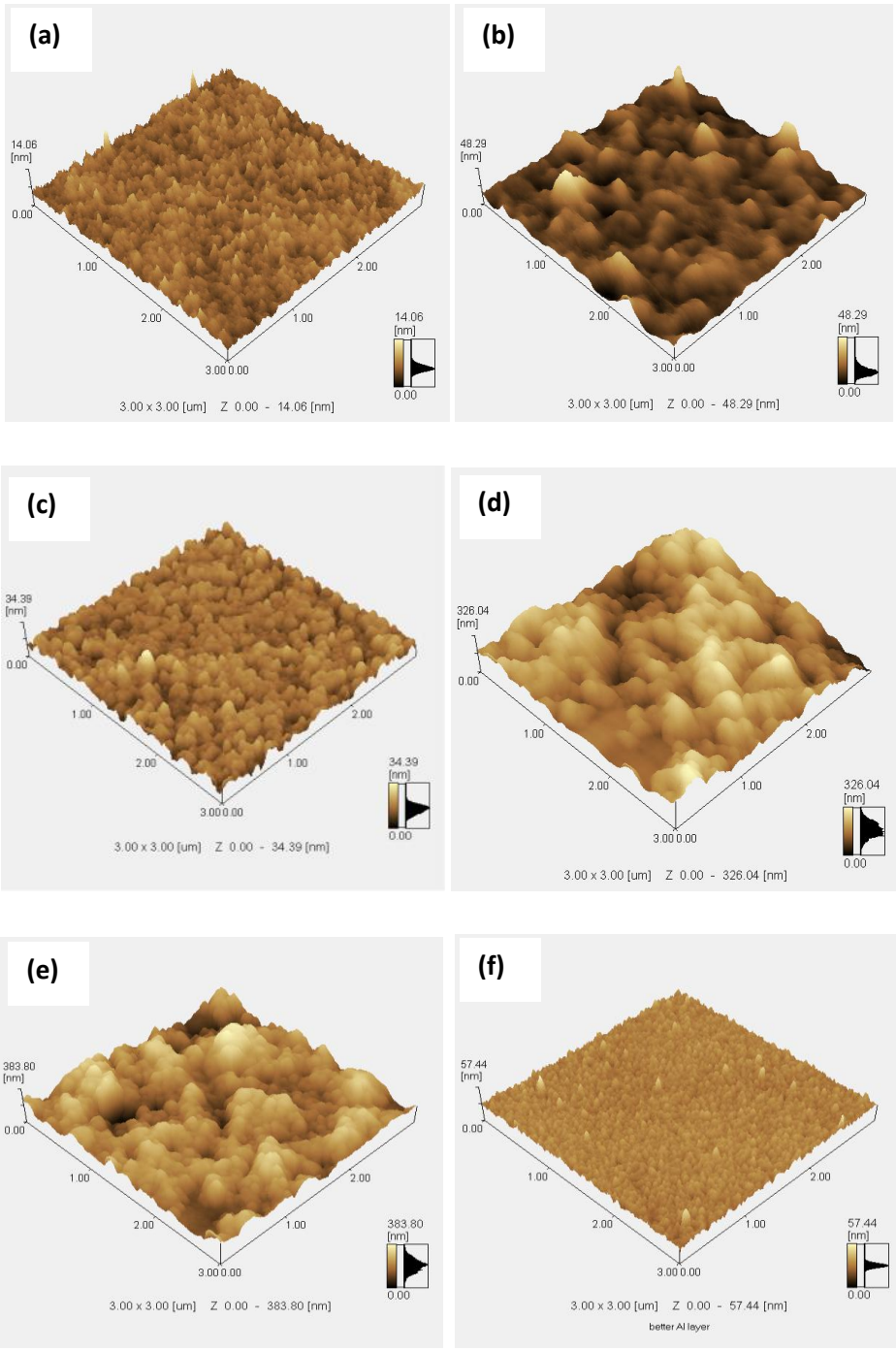

Figure 6.6: Contact-mode AFM topographic images of (a) PEDOT:PSS, (b) P3HT:PCBM, (c) ZnO nanoparticles electron extraction layer (d) ZnO nanoflakes electron extraction layer, and (e) Al layer from P3HT:PCBM/ZnO nanoflakes/Al and (f) Al Layer from P3HT:PCBM/Al device geometries.

Figure 6.7 compares the photovoltaic properties of the OSC devices with ZnO nanoflakes and nanoparticles electron extraction layers spin-coated from solutions of 0.5 mg/mL concentration. The photovoltaic performance parameters including short circuit current dentsity (J_{sc}), open circuit voltage (V_{oc}), fill factor (FF) and power conversion efficiency (PCE) of the devices with different concentrations of the ZnO solutions are presented in Table 6.1. The current-density (J-V) characteristics and external quantum efficiencies (EQEs) of the devices are presented in figure 6.7(a) and (d) respectively. Although both devices recorded almost the same values of V_{oc} on average, the devices with the ZnO nanoflakes recorded relatively higher values of the J_{sc} and FF, and subsequently higher values of the PCE as shown in Table 6.1. The highest PCE values of 2.37 % and 3.08% were obtained from the devices spin-coated from the ZnO nanoparticles and nanoflakes solutions of 0.5 mg/mL concentration respectively.

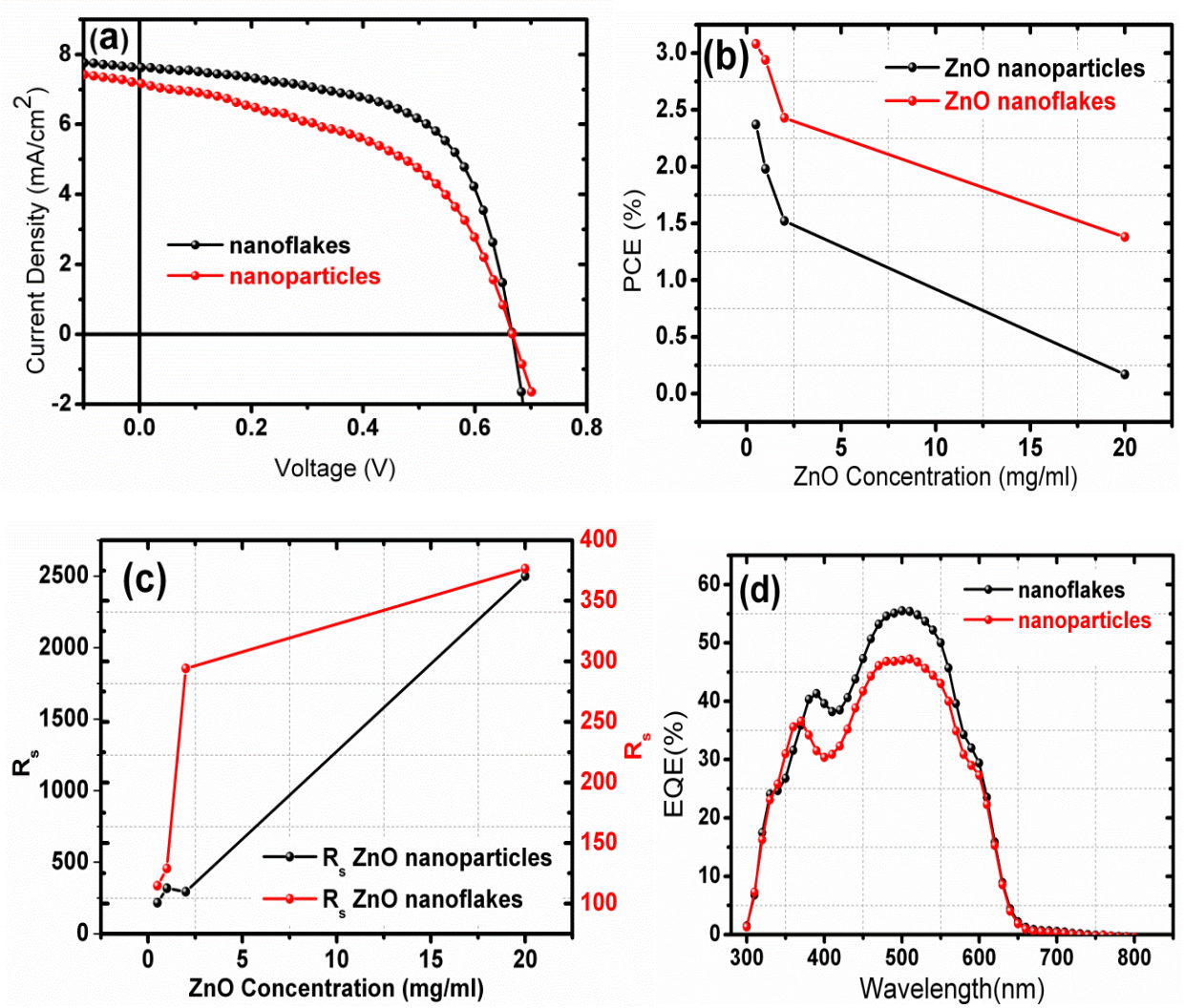

Figure 6.7: (a) J-V curves (b) PCE vs ZnO concentration(c) Series resistance as a function of ZnO concentration and (d) EQE of devices.

Other than the differences in particle morphology (shape and size), the high PCE value recorded from the device with the nanoflakes electron extraction layer suggests that the nanoflakes made a relatively superior contact with the photo-active layer and the top electrode compared to the nanoparticles. Liang et al [4] have pointed out that the surface quality of the ZnO layer can lead to improved photovoltaic properties of the devices. The AFM data show that the nanoparticle layer with the rms value of 3.5 nm was by far smoother than that of the nanoflakes layer with the rms value of 52 nm. Figure 6.7(b) shows the plot of the PCE versus ZnO concentration. The photovoltaic performance was found to be dependent on the particle shape and concentration ZnO. The device with the ZnO nanoflakes electron extraction layer showed a significant enhancement of the PCEs from ~1.38 to 3.08 % as the ZnO concentration decreased from 20 mg/mL to 0.5 mg/mL. Similarly, the device with ZnO nanoparticles also showed such an increase of PCEs from ~ 0.17 to 2.37 % as the concentration decreased with the lower maximum PCE. When the ZnO concentration increases, the amount of solute particles increases in the solution, thereby increasing the probability of clustering together to form larger grains. In other words, at lower concentrations, clustering is minimal, which makes contact between the photoactive layer and the Al layer better. In addition, From the AFM and SEM imaging the ZnO nanoflakes film is much rougher than the ZnO nanoparticles film. It therefore demonstrates that the surface and film quality of the electron extraction layer can make a direct impact on the contact between the active layer and the ZnO layer, thus influencing the photovoltaic performance of the device [4]. It is therefore reasonable to conclude that the high PCE value of 3.08% recorded from the device with the nanoflakes buffer layer was a result of improved collection of the photon generated electrons from the rougher interface between the photo-active layer and the top electron which may improve the efficiency of the device by increasing light harvest in the photo-active layer and by subsequently preventing the formation of shunt paths.

One way of determining the impact of contacts between the buffer layer and the photoactive layer and between the buffer layer and the top electrode on the general performance of the devices is by evaluating series resistance (R_s) and shunt resistance (R_{sh}). On the one hand, good contact between the ZnO layer and the photoactive layer can decrease R_s by improving collection and transportation of electrons to the cathode. On the other hand, poor contact between the ZnO layer and the photoactive layer and between the ZnO layer and the top electrode can lead to low shunt resistance values and a subsequent low PCE due to creation of alternative current paths. Table 6.2 presents R_s and R_{sh} values independently calculated from the inverse slope of the J-V

curves of the devices at $I = J_{sc}$ ($V = 0$) and $V = V_{oc}$ ($I = 0$), respectively. As shown in Table 6.2 and Figure 6.7(c), the R_s increases with an increase of the ZnO concentration, resulting in the decrease of PCE while the R_{sh} increases with a decrease of the ZnO concentration resulting in the increase of the FF, J_{sc} and PCE values. These data are consistent with the data reported by Liang et al [4]. Again it can be concluded that due to superior contact, ZnO nanoflakes serve as better transport pathways for electrons and the parasitic losses are lower than those of ZnO nanoparticles.

The improvement in device performance is also observed from the EQE of the devices, as shown in Figure 6.7(d). There is a significant increase in EQE for the device with the ZnO nanoflakes electron extraction layer with a maximum of ~55 % at the wavelength of 505 nm versus ~47 % for the ZnO nanoparticles electron extraction layer. Liang et al [4] reported that increased optical transmittance of the ZnO extraction layer should lead to enhanced absorption of the photoactive layer and better general performance of the OSC devices. While not measured in this study, it is reasonable to assume that the optical transmittance of the ZnO nanoflakes electron extraction layer was better than that of the nanoparticles and this could be one of the factors that contributed to improved photovoltaic properties of the devices.

Table 6.1: Photovoltaic comparison of P3HT:PCBM solar cells with different concentrations of ZnO nanoparticles and nanoflakes

Concentration (mg/mL)	ZnO nanoparticles				ZnO nanoflakes			
	J_{sc} (mA/cm^2)	V_{oc} (V)	FF (%)	PCE (%)	J_{sc} (mA/cm^2)	V_{oc} (V)	FF (%)	PCE (%)
0.5	7.18	0.67	49.5	2.37	7.63	0.67	60.6	3.08
1	6.67	0.65	45.8	1.98	7.45	0.67	59.2	2.94
2	6.38	0.67	35.7	1.52	6.94	0.66	52.8	2.43
20	0.74	0.64	36.3	0.17	6.01	0.61	37.8	1.38

Table 6.2: Series and Shunt Resistance comparison of P3HT:PCBM solar cells with different concentrations of ZnO nanoparticles and nanoflakes

Concentration (mg/ml)	ZnO nanoparticles		ZnO nanoflakes	
	$R_s(\Omega.cm^2)$	$R_{sh}(\Omega.cm^2)$	$R_s(\Omega.cm^2)$	$R_{sh}(\Omega.cm^2)$
0.5	217	2900	114	6300
1	318	2650	129	5890
2	295	1850	294	4260
20	2500	9690	377	1940

6.4. Conclusion

In conclusion, the bulk heterojunction organic solar cell devices were successfully fabricated using solution based method with ZnO nanoparticles and nanoflakes electron extraction layers. The effect of concentration and morphology of the ZnO electron extraction layers were investigated. Improved photovoltaic properties were observed from devices with the ZnO nanoflakes and nanoparticles electron extraction layers spincoated from solutions of 0.5 mg/mL concentration with the nanoflakes giving a relatively high PCE value of 3.08% versus 2.37% from the nanoparticles. The improved PCE from ZnO nanoflakes electron extraction layer was attributed to reduced clustering at lower concentration and subsequently an efficient collection of the photon generated electrons due to smooth interface and superior contact between the nanoflakes and the photo-active layer and also between the nanoflakes and the Al top electrode.

References

[1] K. Lee, J.Y. Kim, S.H. Park, S.H. Kim, S. Cho and A.J. Heeger, *Advanced Materials* **19**(2007) 2445-2449

[2] L. Qian, J. Yang, R. Zhou, S. Tang, Y. Zheng, T.-K. Tseng, D. Bera, J.Xue and P.H. Holloway, *Journal of Materials Chemistry* **21**(2011) 3814-3817

[3] N. Sekine, C-H. Chou, W-L. Kwan and Y. Yang, *Organic Electronics* **10**(2009) 1473-1477

[4] Z. Liang, Q. Zhang, O. Wiranwetchayan, J. Xi, Z. Yang, K. Park, C. Li and G. Cao, *Advanced Functional Materials* **22**(2012) 2194-2201

[5] G. Oskam, F. de Jes´us Peet Poot, *Journal of Sol-Gel Science and Technology* **37** (2006) 157-160

[6] D.C Olson, Y-J. Lee, M. S. White, N. Kopidakis, S.E. Shaheen, D.S. Ginley, J.A. Voigt and J.W.P. Hsu, *Journal of Physical Chemistry* **111**(2007) 16640-16645

[7] D.Bera, L.Quian, S.Sabui, S.Santa and P.H Holloway, *Optical materials* **30**(2008) 1233-1239

[8] P.Kumbhakar, D.Singh, C.S. Tiwary and A.K Mitra, *Chalcogenide Letters* **5**(2008) 387-394

[9] H. Oh, J. Krantz, I. Litzov, T. Stubhan, Luigi. Pinna and C.J. Brabec, *Solar Energy Materials and Solar Cells* **95**(2011) 2194-2199

[10] G. Li, V. Shrotriya, Y. Yao, J. Huang and Y. Yang, *Journal of Materials Chemistry* **17**(2007) 3126-3140

[11] O.M. Ntwaeaborwa, R Zhou, L Qian, S.S. Pitale, J. Xue, H.C. Swart, P.H. Holloway, *Physica B* **407** (2012) 1631-1633

[12] H. Kim, W.-W. So, S.-J. Moon, *Solar Energy Materials and Solar Cells* **91**(2007) 581-587

7 Effects of thermal treatment and surface analysis of bulk heterojunction organic solar cells by TOF-SIMS technique

In this chapter the effects of thermal treatment on the bulk heterojunction (BHJ) organic solar cells with ZnO nanoparticles buffer layer between the active layer and the cathode electrode aluminum (Al) are investigated. The BHJ organic solar cells comprised of poly(3-hexylthiophene) (P3HT) and [6,6]-phenyl butyric acid methyl ester (PCBM) as photoactive layer blend on the substrate coated with a hole transporting layer poly(3,4 ethylenedioxythiophene):poly(styrenesulfonate) (PEDOT:PSS) followed by ZnO nanoparticles buffer layer. The devices were then annealed at 155 ^{o}C before and after the deposition of the Al electrode. Devices annealed after the deposition of Al electrode showed improved photovoltaic characteristics as compared to the devices annealed before deposition of Al electrode. Depth profile analysis and surface imaging of BHJ organic solar cells were performed by time-of-flight secondary ion mass spectrometry (TOF-SIMS). In addition the measurements were performed directly on the Al electrode. Signals arising from ^{27}Al, ^{16}O, ^{12}C, ^{32}S, ^{64}Zn, ^{28}Si, ^{120}Sn and ^{115}In allowd a clear identification of the Al, ZnO, P3HT:PCBM, PEDOT:PSS and ITO/glass layers, respectively. The comparison results between the pre and the post annealed devices depth profiles are discussed in details.

7.1. Introduction

Significant advances in PCE are achieved by the improvement of the photoactive layer morphology and the challenge is to optimize the interfacial area of the donor/acceptor materials, charge mobility within the photoactive layer and the crystallinity of P3HT polymer within the blend. However, the processing conditions such as thermal annealing of BHJ films can help improve the morphology and charge carrier mobility thereby increasing the quantum efficiency of the device [1]. In addition, the sequence of the thermal treatment is critical for the device performance. The organic solar cells with the cathode confinement in the thermal treatment (post annealing) show better performance than the cells without the cathode confinement (pre

annealing) [2]. In many multi-layered electronic devices, the interfaces between their layers govern their properties and changes such as oxidation or the formation of polar layers affect their functioning. Hence, to understand the BHJ structure the study of these interfaces is important for organic solar cells development [3,4,5].

7.2. Experimental

ZnO nanoparticles synthesis

A wet chemistry method was used to synthesize ZnO nanoparticles. The synthesis details are discussed in chapter 4, section 4.4.

Device fabrication

The device geometry was ITO/PEDOT:PSS/P3HT:PCBM/ZnO nanopaticles/Al with the device area of 0.12 cm^2. A glass substrate precoated with ITO and modified by spin-coating a thin layer of PEDOT:PSS followed by drying in an oven/hot plate at 110 ^oC for 10 min was used as an anode electrode. The photoactive layer of P3HT:PCBM blend with a weight ratio of 1:0.6, dissolved in chlorobenzene, was spin-coated at the speed of 1000 rpm for 15 s. This was followed by the deposition of the layer of methanol solution of ZnO nanoparticles at 4000 rpm for 35 s. Finally, the top Al metal electrode (100 nm) was thermally evaporated at ~ 1 x 10^{-6} Torr pressure through a shadow mask defining the device area. Two devices are compared in this study, i.e. Device A was then thermally treated before the evaporation of Al electrode (i.e. pre-annealing) and device B was thermally treated after the evaporation Al electrode (i.e. post-annealing) at 155 ^oC for 10 min.

Photovoltaic performance measurements

Current density versus voltage (J-V) characteristics were measured using a Keithley 2400 source meter and an Oriel xenon lamp (150 W) coupled with an AM1.5 filter to simulate sunlight. The light intensity was calibrated with a silicon reference cell with a KG2 filter following standard solar cell testing procedures. All J-V measurements were conducted at the light intensity of 100 mW/cm^2. The external quantum efficiencies (EQE) as a function of wavelength were measured using an incident photon-to-current efficiency (IPCE) measurement system (PV measurement, Inc). The wavelength of the bias light was controlled with optical filters (Andover Corporation).

SIMS depth profiling and Imaging

Complete devices, device A and B, were characterized by iontof TOF-SIMS[5]. Two depth profiling ion beams operating in the dual beam mode were used. While a primary current of 70 nA of Cs^+ ions is sputtering the crater, the 0.3 pA Bi_3^{++} ion is progressively analyzing the crater bottom, with impact energies of 1 keV (Cs^+) and 30 keV (Bi_3^{++}) and the sputter area of 300×300 μm with the sputter time of 10 sec/scan. Both positive and negative mode of SIMS measurements were performed directly on the Al cathode. The surface imaging was performed with a Cs^+ 0.3 pA primary beam, and was rastered over area of 100 × 100 μm on the sample surface. The two-dimensional images were recorded with a resolution of 512 x 512 pixels. The measurements were performed at the base pressure of 1.5×10^{-9} mbar.

7.3. Results and Discussion

The purpose of annealing before cathode deposition is to remove any residual solvent and to enhance the crystal structure of the active layer, while thermal annealing after cathode deposition is to improve contact between the active layer and the cathode, therefore charge collection at the cathode is improved. The Photovoltaic response of device A and B are illustrated in figure 7.1. The device performance is greatly improved by the thermal treatment after the deposition of the Al cathode (post-annealing). The PCE is significantly increased from 1.57 % to 2.93 %. In addition, the V_{oc} of Device B increased marginally from 0.43 % to 0.65 %. A summary of the PV characteristics is presented in table 7.1. The improvement of the PV properties can be attributed to combined effects of the ZnO buffer layer and post-annealing treatment. This trend is similar to results reported by Ntwaeaborwa et al [6] and Kim et al [7], where they observed that the device with thermal treatment after cathode deposition shows a better performance. The increase of V_{oc} in device B may be attributed to a decrease in ohmic contact at the interface between ZnO layer and Al electrode. The change in ohmic contact at the interface may be a result of energy level re-alignment due to a post annealing treatment as stated by Zhao et al [8]. The change of ohmic contact in organic solar cells is considered to have a strong impact on the V_{oc} and FF of the cell. EQE spectra is shown in figure 7.1 (b), the maximum photocurrent contribution is observed at ~ 501 nm and an improvement of device performance of about 10 % is obtained for device annealed after Al deposition.

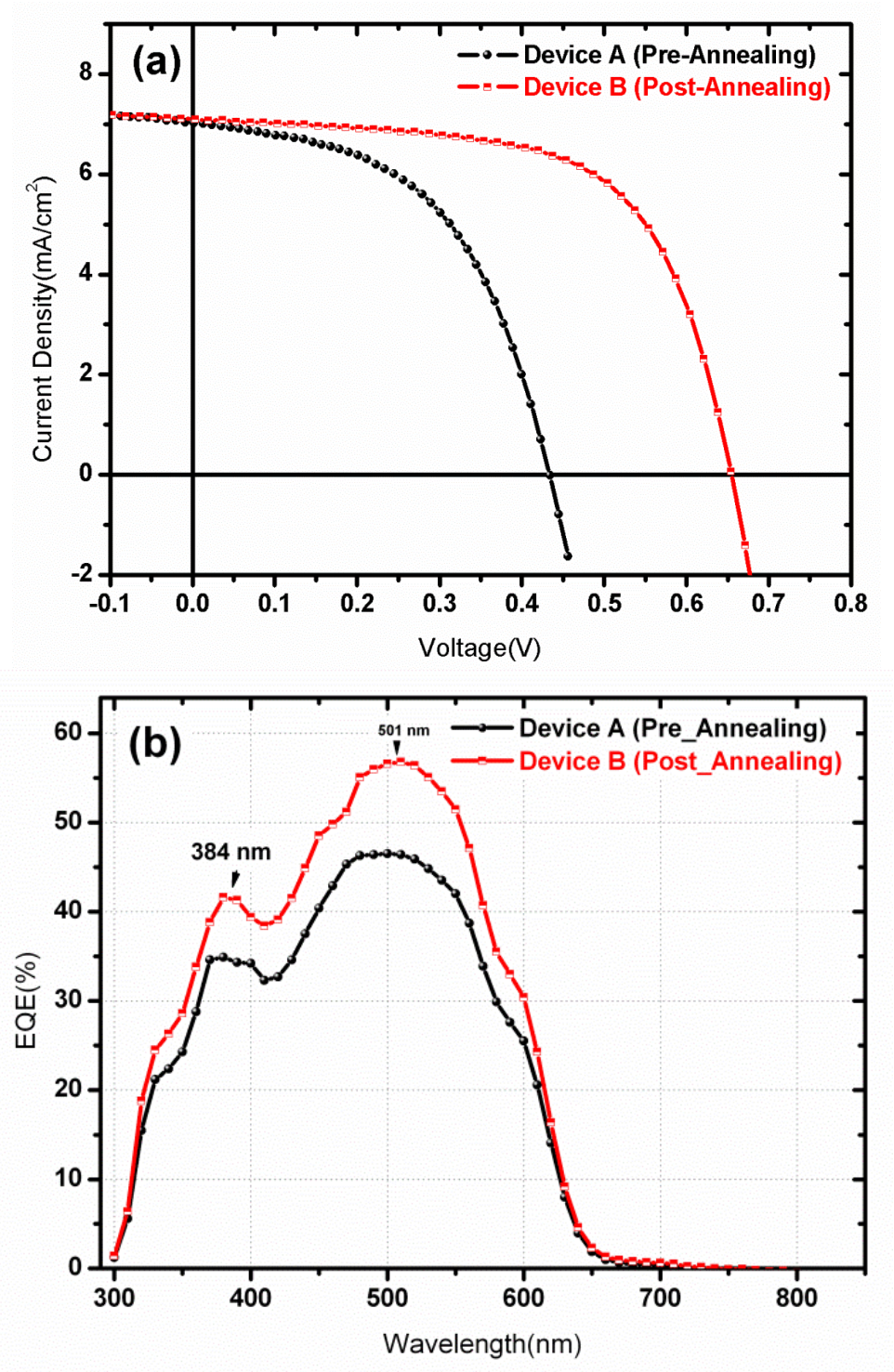

Figure 7.1: (a) J-V characteristics and (b) External quantum efficiencies of the devices

Table 7.1: Photovoltaic comparison of device A and device B

Device A				Device B			
J_{sc} (mA/cm^2)	V_{oc} (V)	FF (%)	PCE (%)	J_{sc} (mA/cm^2)	V_{oc} (V)	FF (%)	PCE (%)
7.027.18	0.433	51.69	1.57	7.10	0.654	63.07	2.93

Positive mode, SIMS depth profiling results of device A and B are presented in figure 7.2 and 7.3. Signals arising from ^{27}Al, ^{16}O, ^{12}C, ^{32}S, ^{64}Zn, ^{28}Si, ^{120}Sn and ^{115}In ions allowed a clear identification of the Al/ZnO/P3HT:PCBM/PEDOT:PSS and ITO/glass layers, respectively. Although there is no significant difference of depth profile distribution between device A and B except slight concentration intensity of carbon, the formation of Aluminum oxide is possible and this has been reported before by Bulle-Lieuwma et al [9]. The Al signal that decreases slowly and diffuses in to the active layer (P3HT:PCBM) originates from the Al metal. The annealing of devices leads to a slight shift and diffusion of Al into to the active layer. The interface between Al and P3HT:PCBM is found to be oxygen-rich, as it is visible from the ^{16}O signal observed. Interestingly, within the active layer the ^{64}Zn signal which originates from ZnO layer is observed. Again the intensity of ^{16}O signal increases at the Al/P3HT:PCBM interface and significantly decreases within the active layer and then stays constant throughout to the ITO/glass substrate. The presence of ^{16}O is attributed to ZnO or the formation of aluminum oxide (or hydroxide) during Al evaporation as a result of a chemical reaction with the present residual gas (water) in the vacuum chamber [10, 11] and water that might be present on the sample surface. Sulfur (^{32}S) depth profile, which originates from P3HT, PSS and PEDOT and carbon (^{16}C) from P3HT:PCBM are stable at the Al region, and then simultaneously increases towards the P3HT:PCBM region. While ^{16}C is uniformly distributed within the active layer then significantly decreases towards the PEDOT:PSS layer, ^{32}S slightly increased, slowly decreased and then is uniformly distributed throughout the PEDOT:PSS layer then decreased towards the ITO/glass region.

The diffusion of tin (^{120}Sn) and indium (^{115}In) into the active layer from ITO/glass region has been recognized as one of the main factors that are detrimental to the lifetime of organic solar cells. The diffusion of ^{115}In and ^{120}Sn depends on the nature of the layers present. In the case of PCBM/PEDOT:PSS/ITO, ^{120}Sn and ^{115}In signals are found within the PEDOT:PSS until they reach the P3HT:PCBM/PEDOT:PSS interface, where signals drops. De Jong et al [12] showed with RBS technique that the diffusion of ^{115}In into the PEDOT:PSS layer strongly increases upon the exposure to air using the explanation that water present in the atmospheric air and taken up by the PEDOT:PSS liberates the acidic protons of PSS. Acidic etching then result in indium ions dissolving in the PEDOT:PSS. This may possibly cause in both indium and tin diffusing to the P3HT:PCBM layer. Because our samples were exposed to air and kept for few months without encapsulation or were kept at ambient laboratory conditions, findings in this study may be in accordance with the results of de jong et al [12]. The silicon (^{28}Si) signal originating from the underlying glass substrate used is low throughout the layers and increases at the ITO/glass region.

Negative mode, SIMS measurements are shown in figure 7.4. C_4HS^- and SO_2^- ions originating from P3HT and PEDOT:PSS were detected. The depth profile distribution followed the same pattern as the ones presented in figure 7.2 and 7.3. $C_2O_3H_3^-$, SO_2^-, C_4HS^-, $C_{11}H_{17}S^-$ and $C_8H_7SO_3^-$ were also detected not only in the PEDOT:PSS/ITO layers but also in the inner region of the P3HT:PCBM layer. These results suggest that the active layer region is P3HT and PSS enriched.

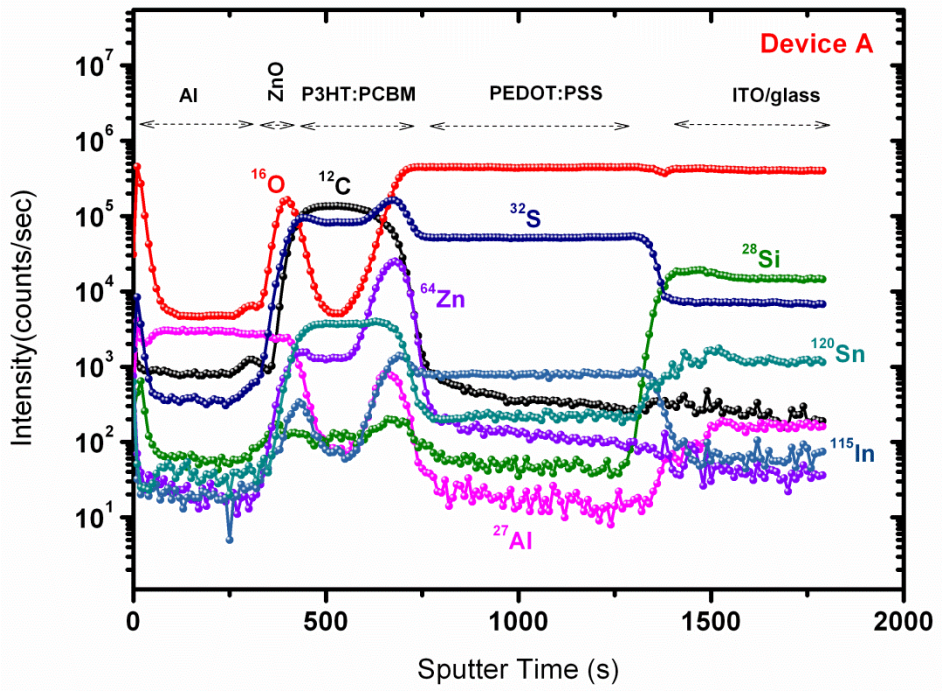

Figure 7.2: Positive mode TOF-SIMS depth profiles (Intensity as function of a sputter time) obtained directly on the Al cathode for the Pre-annealed device

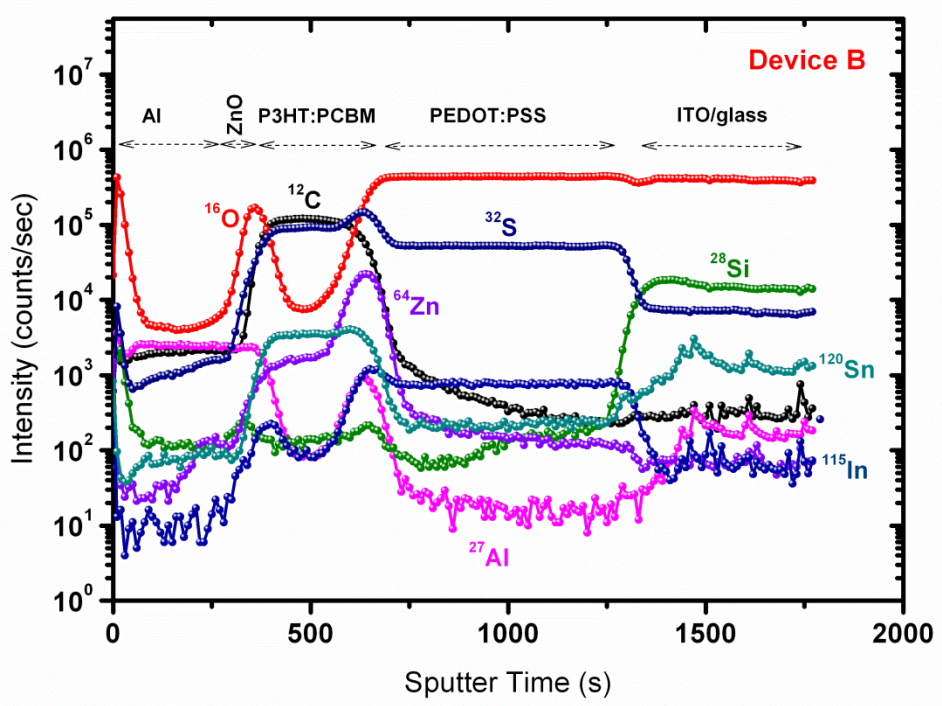

Figure 7.3: Positive mode, TOF-SIMS depth profiles (Intensity as function of a sputter time) obtained directly on the Al cathode for the Post-annealed device

.

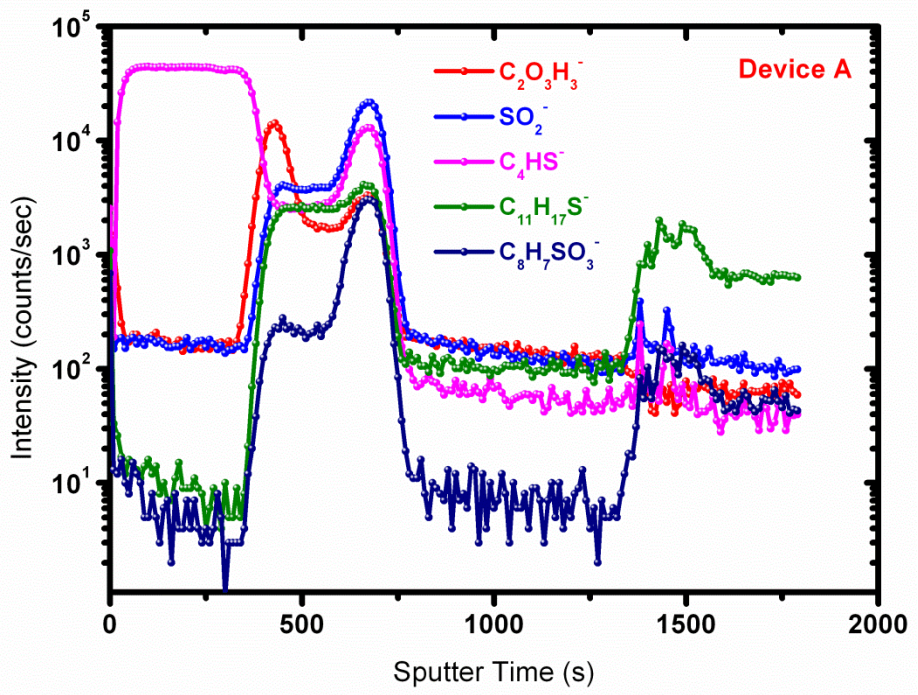

Figure 7.4: Composition depth profiles of secondary ions detected by Negative mode, TOF-SIMS

The secondary ion images for device A were detected using a low primary ion dose of 180 scans. The 3D imaging of positive and negative secondary ions is presented in figure 7.5 and 7.6, respectively. The distribution of signals shows high intensity/concentration for ^{16}O, ^{32}S while the intensity of ^{28}Si, ^{64}Zn and ^{12}C are relatively moderate. This observation is in correlation with the results observed in the depth profile shown in figure 7.3. Similar behavior is observed with the signals of $C_{11}H_{17}S^-$ and C_4HS^- showing most intense distribution as compared to SO_2^-, $C2H3O_3^-$ and $C_8H_7SO_3^-$. Their respective overlay images are also shown. However, due to their low concentration on the surface, ^{120}Sn and ^{115}In shows poor quality of surface imaging, hence they couldn't be included in this section. But with longer TOF-SIMS acquisition times and more computer processing it could be possible to increase the exposure to primary ions and increased concentration of these ions could be detected.

Figure 7.7 and 7.8 shows the surface imaging of device A after 60 and 180 primary ion scans, respectively. Images shows the specific elemental or chemical distribution across the surface observed within 300 μm × 300 μm dimension. These images reveal the secondary ion intensities as a function of the location on the sample surface. After the first 60 scans, ^{27}Al, ^{120}Sn, ^{64}Zn and ^{115}In are homogenously distributed on the sample surface while there are clear large particles on the surface indicating the inhomogeneous distribution of ^{16}O, ^{32}S, ^{12}C and ^{28}Si. However, after 180 scans the distribution of secondary ions detected intensified and showed more inhomogeneity across the surface.

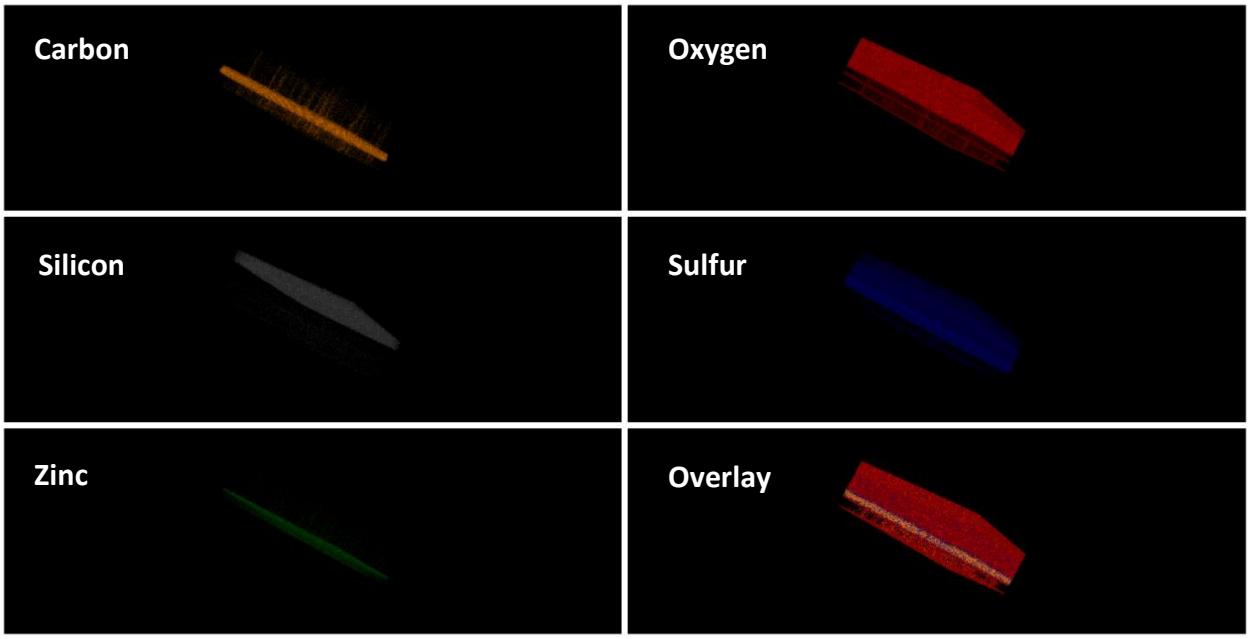

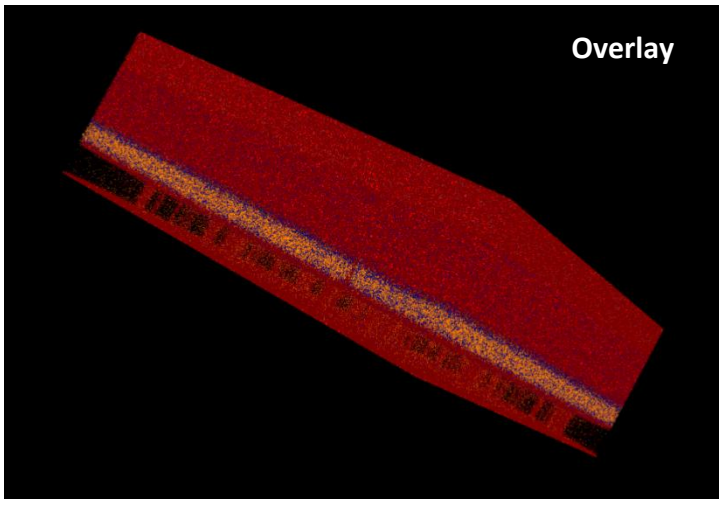

Figure 7.5: Positive ions, 3D elemental mapping for device A, after 180 scans (300 μm × 300 μm dimension).

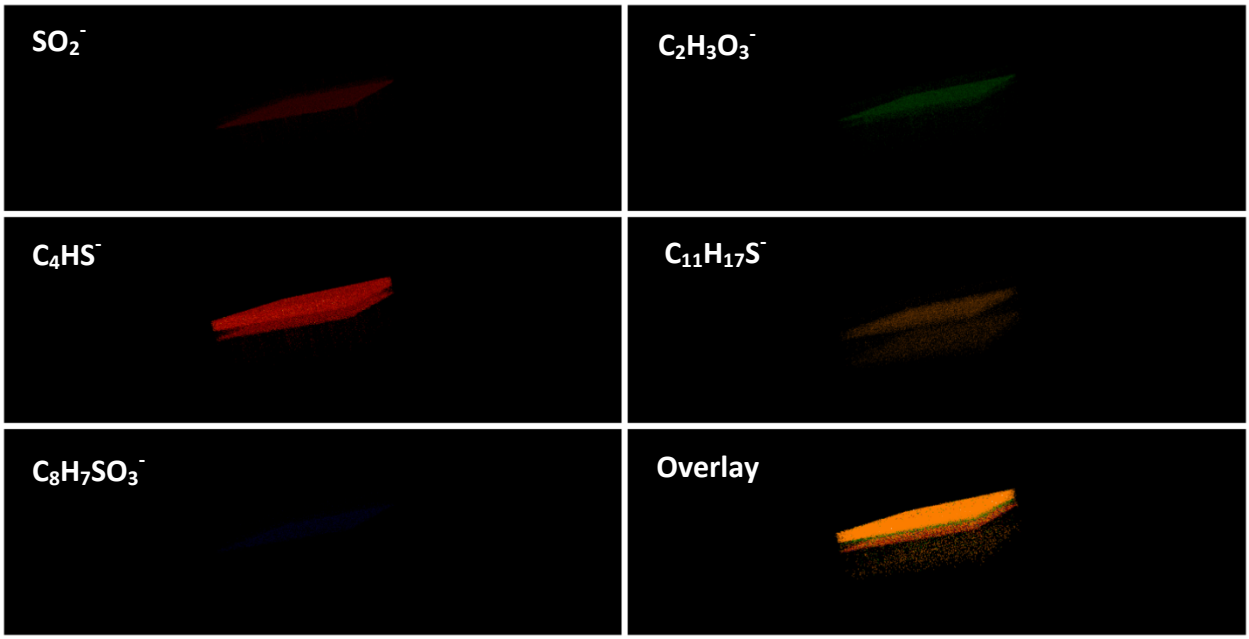

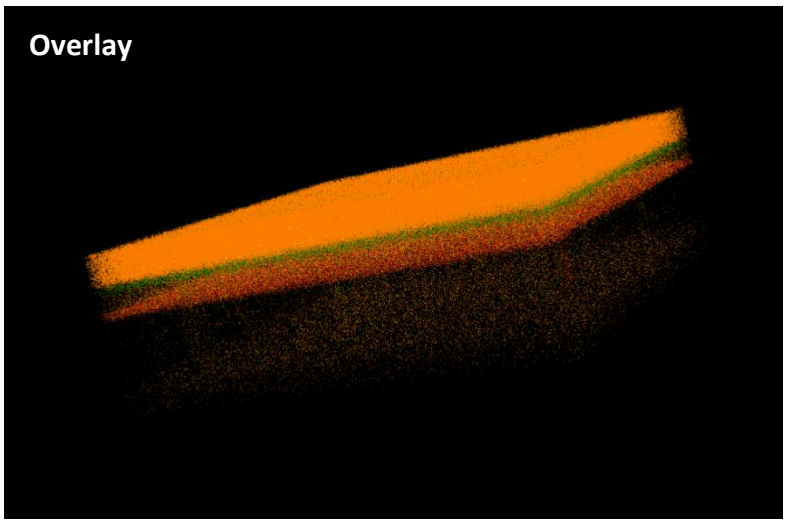

Figure 7.6: Negative ions, 3D elemental mapping for device A, after 180 scans (300 μm × 300 μm dimension).

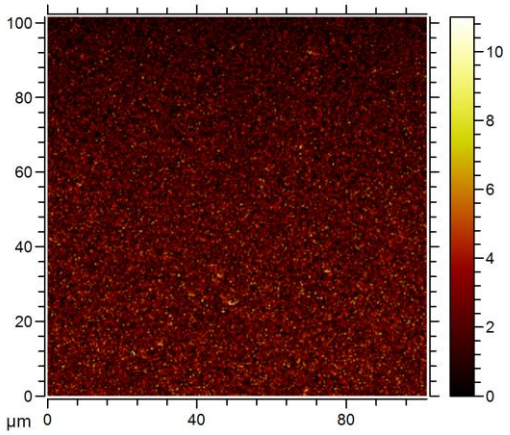

Al-
MC: 11; TC: 1.185e+005

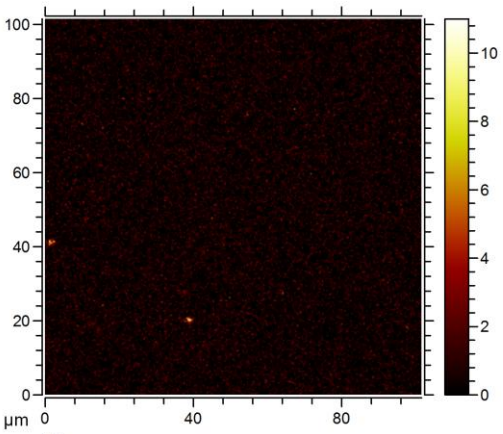

Zn-
MC: 11; TC: 3.047e+004

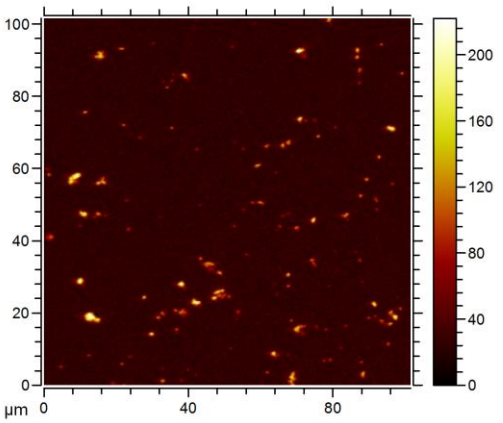

O-
MC: 222; TC: 1.684e+006

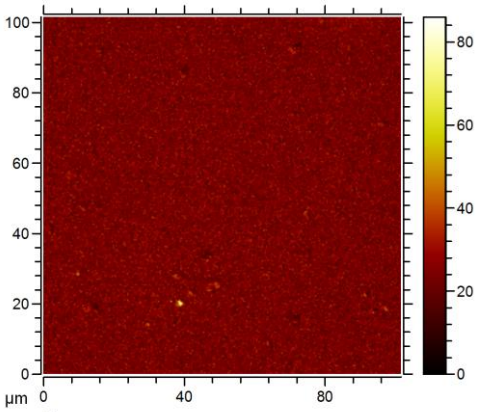

S-
MC: 86; TC: 1.543e+006

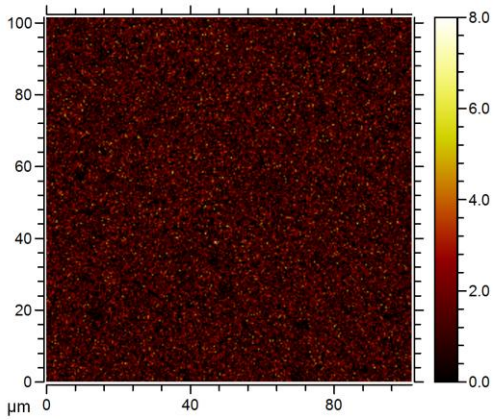

Sn-
MC: 8; TC: 6.610e+004

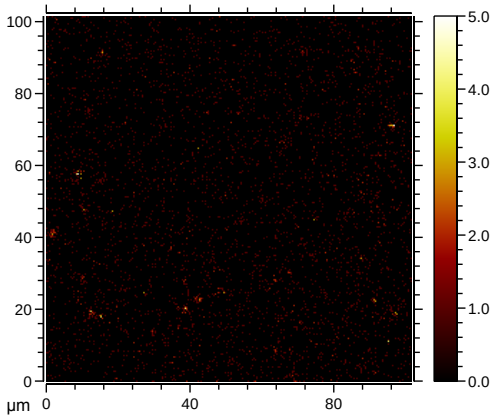

In-
MC: 5; TC: 4.279e+003

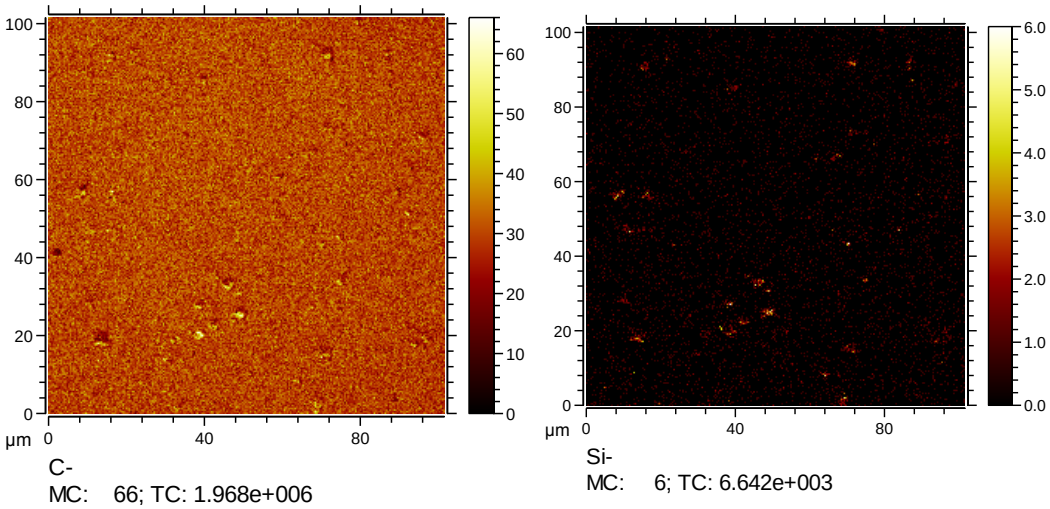

Figure 7.7: Elemental mapping for Device A, after 60 scans.

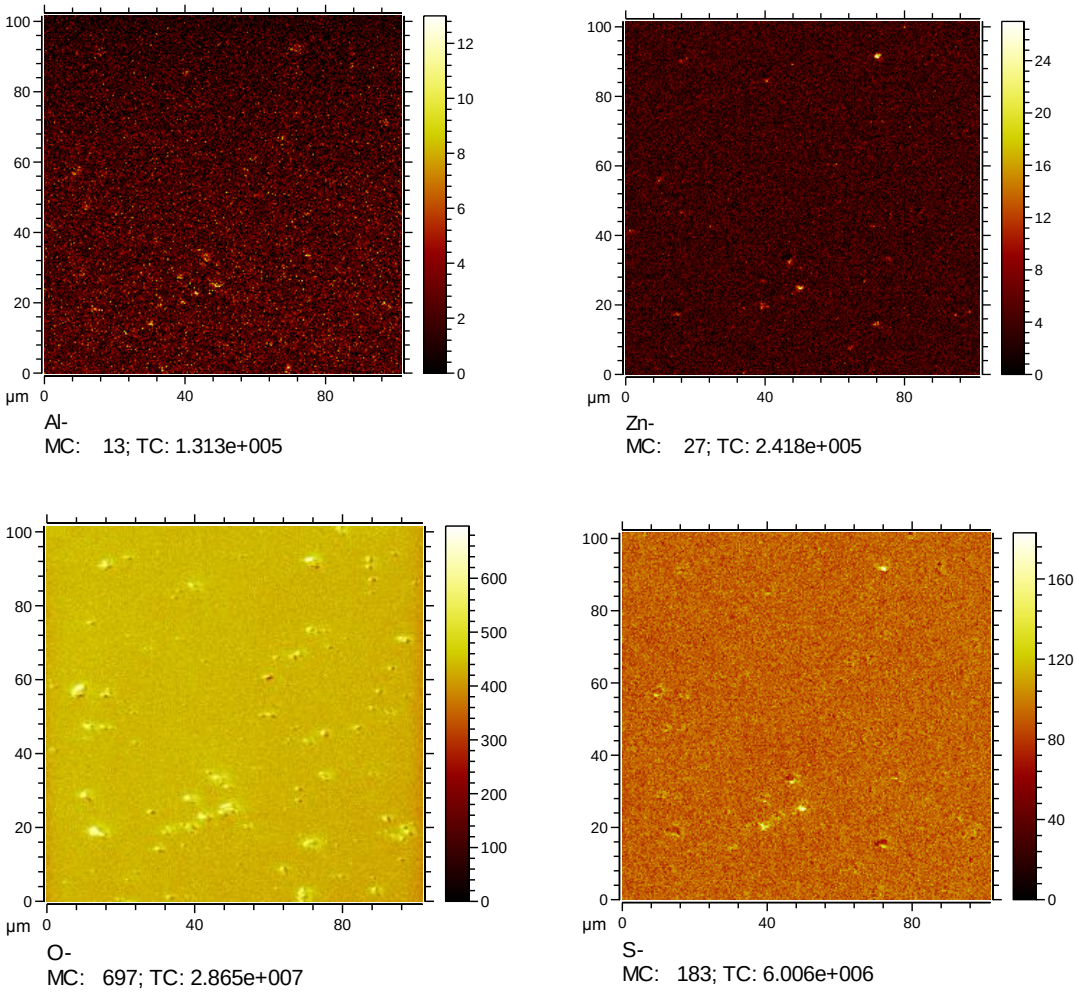

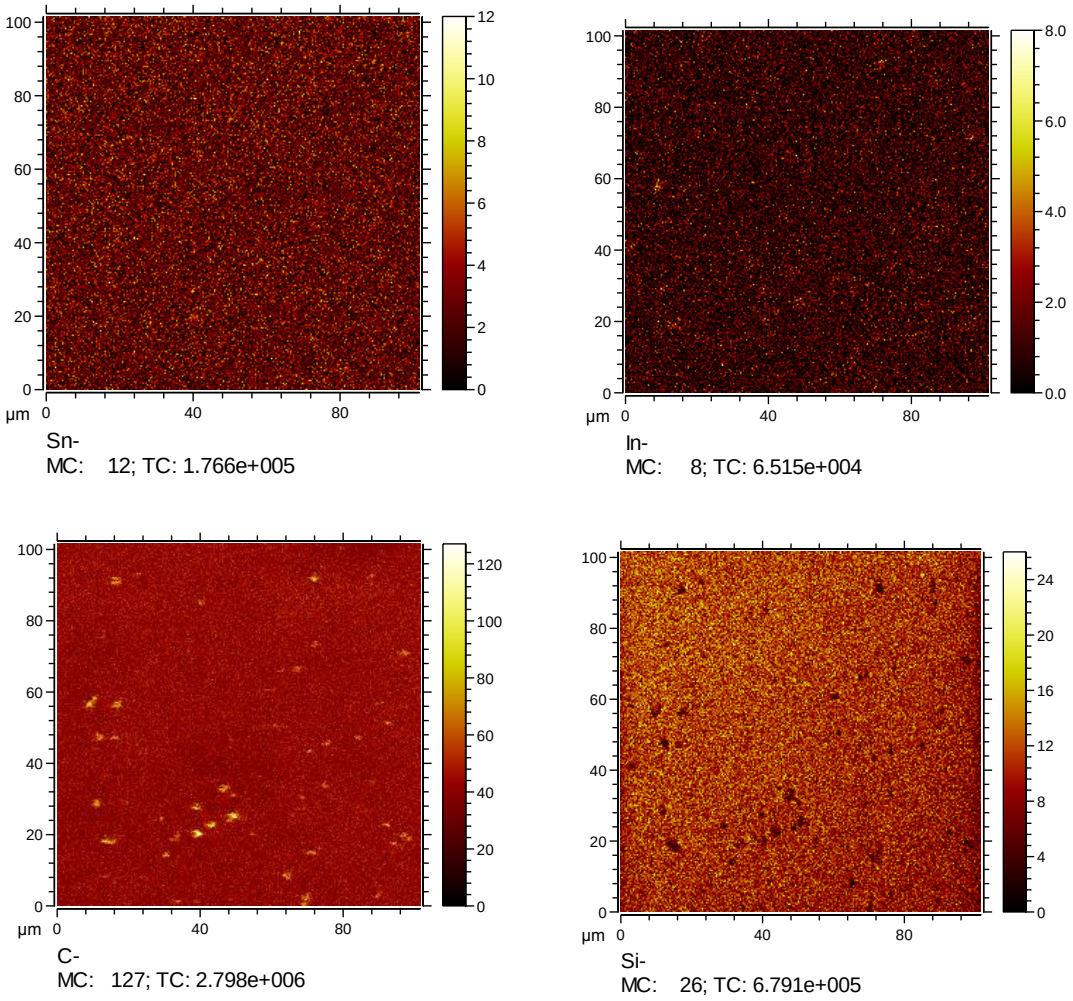

Figure 7.8: Elemental mapping for Device A, after 180 scans 300 µm × 300 µm dimension).

7.4. Conclusion

For a better understanding of how to improve photovoltaic properties of organic solar cells, we have studied the effect of thermal treatment before and after the deposition of Al electrode. The improvement in photovoltaic properties was observed from the post annealed device (device B) and this is attributed to the combined effects of the ZnO buffer layer and post annealing treatment. We carried out the composition depth profile analysis of the organic solar cells. The results indicated that the BHJ layer was P3HT enriched and PSS penetrated into the BHJ layer. The interface between Al and P3HT:PCBM was found to be oxygen-rich and species like AlO or AlO_2 may have formed at the interface. This was supported by a clear increase in intensity of the ^{16}O signal. Surface imaging showed homogeneity and some inhomogeneity distribution of chemicals.

References

[1] L.Chang, H.W.A Lademann, J-B Bonekamp, K.Meerholz and A..J Moule, *Advanced Functional Materials* **21**(2011) 1779-1787

[2] C. F Zhang, Y. Hao, S.W Tong, Z.H Lin, Q. Feng, E.T Kang, and C.X Zhu, *IEEE Transaction on Electron Devices*, **58** (2011) 835-842

[3] G. G. Andersson, W. J. H. van Gennip, J. W. Niemantsverdriet, H. H. Brongersma, *Chemical Physics* **278** (2002). 159-167

[4] M. A. Baldo and S. R. Forrest, *Physical Review B* **64**, (2001) 085201-1-085201-17

[5] B. Masenelli, E. Tutis, M. N. Bussac, L. Zuppiroli, *Synthetic Metals* **122** (2001)141-144

[6] O.M Ntwaeborwa, R. Zhou, L. Qian, S.S Pitale, J. Xue, H.C Swart and P.H Holloway, *Physica B:Condensed matter*, **407**(2012)1631-1633

[7] H.J Kim, J.H Park, H.H Lee, D.R Lee and J.J Kim, *Organic Electronics* **10** (2009) 1505-1510

[8] Y. Zhao, Z. Xie, Y. Qu, Y. Geng and L.Wang, *Synthetic Metals* **158** (2008) 908-911

[9] C.W.T Bulle-Lieuwma, W.J.H Van Gennip, J.K.J VanDuren, P.Jonkheijm, R.A.J Janssen and J. W. Niemantsverdriet, *Applied Surface Science* **203-204** (2003) 547-550

[10] H. Heil, J. Steiger, S. Karg, M. Gastel, H. Ortner, H. von Seggern, M. Stössel, *Journal of Applied Physics* **89**(2001) 420-424

[11] R.I.R. Blyth, S.A. Sardar, F.P. Netzer, M.G. Ramsey, *Applied Physics Letter* **77**(2000) 1212-1214

[12] M.P de jong, L.J van Ijzendoorn and M.J.A de Voigt, *Applied Physics Letters* **77**(2000) 2255-2257

8 Inverted organic solar cells with solution processed ZnO nanoparticles/nanoflowers

In this chapter photovoltaic property of inverted polymer: fullerene organic solar cells with solution processed zinc oxide (ZnO) nanoparticles and nanoflowers as electron extraction layers are compared. The devices comprised of the following configuration: glass/ITO/ZnO nanoparticles or nanoflowers/P3HT:PCBM/PEDOT:PSS/Ag. The maximum current density of 8.33 mA/cm^2 and 2.26 % power conversion efficiency was obtained from the device with ZnO nanoparticles as compared to 7.37 mA/cm2 and 1.08 % from device with ZnO nanoflowers. The improved performance of the device with ZnO nanoparticles is due to combined effects of improvement in charge collection and higher optical transmittance of electron selective layers. Furthermore, the depth profiling and surface imaging studies of the devices with nanoparticles extraction layer are discussed.

8.1. Introduction

In the conventional structure of organic solar cells, a layer of poly(3,4-ethylene dioxythiophene): poly(styrene sulfonate) (PEDOT:PSS) is usually used to modify the transparent indium tin oxide (ITO) electrode for efficient collection of holes [1,2]. However, owing to the strong acidic nature of PEDOT:PSS, the degradation of ITO/PEDOT:PSS interface is inevitable [3]. Furthermore, widely used low work-function metal cathodes such as Al cathode in conventional organic solar cells are sensitive to air. The exposure of an Al cathode to air can cause oxidation and degradation of the active layer due to the diffusion of oxygen and moisture through pinholes and grain boundaries of the metal cathode [4]. To overcome these problems, one approach is to use an inverted structure. By modifying the polarity of ITO with an n-type functional buffer layer and using less air sensitive, high work-function metals such as Ag or Au, collection of electrons and holes can be improved considerably. In this type of structure, the elimination of PEDOT:PSS and prevention of air and moisture diffusion from the high work-function metal top electrode can improve the device stability [5]. In organic solar cells, it is important to determine the appropriate energy level of the collecting electrode to match that of the active layer. Thus,

various materials for modifying the polarity of ITO have been proposed. Inorganic semiconducting materials such as TiO_2 or ZnO deposited on the ITO electrode can be used as buffer layers for accepting electrons which can also increase the stability of inverted organic solar cells [5,6]. Compared with TiO_2, ZnO have high electron mobility, which makes it an ideal electron selective contact layer in inverted organic solar cells structures [7]. In addition, TOF-SIMS measurements are performed to monitor 3D molecular compositions and metal/organic interface. The results are discussed in this chapter.

8.2. Experimental

ZnO nanoparticles/nanoflowers synthesis

A wet chemistry method was used to synthesize ZnO nanoparticles and nanoflowers. The synthesis details are discussed in chapter 4, section 4.4.

Device fabrication

The inverted devices with the device area of 0.12 cm^2 were fabricated. The ZnO layer from ethanol solution was spin coated at 4000 rpm for 35 sec on top of ITO/glass substrate and was dried on a hot plate at 60 ^oC for 1 hour. The photoactive layer of P3HT:PCBM blend with a weight ratio of 1:0.6, dissolved in chlorobenzene, was spin-coated with the speed of 1000 rpm for 15 sec followed by PEDOT:PSS layer. The next step was to evaporate the ~ 100 nm silver (Ag) metal electrode at ~ 1×10^{-6} Torr and the cells were annealed at 155 ^oC for 10 min.

Characterization

The structure of ZnO nanoparticles and nanoflowers was analyzed by X-ray diffratometer (XRD), the transmittance of ZnO films were evaluated using a Perkin – Elmer Lambda 35 UV-Vis-NIR spectrophotometer and cross-section view morphology was evaluated by field-emission scanning electron microscopy (FE-SEM). The current-density versus voltage (J-V) characteristics and external quantum efficiencies were measured as discussed in Chapter 7, section 7.2.

Same procedure and settings discussed in Chapter 7, section 7.2 were used to do the analysis of depth profiling and surface imaging on the inverted organic solar cells.

8.3. Results and discussion

The hexagonal wurtzite structure of both ZnO nanoparticles and nanoflowers was measured using XRD by a CuKα source with 2θ ranging from 30^o to 80^o as shown in figure 8.1. The particle size as discussed in previous chapters was estimated using the Debye-Scherrer equation, and was found to be ~ 5 nm for nanoparticles and ~ 35 nm for clustered nanoflowers. The broadening of the peaks reveals the nanocrystalline nature of ZnO nanoparticles. The XRD peaks matched well with the standard JCPDS data, card no 80-0075. The optical transmittance spectra of ZnO nanoparticles and nanoflowers films are presented in figure 8.2. In two cases the films were found to be highly transparent (over 99 % transmittance) in the visible range with absorption edges around 251 nm (nanoparticles and nanoflowers) and 348 nm (nanoparticles only). However the low transmittance is observed for ZnO nanoparticle at the wavelength range of 200 nm – 500 nm as compared to the transmittance of ZnO nanoflowers. Figure 8.3 show the cross-sectional view of ZnO nanoparticles and nanoflowers on the ITO-coated glass substrate. The nanoparticles are uniformly distributed across the surface while the nanoflowers were scattered unevenly on the surface.

Photovoltaic (PV) characteristics comparison between the device with ZnO nanoparticles and nanoflowers are shown in figure 8.4 (a-b) and extracted parameters are summarized in table 8.1. The device with ZnO nanoparticles shows a J_{sc} of 8.33mA/cm^2, V_{oc} of 0.58 V and FF of 46.45 %, resulting in the PCE of 2.26 %. However, as shown in table 8.1, the PV values of from the device with ZnO nanoflowers were comparatively low. It is evident from the J-V curve that the device with nanoflowers suffers the high series resistance. Since these devices are fabricated with the same materials and the same procedure and the only difference is the electron extraction layer morphology, the increased current density is unlikely to account for other reasons, but it is possibly due to reduced series resistance in the case of ZnO nanoparticles. Shim et al [9], have demonstrated that the tuning of ZnO buffer layer improves the photovoltaic performance. On the other hand when the ZnO buffer layer becomes thick, a high intrinsic resistance increasing the

series resistance and reducing the charge carrier transport ability can decrease the photovoltaic performance of the device.

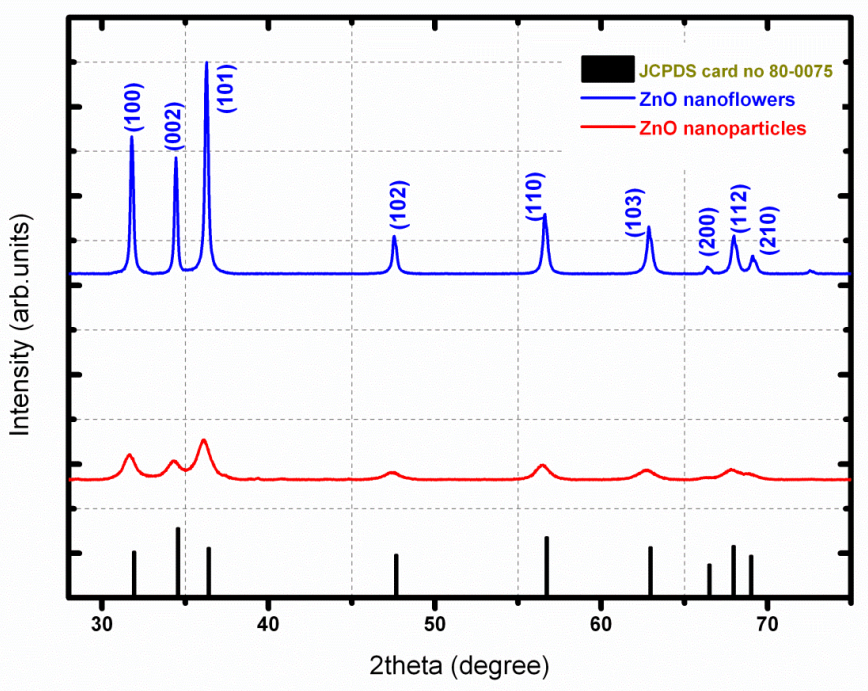

Figure 8.1: XRD patterns of ZnO nanoparticles and nanoflowers.

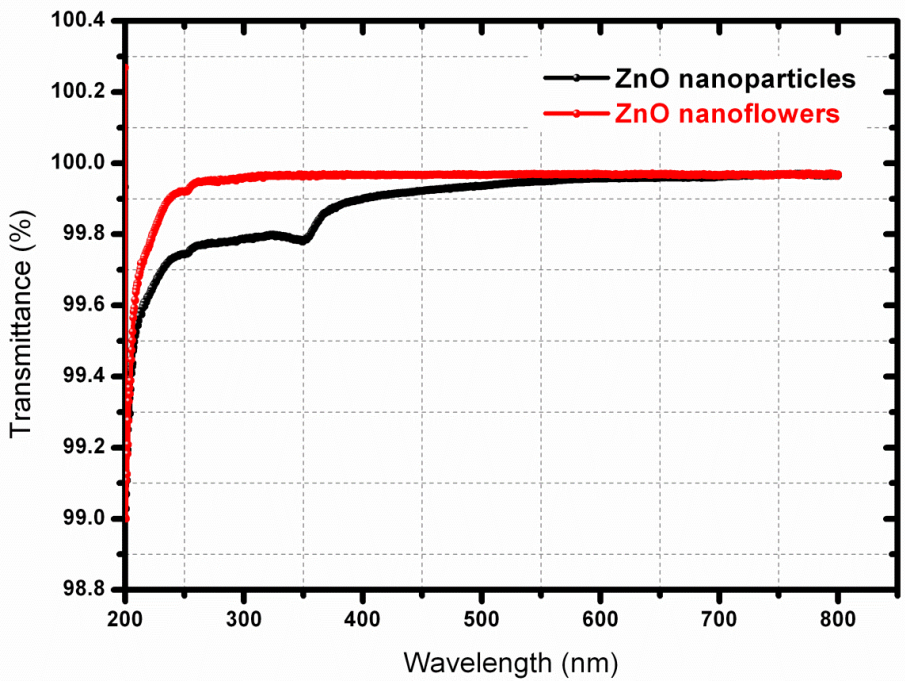

Figure 8.2: Transmittance comparison of ZnO nanoparticles and nanoflowers.

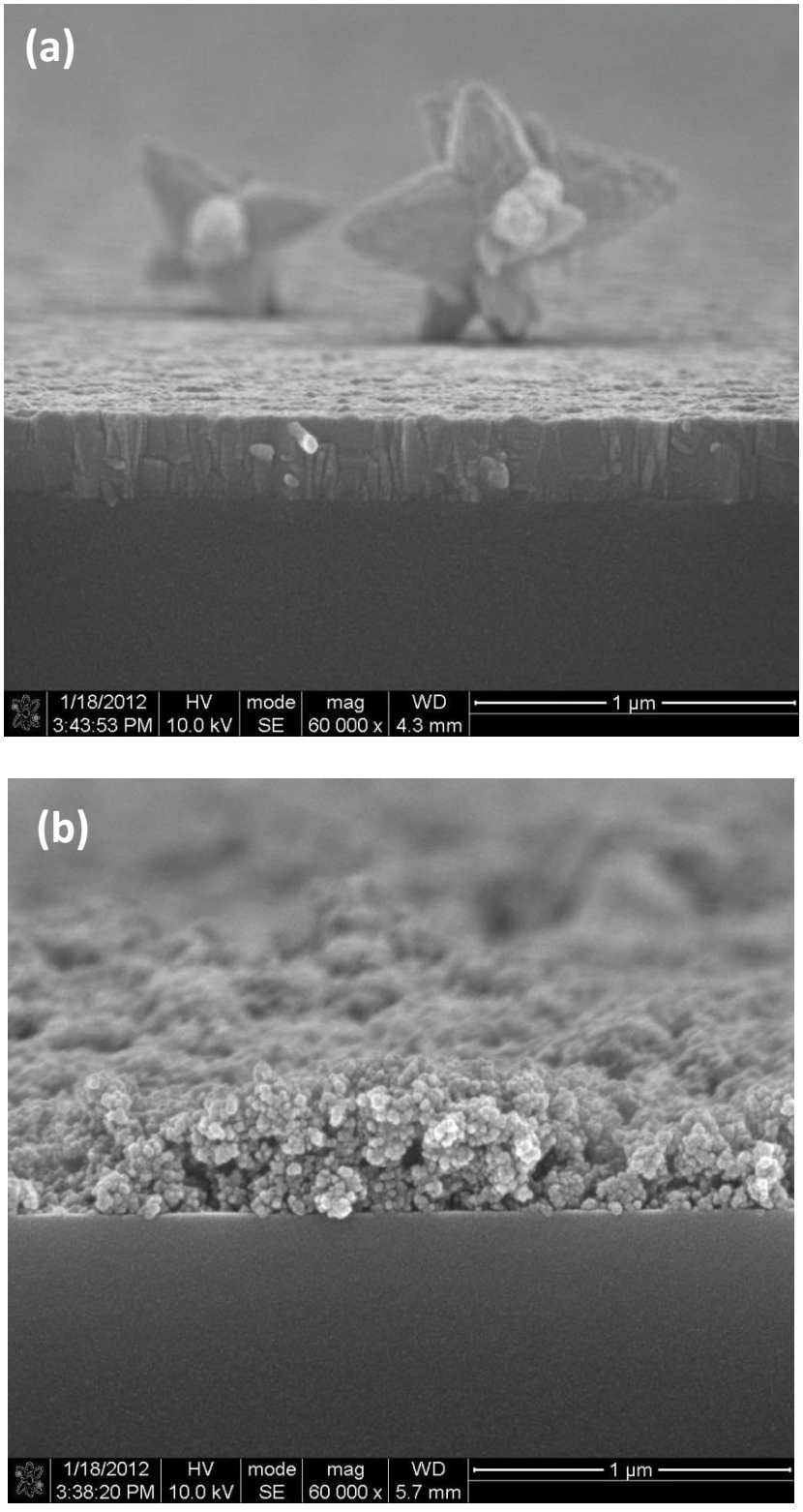

Figure 8.3: FE-SEM cross-section view of (a) ZnO nanoflowers on a glass/ITO substrate and (b) ZnO nanoparticles on a glass substrate.

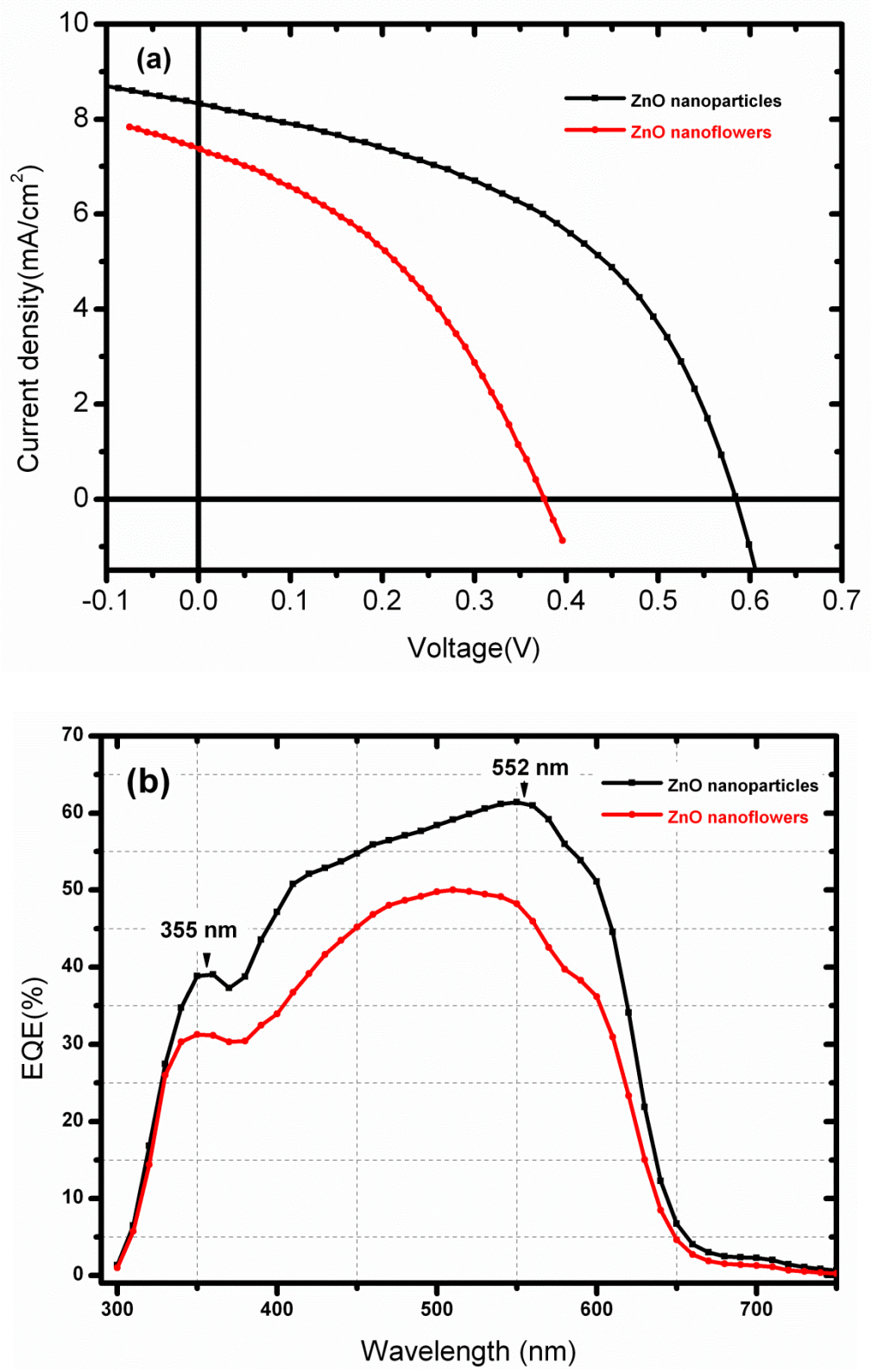

Figure 8.4: (a) J-V characteristics and (b) External quantum efficiencies of the devices with ZnO nanoparticles and nanoflowers electron selective layers.

Table 8.1: Photovoltaic comparison of P3HT:PCBM solar cells with ZnO nanoparticles and nanoflowers electron selective layers

Inverted Device	ZnO Layer	J_{sc}(mA/cm^2)	V_{oc}(V)	FF(%)	PCE(%)
(1)	Nanoparticles	8.331	0.5848	46.45	2.26
(2)	Nanoflowers	7.379	0.3763	38.81	1.08

The external quantum efficiencies (EQE) of these two devices are compared in figure 8.4(b). The device with the ZnO nanoparticles clearly has a higher EQE, especially for wavelengths longer than ~ 450 nm. The EQE of the device with ZnO nanoparticles exceeds that of the nanoflowers by approximately 10 %. A slight red-hift of spectrum is also observed. The enhanced or red-shift is believed to be the result of improved polymer chain ordering from the growth process [8]. The negative and positive mode, SIMS depth profile was performed on the device with ZnO nanoparticles to determine the distribution in depth of the device components. This is presented in figure 8.5 (a-b). The peak intensity of ^{107}Ag signal remained constant for the first few minutes and then decreased. The profile pattern indicated the moderate diffusion of ^{107}Ag into the P3HT:PCBM region. ^{64}Zn, ^{12}C and ^{16}O signals simultaneously increased as the ^{107}Ag signals decreases. They all remain constant in the P3HT:PCBM region except for the ^{16}O signal which dropped and increased again towards the P3HT:PCBM/PEDOT:PSS interface. This suggests that the surface is oxygen rich towards the ZnO/ITO/glass region. In addition, ^{32}S signal also increases and remains constant through the P3HT:PCBM/DEDOT:PSS regions and it drops at the ITO/glass region, indicating that these regions are sulfur enriched originating from both P3HT and PSS. As indicated in the previous discussion (Chapter 7), ^{120}Sn and ^{115}In signals are observed in the P3HT:PCBM region and this is attributed to the acidic nature of PEDOT:PSS etching away the organic layers thereby allowing the penetration of ^{120}Sn/^{115}In into other layers. The ^{28}Si signal which is pronounced in the ITO/glass region comes from the glass substrate.

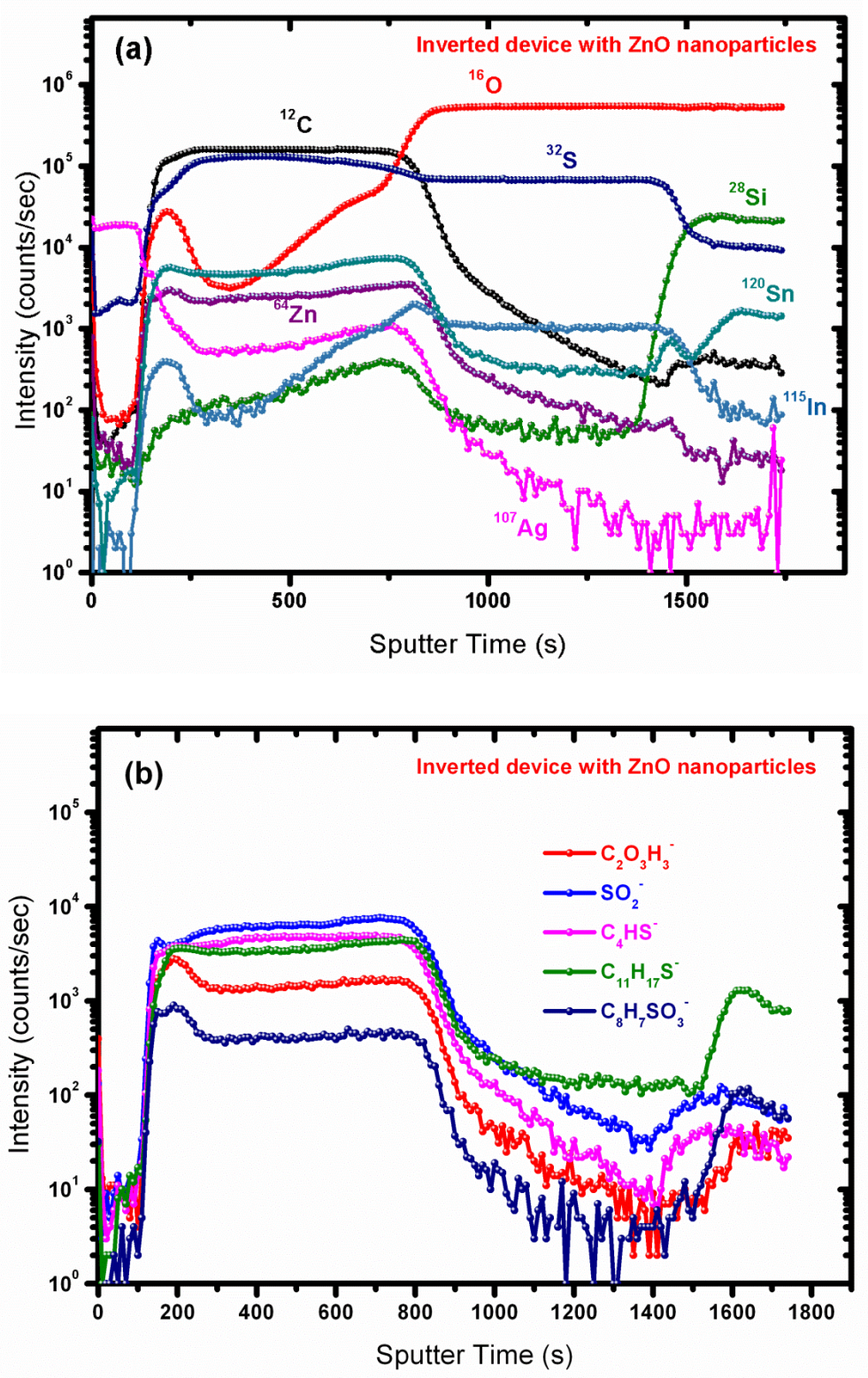

Figure 8.5: (a-b) TOF-SIMS depth profiles (Intensity as function of a sputter time) obtained directly on the Ag electrode for the inverted device with ZnO nanoparticles

Profiles of secondary ions originating from P3HT, PSS and PCBM are shown in Figure 8.5 (b), which quantitatively shows $C_2O_3H_3^-$, SO_2^-, $C_4H_5^-$, $C_{11}H_{17}S^-$ and $C_8H_7SO_3^-$ .It is clear that these secondary ions populated the active layer and this suggests that this region is P3HT:PCBM and PSS enriched as expected because the active layer is comprised of P3HT:PCBM blend. Figure 8.6 (a-d) shows the 3D surface images of silver, carbon, oxygen and sulfur. It is evident from the images that there is quite a high concentration of ^{12}C, ^{16}O and ^{32}S. This is consistent with the composition depth distribution presented in figure 8.5(a).

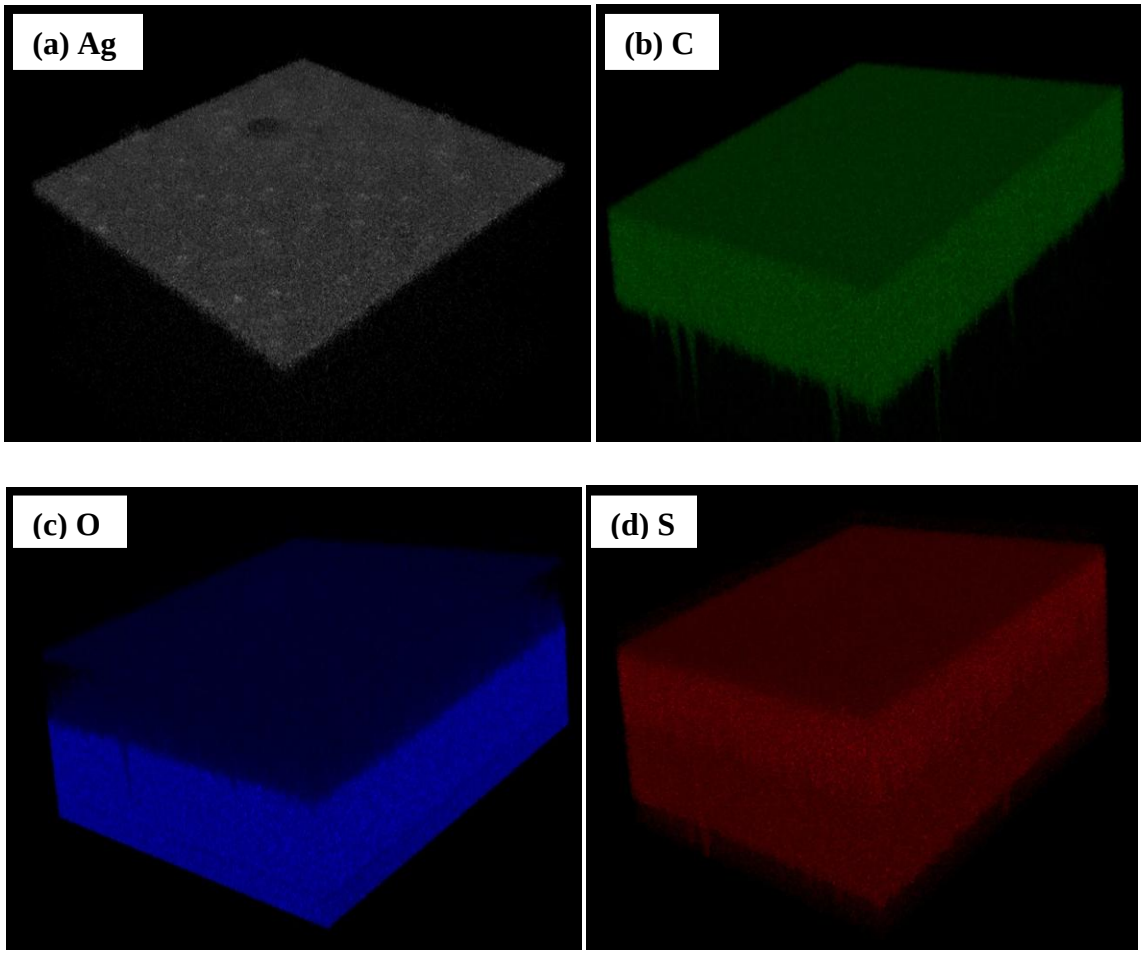

Figure 8.6: 3-D surface imaging of (a) Silver, (b) Carbon, (c) Oxygen and (d) Sulfur (300 μm × 300 μm dimension)

8.4. Conclusion

In conclusion, the photovoltaic properties of inverted organic solar cells with ZnO nanoparticles/nanoflowers electron extraction layers were compared. We found that the morphology of ZnO had an impact on the performance of organic solar cells and the higher PCE of 2.26 % was obtained from the device with ZnO nanoparticles electron extraction layer. The improvement in photovoltaic response was attributed to the blocking of holes and an enhanced electron collection of electrons to the ITO electrode. In addition, the TOF-SIMS results of the device with ZnO nanoparticle extraction layer revealed a small but non-negligible ^{107}Ag and ^{64}Zn diffusion into the active layer as well as prominent ^{32}S and ^{12}C signals coming from P3HT and PCBM, respectively. Furthermore, SIMS imaging confirms the high concentrations of ^{16}O, ^{32}S and ^{12}C signals in the depth distribution.

References

[1] J.Y. Kim, K. Lee, N.E. Coates, D. Moses, T.Q. Nguyen, M. Dante and A.J. Heeger, *Science* **317**(2007)222-225

[2] W.Ma, C. Yang, X. Gong, K. Lee and A.J. Heeger, *Advanced Functional Materials* **15**(2005)1617-1622

[3] K.W. Wong, H.L. Yip, Y. Luo, K.Y. Wong, W.M. Lau, K.H. Low, H.F. Chow, Z.Q. Gao, W.L. Yeung and C.C Chang, *Applied Physics Letters* **80**(2002)2788-2790

[4] J.C Wang, W.T. Weng, M.Y. Tsai, M.K. Lee, S.F. Horng, T.P Perng, C.C. Yu and H.F. Meng, *Journal of Materials Chemistry* **20**(2010) 862-866

[5] F.C Krebs, S.A. Gevorgyan and J. Alstrup, *Journal of Materials Chemistry* **19**(2009)5442-5451

[6] C.Y. Li, T.C. Wen, T.H. Lee, T.F. Guo, J.C.A. Huang, Y.C. Lin and Y.J Hsu, *Journal of Materials Chemistry* **19**(2009)1643-1647

[7] S.K. Hau, H.L. Yip, N.S. Baek, J.Zou, K.O'Malley and A.K.Y. Jen, *Applied Physics Letters* **92**(2008)253301-1-253301-3

[8] V. Shrotriya, G. Li, Y.Yao, T. Moriarty, K. Emery and Y. Yang, *Advanced Functional Materials* **16**(2006) 2016-2023

[9] W. H. Shim, M. Y. Park, D. S. Park, Y. T. Kim, S. Y. Park, J.-H. Lim, K. H. Lee, Y. S. Jeong, Y. D. Kim, K.-D. Kim, H. O. Seo, Y. D. Kim and D. C.Lim, *Molecular Crystals and Liquid Crystals* **538**(2011)164-170

9 Summary and Conclusion

This chapter presents summary and concluding remarks on the previous chapters. Also some possible future work that could be done to continue the research on P3HT:PCBM based solar cells is discussed.

9.1. Summary

9.1.1. ZnO nanostructures in OSCs as electron extraction layers

ZnO nanoparticles, nanoflakes and nanoflowers synthesized by wet chemistry method were used in organic solar cells as electron extracting layers (chapter 4). The hexagonal wurtzite structure of ZnO particles was observed and crystallite size was estimated using Debye-Scherrer equation. ZnO nanoparticles were found to be ~5 ± 0.2, nanoflakes ~20 ± 0.2 and nanoflowers ~35 ± 0.2. FE-SEM revealed spherical ZnO nanoparticles, randomly oriented nanoflakes and clustered nanoflowers and TEM revealed agglomerated nanoparticles with the diameter of ~5 nm, this is in agreement with the XRD results. In addition, rods clustering into flower-like structures were also crystallized. ZnO nanostructures exhibit two absorption peaks at ~ 251 nm and ~ 348 nm (for nanoparticles only). The major absorption peak at 348 nm represents intrinsic band gap absorption of ZnO. The peak at 251 nm was attributed to structural defects. The direct band gap of ZnO nanoparticles was estimated using Tauc's relation and was found to be ~ 3.34 eV. We could not estimate the band gap of nanoflakes and nanoflowers using Tauc's relation because the excitonic band was completely flattened.

9.1.2. Effects of processing parameters on the performance of OSCs

The conventional and inverted organic solar cells were successfully fabricated and processing parameters were varied to determine the optimum performance of conventional devices (chapter 5). Chlorobenzene and 1,2-dichlorobenzene were used to dissolve the photo-active materials (P3HT:PCBM blend). The photovoltaic response was relatively higher when chlorobenzene was

used as a solvent with the PCE of 2.94 % versus 2.86 % when using 1,2-dichorobenzene. This is attributed to the higher carrier mobility and charge collection to the respective electrodes. Again, significant improvement of photocurrent was observed when varying the molecular weight ratio of P3HT:PCBM blend. The maximum PCE of 2.45%, FF of 54.95, J_{sc} of 7.14 mA/cm^2 and V_{oc} of 0.62 V were observed with the weight ratio of 1:0.6 chlorobenzene was used as a solvent of the blend.. The vastly improved performance of the device cast from chlorobenzene with 1:0.6 weight ratio was attributed to factors like the length scale of phase segregation which maybe the same order of magnitude as the exciton diffusion length.

9.1.3. Effects of particle morphology on the performance of OSCs

The performance of both conventional and inverted devices was found to depend on the concentration and morphology of ZnO. In the conventional device, ZnO nanoparticles and nanoflakes concentrations were varied from 0.5 to 20 mg/mL (chapter 6). The surface topographic images of PEDOT:PSS, P3HT:PCBM, ZnO nanoparticle and nanoflakes and Al layers with rms roughness values of 1.02 ± 0.01 nm, 5.2 ± 0.2 nm, 52 ± 3.6 nm, 3.5 ± 0.5 nm and 58 ± 3.2 nm, respectively, were analyzed. The lower rms values shows the smoothening effect of layers while the broad hill-like layers with higher rms value were ascribed to annealing and the formation of highly ordered film structure. Although the devices had the same ZnO concentration, the device with ZnO nanoflakes recorded relatively higher values of PCE, J_{sc}, V_{oc} and FF. The highest PCE values of 2.37 % and 3.08 % were obtained from the devices spin-coated from the ZnO nanoparticles and nanoflakes solutions of 0.5 mg/mL concentration respectively. Furthermore, a comparison between the inverted devices with ZnO nanoparticles and nanoflowers as electron extraction layers was made (chapter 8). In this case, the devices were fabricated using the same materials and the same procedure except that the particle morphology of the ZnO electron extraction layer was different. The photovoltaic response was high for device with ZnO nanoparticles, even if the ZnO nanoflowers showed slightly higher transparency. The EQE of devices studied in this thesis mostly exhibits maximum photon absorption in the visible range of the spectrum in the range of 300-600 nm wavelength.

9.1.4. Effects of thermal treatment on the performance of OSCs

The general performance of devices was shown to depend on the sequence of thermal annealing. For example, the devices annealed after Al deposition showed better performance compared to the device annealed before the Al deposition (chapter 7). It is well known that annealing can improve the crystallinity of P3HT resulting in improved hole mobility in the P3HT. This self-aggregation is induced by the strong packing of hexyl side groups and thiophene rings, which enhances intra and inter molecular charge transfer. As a result, the R_s of OSC decreased and FF increased.

9.1.5. Surface characterization of OSCs

Compositional depth profiling and surface imaging of OSCs were discussed in chapters 7 and 8. For both conventional and inverted devices, different layers of the OSCs, namely, the Al/Ag, the P3HT:PCBM layer, the ZnO nanoparticles layer, PEDOT:PSS layer and ITO/glass layer were clearly identified by TOF-SIMS depth profiling. TOF-SIMS revealed signals arising from ^{27}Al, ^{16}O, ^{12}C, ^{32}S, ^{64}Zn, ^{28}Si, ^{120}Sn and ^{115}In ions. Enrichment of oxygen at the interface between Al and the photoactive layer was observed. Furthermore, depth-profiling showed that during preparation diffusion of indium into the PEDOT:PSS occurred and this was probably due to the influence of water molecules from the atmosphere.

9.2. Conclusion

In conclusion, the research conducted in this project has established new perspectives regarding the effects of ZnO particle morphology on the performance of organic solar cells. Combined with the recent advances in the efficiency of solar cells, the prospects for fabricating efficient organic solar cell devices using ZnO nanostructures as electron extracting layers are excellent. However, it should be noted that the reproducibility issue of OSCs has not yet been clearly addressed because of several reasons. Firstly, establishing highly reproducible performance of OSCs requires tremendous trial and errors, and poorly reproducible performance is believed to be an intrinsic drawback of organic electronics devices. Secondly, in the device fabrication, there are several process variables: blend solution preparation method, blend ratio, blend layer thickness, PEDOT:PSS thickness, various kinds of PEDOT:PSS with different conductivity, spin casting conditions, cathode structure, annealing conditions and method, oxygen and moisture

exposure, encapsulation, illumination set-up and characterization set-up. As a result, it is quite difficult to consistently reproduce the same or relative photovoltaic output from one device to the other. Therefore, many researchers experience significant performance variation even though the devices were fabricated using a consistent procedure. Finally, the results reported in this thesis indicated that more fundamental questions concerning the influence of ZnO morphology on the performance of organic solar cells must be addressed before rational improvement can be expected.

9.3. Future work

Organic solar cells offer many advantages due their fundamental properties, mechanical flexibility and resilience, light weight, processability and immense customizability in their optoeletronic characteristics. Efficiencies have improved considerably due to a greater understanding of basic organic semiconductor operations, tailored device architectures and improved material synthesis and selection, with current state-of-the-art device efficiencies exceeding 8%.

Despite advances, numerous challenges still remain to make OSCs a commercially viable competitor to thin film inorganic materials. To this point, most research efforts have been focused on increasing device efficiency at the laboratory scale and the lifetime of OSCs is also a concern and requires more investigation. In addition, as materials synthesis and control over device morphology improve, attention must be turned to module performance as a whole, including optical effects. Altering substrate optical properties has already been shown to improve the exciton diffusion bottleneck and increase performance and further developments could increase the performance further.

In the past three decades, organic photovoltaics have emerged from a niche research topic to a promising competitor in the photovoltaic market. Inexpensive, rugged, and high efficiency organic photovoltaics have the potential to revolutionize solar energy around the world and diligent research effort will realize this goal. Finally, the future work that can be done to continue the research of P3HT:PCBM based solar cells is to look into approaches of light harvesting by choosing low band gap photo-active materials and band gap tuning of conjugated polymers or extending to NIR to maximize the efficiency of OSCs. Moreover, ZnO has a lot of defects that

might cause instability in the devices. Treatment of ZnO in the UV-Ozone may get rid of some of these defects and significantly change the conductivity thereby enhancing the absorption efficiencies or the overall performance of OSCs.

Publications

P.S. Mbule, G.H. Mhlongo, H.C. Swart. O.M. Ntwaeaborwa, Sensitizing effect of ZnO quantum dots Red-emitting Pr3+-doped SiO2 Phosphor, Physica B: 407, (2012) 16071610

P.S. Mbule, G.H. Mhlongo, H.C. Swart, O.M. Ntwaeaborwa, Low temperature synthesis of ZnO nanoparticles and nanorods via wet chemistry route, proceedings of the South African Institute of Physics Conference, 12-15 July 2011, pp 174 - 178, ISBN 978-1-86888-688-3,

P.S. Mbule, T.-H. Kim, B.-S. Kim, H.C. Swart, O.M. Ntwaeaborwa, Effects of thickness and and solvent on the photo-active layer in organic photovoltaic devices, Submitted to the Journal of Physics Conference series

P.S. Mbule, T.-H. Kim, B.-S. Kim, H.C. Swart, O.M. Ntwaeaborwa, Effects of particle morphology of ZnO buffer layer on the performance of organic solar cell devices, solar energy materials and solar cells 112(2013), pp 6-12

National Conferences

- 55^{th} Annual Conference of the South African Institute of Physics (September 2010)

    1. Ex-Situ synthesis and optical properties of ZnO-PbS nanocomposite
       P.S. Mbule, R.E. Kroon, H.C. Swart and O.M. Ntwaeaborwa

- 4^{th} South African Conference on Photonic Materials (May 2011)

    2. Sensitizing effects of ZnO quantum dots on red-emitting Pr^{3+}-doped SiO_2 phosphor
       P.S. Mbule, G.H. Mhlongo, S.Pitale, H.C. Swart and O.M. Ntwaeaborwa

- 56^{th} Annual Conference of the South African Institute of Physics (July 2011)

    3. Low temperature synthesis of ZnO nanoparticles and nanorods via wet chemistry route
       P.S. Mbule, G.H. Mhlongo, H.C. Swart and O.M Ntwaeaborwa

- 57th Annual Conference of the South African Institute of Physics (July 2012)

    4. Thickness and Solvent influence on the photo-active layer in organic photovoltaic devices

       P.S Mbule, T.-H. Kim, B.-S. Kim, H.C. Swart and O.M. Ntwaeaborwa

International Conferences

- 4th International conference on Nanoscience and Nanotechnology (1-4 April 2012)

    5. Effects of ZnO nanoparticles/nanoflakes buffer layer on the performance of organic photovoltaic devices
       P.S Mbule, T.-H. Kim, B.-S. Kim, H.C. Swart and O.M. Ntwaeaborwa

- International Symposium on Luminescence (July 2012)

    6. Sensitizing effects of ZnO quantum dots on red-emitting Pr^{3+}-doped SiO_2 phosphor
       P.S. Mbule, G.H. Mhlongo, S.Pitale, H.C. Swart and O.M. Ntwaeaborwa

- 16thInternational workshop on inorganic and organic electroluminescence and 2012 International conference on the science and technology of emissive displays and lighting, held in Hong Kong, China from the 10th to 14th December 2012

    7. Effects of particle morphology of ZnO buffer layer on the performance of organic solar cells
       P.S Mbule, T.-H. Kim, B.-S. Kim, H.C. Swart and O.M. Ntwaeaborwa

Biography

Mbule Pontsho Sylvia was born in the eastern Free State, in the town called Fouriesburg, on the 24th March. She obtained her elementary and higher education in Fouriesburg and matriculated in 2002. She then went to the University of the Free State (Qwaqwa campus) to further her studies. She obtained her bachelor degree in chemistry in 2006. She obtained her B.Sc Hons (in Physics) in 2008. In 2008 she joined the department of physics at the main campus (Bloemfontein) to do her M.Sc. She conducted research in semiconductor physics, synthesizing and characterizing nanophosphors (Luminescent materials) and her M.Sc project title was sol-gel synthesis and luminescence properties of praseodymium (Pr^{3+}) doped different host matrices. In 2010 she started her Ph.D degree, adventuring in the renewable energy field. Her Ph.D project was on the synthesis of ZnO nanostructures via wet chemistry route for applications in organic solar cells as electron extraction layers. Firstly, the aim of the project was the importance of using ZnO buffer layer as electron extraction layer to improve the performance of organic solar cell devices. Secondly, the effects of ZnO particle morphology (spherical nanoparticles, nanoflakes and nanoflowers) on the general performance of organic solar cell devices. During the period of her research she was afforded the opportunity to visit national and international research laboratories to explore research in much greater heights. Her first international travel was when she went to Dubna, Russia in 2009, for participation in the "2009 practice for South African students at the joint institute for nuclear research (JINR) " and at the end of the workshop she presented the work on Time-of-flight (TOF) method in small angle neutron

scattering (SANS) experiment. She also went to the Korea institute of science and technology (KIST), South Korea in 2011/12, to learn how to fabricate and test organic solar cells as part of her Ph.D project. She attended national and international conferences like South African institute of physics (SAIP) conference, 4th South African Conference on Photonic Materials (May 2011), 4th International conference on Nanoscience and Nanotechnology (1-4 April 2012) to mention few, to present her research work. With the guidance and mentorship from her promoters she managed to publish her work in a prestigious journal with the impact factor of 4.5 and she also presented this work at the16thInternational workshop on inorganic and organic electroluminescence and 2012 International conference on the science and technology of emissive displays and lighting, held in Hong Kong, China, 10th to 14th December 2012.